

Rotational Core Losses in Hydro Generators

Jemimah C Akiror

A Thesis

In the Department

of

Electrical and Computer Engineering

Presented in Partial Fulfillment of the Requirements

For the Degree of

Doctor of Philosophy (Electrical and Computer Engineering) at

Concordia University

Montreal, Quebec, Canada

October 2016

© Jemimah Connie Akiror, 2016

Professor Nematollah Shiri, Committee Chair

Department of Computer Science and Software Engineering
Concordia University

Professor Abdelmounaïm Tounzi, External Examiner

Equipe 'Outils et Méthodes Numériques' du L2EP
Université de Lille - Sciences et Technologies

Professor Pragasen Pillay, Supervisor

Department of Electrical and Computer Engineering
Concordia University

Dr. Arezki Merkhoul, Co-supervisor

Unité Expertise Équipements électriques
Institut de recherche d'Hydro-Québec (IREQ)

Professor Luiz A. C. Lopes, Examiner

Department of Electrical and Computer Engineering
Concordia University

Professor Abdel R. Sebak, Examiner

Department of Electrical and Computer Engineering
Concordia University

Professor Radu G. Zmeureanu, Examiner

Department of Building, Civil and Environmental Engineering
Concordia University

ABSTRACT

Rotational Core Losses in Hydro Generators

Jemimah Connie Akiror, PhD
Concordia University, 2016

Accurate estimation of core losses in hydro generators is invaluable as it has implications of monetary value to both machine designers and utilities. For machine designers to meet the maximum acceptable total loss design targets, accurate loss estimation techniques are important to avoid the penalty of the extra losses generated. On the other hand, increase in the demand for electricity requires utilities to increase the output of their hydro generators as an alternative to building new stations, which is a more cost efficient option. Therefore, accurate prediction of core losses and their distribution, as part of the uprate studies, is key for any proposed uprate to determine the machine's hot spots and core capability. This will permit the increase in machine rating without compromising its life time.

This study is towards an accurate quantification of core losses and their distribution in hydro generators stators for uprate studies. The emphasis is on understanding the distribution of rotational flux in the generator stator core, rotational core loss measurements in lamination steel, and core loss estimation including both the rotational and non-sinusoidal flux density components. This entails 2D electromagnetic finite element modelling, validation and simulation of hydro generators, which are subsequently used for the analysis.

The distribution of rotational flux was found to be dependent on the stator dimensions and material BH curve operating point. Moreover, the associated rotational core losses resulted in a non-uniform distribution of losses in the stator, with higher localized losses at the back of the tooth. This new distribution of core losses is important in the thermal modelling to determine the distribution of hotspots in the machine.

In this work, the numerical analysis provides an understanding of what is happening in the machine beyond the current measurement capability in the real machine. The experimental measurements performed also support the numerical results in the loss estimation.

ACKNOWLEDGEMENT

First and foremost, I thank God without whom this wouldn't have been possible. For the gift of life, energy and zeal He provided from the beginning, through it all, till the end, and even the future to come.

Great gratitude goes to Prof. Pillay for the opportunity to pursue not only this degree but also my antecedent degree in an environment suited for growth, creativity and diligence. Thank you for ingraining in me that "just because it's hard doesn't mean it can't be done", a valuable lesson I will carry with me always.

Thanks also go to my supervisor at IREQ Dr. Merkhoul, for the opportunity to work in a top notch research center. The exposure and experience was invaluable, I have learnt a lot. Thanks also go to Dr. Julian Cave, also at IREQ for his guidance and the technical discussions.

Appreciation goes to my PEER group colleagues for the helpful discussions both technical and non- technical. Each of you from different parts of the world gave me a real taste of united nations.

Sincere thanks to Dr. John Wanjiku and Dr. Sudharshan Kaarthik for taking the time to proof read and critic this document. I am also grateful for your technical input in this work.

My life group "King's sons and daughters" members, thank you for being my family away from home, keeping me accountable and celebrating my small victories that culminated to this.

Thank you to my family back home; Mom, Dad, Charles, Bonny, Jane, Richard, Rachel, Arthur and Sue, Christine and Charles for the constant unconditional love and support.

Thanks to Afwoyo for being a great friend and my connection to the reality outside the lab.

Last but not least, special thanks to my fiancé David Okwii for your sacrifice, support, patience and understanding, which gave me a peace of mind to pursue this aspect of my career.

TABLE OF CONTENTS

List of Tables	ix
List of Figures	x
Chapter 1 : Introduction	1
1.1 Problem Statement	4
1.2 Objectives	5
1.3 Contributions	5
1.4 Limitations	7
1.5 Literature Review	7
1.5.1 Core loss measurement test benches	9
1.5.2 Models for pulsating and rotational core losses	12
1.5.3 Core faults	17
1.6 Thesis outline	21
1.7 Summary	22
Chapter 2 : Generator Modeling and Validation	23
2.1 Modeling	24
2.1.1 Geometry	25
2.1.2 External circuits	26
2.2 Simulation set-up	28
2.2.1 Time step and meshing	28
2.2.2 Simulation parameters	29
2.3 Model validation	30
2.3.1 Experimental results	30

2.3.2	Comparison of simulation and experimental results.....	34
2.3.3	Effect of parameter variation on performance	38
2.3.4	Final model parameters.....	43
2.4	Summary	44
Chapter 3	: Rotational flux Distribution.....	45
3.1	Definition of rotational flux	45
3.1.1	Aspect ratio	46
3.1.2	Percentage area calculation.....	48
3.2	Variation of the rotational flux with design and operating point.....	49
3.2.1	Yoke depth influence on rotational flux distribution.....	50
3.2.2	Air gap length influence on rotational flux distribution	51
3.2.3	Influence of the machine BH curve operating point on rotational flux distribution	52
3.3	Discussion of the results.....	56
3.4	Different machine designs	57
3.5	Summary	60
Chapter 4	: Magnetizer Design Core Loss Measurement	61
4.1	Design of the magnetizer	61
4.1.1	State of the art	62
4.1.2	Proposed magnetizer	64
4.1.3	Comparison of the testers	71
4.2	Core loss measurements.....	73
4.2.1	Pulsating core loss measurements.....	74

4.2.2	Rotational core loss measurements	76
4.3	Loss separation.....	78
4.4	Inter lamination faults.....	80
4.4.1	FEA model preparation.....	80
4.4.2	Simulation of the fault.....	83
4.4.3	Experimental measurement.....	87
4.4.4	Conclusion.....	93
4.5	Summary	93
Chapter 5	: Core Loss Estimation and Flux density Control.....	95
5.1	Core loss estimation.....	95
5.1.1	Sinusoidal flux density core loss estimation	95
5.1.2	Non-sinusoidal flux density core loss estimation.....	102
5.2	Flux density waveform control	106
5.2.1	DQ equivalent for the measurement set up	108
5.2.2	Feedback loop.....	110
5.3	Summary	113
Chapter 6	: Generator Winding Pattern Design.....	115
6.1	Generator winding refurbishment.....	115
6.2	Generator modelling and validation.....	116
6.3	Change in pattern winding.....	118
6.3.1	Natural frequency of the core.....	119
6.3.2	Armature MMF	120
6.3.3	Air gap flux density	122

6.3.4	Electromagnetic forces.....	123
6.3.5	Losses.....	125
6.3.6	Conclusion.....	126
6.4	Summary	127
Chapter 7	: Conclusions and Future work.....	128
7.1	Conclusions.....	128
7.2	Future work	130
Appendix A:	Coil Sizing	145
Appendix B:	Magnetizer Set-up at IREQ.....	147
Appendix C:	Safe Operating Procedures for the Rotational Core Loss Test Bench at Concordia University Power Lab.....	152
Appendix D:	Z-component field intensity distribution 1 mm above the sample for the proposed magnetizer.....	153

List of Tables

Table 1-1 : Summary of core loss models.....	16
Table 2-1 Machine nameplate data	24
Table 2-2 Performance tests on the units	34
Table 2-3 Synchronous reactance of the units	36
Table 2-4 Effect of parameter variation on open circuit voltage	40
Table 3-1 Aspect ratio percentage distribution in the stator	49
Table 3-2 Machine parameters	58
Table 4-1 Measurement area on the sample	69
Table 4-2 Comparison of the testers	72
Table 4-3 Angles for different aspect ratios.....	76
Table 4-4 Coefficients for hysteresis loss calculation	80
Table 5-1 No load and full load flux density and core loss.....	98
Table 5-2 Stator core loss calculation in different machine designs.....	101
Table 5-3 Core loss estimation considering the non-sinusoidal component	106
Table 6-1 Machine specifications	117
Table 6-2 Loss comparison.....	126

List of Figures

Figure 1-1: Loss distribution in 19 MVA hydro generator.....	2
Figure 1-2: B vector for one magnetizing cycle; (a) Pulsating flux, (b) Rotating flux.....	3
Figure 1-3: Non-sinusoidal excitation core loss measurement schematic.....	10
Figure 1-4: Core faults in turbo generators; (a) Effects of core loosening on a 493 MVA, 3600 rpm hydrogen cooled double-tube stack winding designed by Westinghouse [55] , (b) Melting of the 460 MVA, 24 kV hydrogen-cooled generator core due to inter-lamination core fault [56].	17
Figure 1-5: Set up of the flux test [60].....	19
Figure 1-6: Chattock coil placement to measure fault current induced fields [60].	20
Figure 1-7: Iron core probe placement in the slot wedge [65].....	20
Figure 1-8: Configuration for inter lamination fault testing in the stator using a rotor like structure [67].....	21
Figure 2-1: FEA model of the 19 MVA, 13.8 kV hydro generator; (a) 2D model, (b) 3D model. ..	25
Figure 2-2: Phase winding external circuit.	26
Figure 2-3: Damper bar circuit.	27
Figure 2-4: Model of the generator showing the meshing	29
Figure 2-5: Air gap flux measurement; (a) Coil probe used to measure air gap flux, (b) Positioning of the probes in the stator bore, (c) Location of the flux probes on the machine.	33
Figure 2-6: Comparison of measured open circuit air gap flux densities	33
Figure 2-7: Comparison of measured and simulated characteristic curves; (a) open circuit curve, (b) short circuit curve	35
Figure 2-8: Comparison of measured and simulated heat run test data; (a) open circuit curve, (b) short circuit curve	37

Figure 2-9: Comparison of measured and simulated air gap flux data; (a) No load, (b) 77% of rated load.....	38
Figure 2-10: Effect of change in simulation parameters; (a) Effective length, (b) Air gap length, (c) BH curve permeability, (d) Combination of air gap length and material permeability	42
Figure 3-1: Simulation results of the machine model at $I_f = 1090$ A; (a) Flux density magnitude distribution (b) Flux lines (c) Flux density loci at different points in the stator.....	46
Figure 3-2: Flux density loci; (a) Pulsating flux locus (b) Rotating flux locus	47
Figure 3-3: Plot of aspect ratio across the stator	48
Figure 3-4: Aspect ratio, R for different yoke lengths; a) 20 % less than the design length; b) 10 % less than the design length; c) design length; d) 10 % more than the design length and e) 20 % more than the design length.....	51
Figure 3-5: Effect of increase in yoke depth on rotational flux distribution.	52
Figure 3-6: Effect of change in air gap length on rotational flux distribution.	52
Figure 3-7: Measured open circuit curve of the 19 MVA generator showing simulated points...	53
Figure 3-8: 2D FEA model showing points where field data is extracted.....	53
Figure 3-9: Flux density loci at; a) Point 1: middle of the tooth b) Point 2: Back of the tooth c) Point 3: Back of the slot d) Point 4: Back of the yoke	54
Figure 3-10: Effect of saturation on rotational flux density distribution; (a) $I_f = 401$ A, (b) $I_f = 1090$ A	55
Figure 3-11: Effect of saturation on rotational flux density distribution using stator area.....	55
Figure 3-12: Percentage of stator area verses aspect ratio at three machine loadings.....	56
Figure 3-13: Aspect ratio distribution in different machine designs; (a) Machine 1, (b) Machine 2, (c) Machine 3 and (d) Machine 4.....	59
Figure 3-14: Comparison of the aspect ratio - R variation in different machines under open circuit conditions.....	59

Figure 4-1: 8-pole magnetizer, (a) 3D model, (b) 2D view with the coil number distribution.....	62
Figure 4-2: Field distribution with current of 10 A for the flux vector at 45° from the x, (a) Flux density distribution, (b) Flux vector.....	64
Figure 4-3: Field distribution with current of 10 A for the flux vector in the x, (a) Flux density distribution, (b) Flux vector.....	64
Figure 4-4: .Winding pattern for the different number of slots designs.....	65
Figure 4-5: The different magnetizer slot number (a) 3D models, and (b) Flux density distribution in sample, for i) 24 slots, ii) 36 slots, iii) 48 slots	66
Figure 4-6: Winding patterns.....	67
Figure 4-7: (a) Flux density distribution in the sample x-axis with the flux vector in the positive X direction for different design modifications at 10 A	68
Figure 4-8: 3D model of the new magnetizer design.	70
Figure 4-9: Sinusoidal winding diagram showing the number of coils per turn in each slot.....	70
Figure 4-10: Field distribution at 10 A with the flux vector in the y, (a) Flux density distribution, (b) Flux vector in the sample.	71
Figure 4-11: Field distribution at 10 A with the flux vector at 45° from the y, (a) Flux density distribution, (b) Flux vector in the sample.	71
Figure 4-12: Flux density distribution in the sample; a) previous magnetizer, b) New magnetizer	72
Figure 4-13: Core loss measurement setup.....	73
Figure 4-14: Pulsating core loss measurements at 60 Hz, (a) Measured BH loops of the X and Y, (b) Measured losses when x and y are excited independently and their average is the total core loss, (c) Measured losses when x and y are excited simultaneously, and the result is compared to the average from (b).....	74
Figure 4-15: Measured BH loops at different flux density levels	75

Figure 4-16: (a) Measured BH loops at 1 T for different frequencies, (b) Measured core losses at different frequencies	76
Figure 4-17: Measured rotational core losses at 60 Hz for; (a) Aspect ratio $R = 1$ in the clockwise and counter clockwise direction, (b) Different aspect ratios.....	77
Figure 4-18: Measured core losses at different frequencies	77
Figure 4-19: Measured rotational core losses at 10 Hz and 60 Hz	78
Figure 4-20: (a) Measured and predicted losses at 10 Hz, (b) Loss separation at 60 Hz	79
Figure 4-21: 3D model of the test rig with two laminations, the red shows the y coils and the blue the x coils	81
Figure 4-22: Comparison of flux density distribution across the lower sample in the x and y directions when one or two samples are used in the setup	82
Figure 4-23: Comparison of the flux density distribution across the sample in the x and y direction on the lower and upper samples.....	83
Figure 4-24: Sample with location and size of different faults; Fault A is 20 mm in diameter; Fault B is 40 mm in diameter and Fault C is 140 mm in diameter	84
Figure 4-25: Flux density distribution in the sample with the flux vector i) aligned to the $-X$ axis and ii) aligned to the Y axis, for; a) No fault in the sample, b) With fault A on the X and Y axis 30 and 40mm from the center of the sample, c) With fault aligned to the X axis	85
Figure 4-26: Flux density magnitude in the middle of the lower sample with the flux vector in the $-X$ direction (a) In the X direction (b) In the Y direction.....	86
Figure 4-27: Comparison of field quantities across the sample diameter with the magnetization direction in the x axis; (a) Field intensity magnitude on the sample surface, (b) Current density magnitude in the middle of the lower sample.....	87
Figure 4-28: Samples before and after the fault is imposed	88
Figure 4-29: Rotational core loss measurement setup.....	88

Figure 4-30: Core losses for M15G29 measured with one sample and with two samples	89
Figure 4-31: Flux density waveforms from the $\mathbf{B}_{x,y}$ sensors for the fault and no fault condition in the (a) clockwise and (b) counterclockwise direction	90
Figure 4-32: Field intensity from the $\mathbf{H}_{x,y}$ sensors for the fault and no fault condition in the (a) clockwise and (b) counterclockwise directions.....	91
Figure 4-33: Rotational core losses (a) at 60 Hz (b) at 400 Hz and 1 kHz for both faulted and non-faulted laminations.	93
Figure 5-1: Measured rotational core loss; (a) surface of the rotational core loss data, (b) goodness of the fitted surface	96
Figure 5-2: Flux density plot at no load and full load for (a) Point 1: Tooth; (b) Point 2: Back of the tooth; (c) Point 3: Back of the slot	97
Figure 5-3: Measured stator material properties at 60 Hz; (a) \mathbf{BH} curve, (b) Core losses.....	99
Figure 5-4: Measured rotor material properties at 60 Hz; (a) \mathbf{BH} curve, (b) Core losses.....	99
Figure 5-5: Comparison of machines with data from the stator radial line through the tooth to the yoke, for (i) Machine 1, (ii) Machine 2, (iii) Machine 3, (iv) Machine 4 where (a) Flux density and Aspect ratio distribution, (b) Core losses, pulsating and rotational core losses distribution	100
Figure 5-6: Non-sinusoidal waveforms; (a) Flux density waveforms from FEA, (b) Measured \mathbf{B}_x waveform, (c) Measured \mathbf{B}_y waveform.....	103
Figure 5-7: Estimation of the non-sinusoidal core loss components at (a) point 1: middle of the tooth \mathbf{B}_x , (b) point 2: back of the tooth \mathbf{B}_x , and (c) point 2: back of the tooth \mathbf{B}_y	104
Figure 5-8: DQ transformation stages (a) 3 phase symmetrical system (ABC), (b) Clarke transform from ABC to $\alpha\beta$, (c) Park transform from $\alpha\beta$ to dq	108
Figure 5-9: DQ transformation for the rotational test setup (a) 2 phase rotational flux system, (b) DQ transformation of the 2 phase system.	109
Figure 5-10: Block diagram of the feedback loop for waveform control.....	110

Figure 5-11: Simulation diagram of the feedback loop for waveform control	111
Figure 5-12: Feedback loop simulation results; (a) B_x waveforms and error, (b) B_y waveforms and error.....	112
Figure 5-13: Comparison of the sinusoidal reference and measured B-coil voltages for different flux densities ; (a) at 1.7 T, (b) at 1.9 T	113
Figure 5-14: Comparison of the non-sinusoidal reference and measured B-coil voltages for different flux densities ; (a) at 1.2 T, (b) at 1 T.....	113
Figure 6-1: Simulated machine at 86% rated load; (a) 2D FEA model, (b) Flux density distribution and flux lines.....	118
Figure 6-2: Comparison of the measured and simulated air gap flux density at (a) no load and (b) 86% of rated load.....	118
Figure 6-3: Machine stator winding patterns; (a) Old winding pattern (b) New winding pattern	119
Figure 6-4: Natural frequency of the machine core.....	120
Figure 6-5: Comparison of the analytically calculated stator winding MMFs of the old and new pattern winding.....	121
Figure 6-6: Comparison of the air gap flux density in both pattern windings; (a) At a point, (b) FFT of the air gap flux density at a point, (c) Radial air gap flux density.....	123
Figure 6-7: Comparison of the air gap electromagnetic force densities in new and old pattern winding; (a) Force densities along an air gap arc, (b) Force density FFT in pu	124

Chapter 1 : Introduction

Statistics from the Canadian Electricity Association show that hydro contributes about 63.3% of the total electricity generated in Canada [1]. In Quebec, 99% of the electricity is from 63 generating stations and 27 large reservoirs [2]. Most generators have been in operation for over 20 years, and were designed with large safety margins that can still be utilized to increase the nameplate rating without compromising the expected life time of the machine. As the demand for electricity increases, increasing existing generator output provides a cost effective viable alternative to building new power stations. This is because the cost and time involved in building new power stations requires large investments that may not be available especially in relation to the available demand.

Generator uprate is the increase of the generator output from its nameplate rating. Machine uprates can be achieved with minimal operational or structural changes on the generator and/or the turbine without replacing the entire unit [3], [4]. These include; increasing the power factor, increasing the operating temperature, refurbishment of the windings and the iron core, change or increase of the turbine output, installation of a new excitation system, and mechanical reinforcement among others. Extensive multi-disciplinary studies are therefore, a pre-requisite to any machine uprate to determine a precise distribution of all the losses, the potential areas of weakness in the system and suggest the limits within which the output can be increased, for the proposed changes. From an electrical point of view, one important aspect is determining the hotspots in the machine to ensure the machine operation does not go beyond the rated insulation class. This necessitates an accurate calculation and distribution of losses in the different parts of the machine.

Another application of the accurate loss calculation in large hydro generators is in the machine design. In the industry, hydro generator designers are tasked to guarantee certain total losses per machine rating. Failure to meet this specification results in penalties of over \$ 5000 per extra kW due to the client, lower losses result in the same monetary equivalent as a bonus to the designer. Therefore, accurate loss prediction techniques are imperative in the design process.

While the prediction of some losses in the machine such as the copper losses, friction and windage losses are straightforward and fully developed, other losses such as the core losses and stray losses still need more comprehension for better prediction techniques.

The segregated loss method is commonly used to determine the efficiency and the global loss distribution in synchronous machines. For large machines this is done using the calorimetric method [5]. Figure 1-1 shows the measured losses of a 19 MVA, 13.8 kV hydro generator using IEEE standard 115 [6]. For this machine core losses are 28% of the total machine losses. However the distribution of these losses in the core is unknown; hence the need for finite element analysis (FEA) modeling and simulation. FEA aids the visualization of losses, specifically copper and core losses, to identify hotspots in the machine. However, the results from FEA are contingent on the accuracy of the core loss formulae used. The aim of this work is to better understand and estimate core losses, and their distribution in large hydro generators for the purposes of machine design and uprating.

Core losses are the losses in ferromagnetic materials exposed to a changing magnetic field. The losses can be categorized into pulsating and rotational core losses. In pulsating core losses, the magnetic flux density (\mathbf{B}) only varies in magnitude akin to a sinusoid. The \mathbf{B} vector remains unidirectional, only changing direction in the positive or negative half cycle of the sinusoidal as shown in Figure 1-2 (a). At point 1 the \mathbf{B} vector magnitude is 0, as the field increases, the vector magnitude increases until the peak value at point 3 but maintains the same direction. After the peak, the \mathbf{B} vector magnitude begins to decrease until zero at point 4. In the negative half cycle of

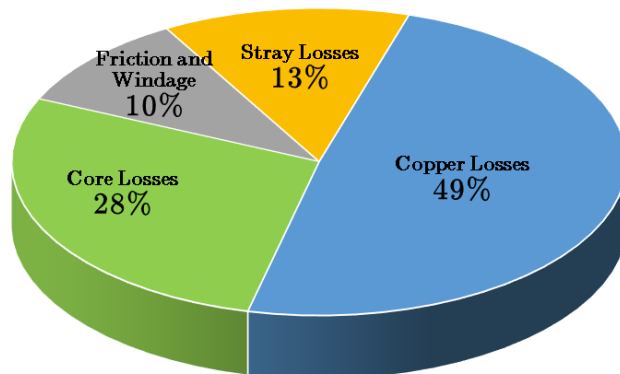


Figure 1-1: Loss distribution in 19 MVA hydro generator.

the magnetizing field, the **B** vector reverses in direction and begins to increase until the peak at point 5, after which it reduces in magnitude to point 6 and finally to zero at point 7.

Conversely, if the **B** magnitude remains the same and the **B** vector rotates with the field as shown in Figure 1-2 (b), this variation of the **B** vector causes rotational core losses. At point 1 when the magnetizing field A' is zero, field B' is at negative maximum, and the vector is aligned to the y axis. As both fields A' and B' increase until point 2 the **B** vector shifts by 45° . Further increase in the fields to point 3 where field B' becomes zero and field A' is maximum, the flux vector is aligned with the x axis. As field A' decreases and field B' continues to increase, the flux vector continues to rotate as shown at point 4. Point 5 is similar to point 1 with field B' at positive maximum hence point 1 and point 5 flux vectors are aligned in the opposite direction. As the fields increase and decrease, the flux vector rotates accordingly, while ideally maintain the **B** magnitude constant.

Rotational core losses are significantly higher than pulsating core losses (50% more in comparison between purely pulsating and purely rotating fields for the same flux density) at unsaturated flux densities levels in most machines. As a result, they need to be accounted for in machine core loss prediction methods.

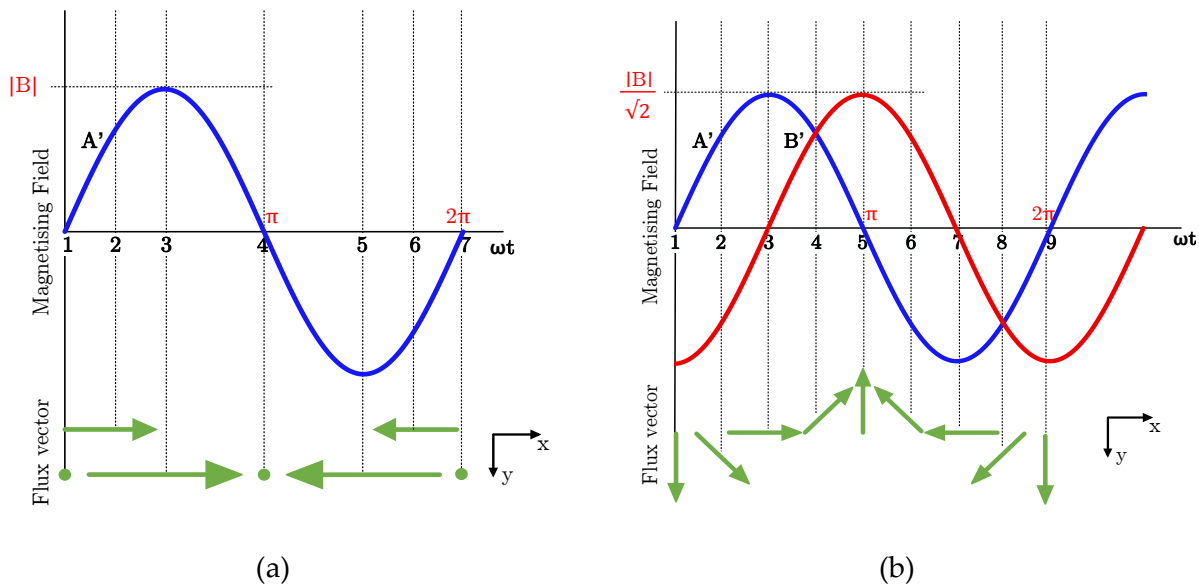


Figure 1-2: **B** vector for one magnetizing cycle; (a) Pulsating flux, (b) Rotating flux.

Methods used to estimate core losses in electric machines consider the flux to only be pulsating. However, this is not the case with electrical machine stators yokes [7] and transformer T-joints [8], where the rotating flux is localized. This localized rotating flux results into a localized heating of the core, which shifts the overall machine hotspot further into the stator yoke. Therefore, disregarding the rotating flux component not only underestimates the total core losses in the machine, but it also inaccurately defines the core loss distribution in the machine for determination of hotspots.

Core losses are fundamentally a function of frequency and flux density. In addition, they can significantly increase with material stress, high temperature operation, rotating magnetic fields and non-sinusoidal flux density among others. An ideal core loss model should include all the above effects. However, some of these properties are complex and difficult to model and quantify. Moreover techniques to measure them are still limited. This makes it challenging to match the predicted and measured core losses. For instance, the measured no load core losses also include eddy current losses in the stator windings due to slot leakage flux, rotor surface losses from eddy currents and slot passing harmonics, and damper bar conduction losses, which are usually not included in the numerical core loss prediction.

The scope of this work is to quantify and include the rotational core loss component into the predicted machine core losses for hydro generators. This involves investigation of the distribution of rotational flux in the machine, measurement of rotational core losses in the magnetic materials and estimation of the machine total core losses including the rotational component.

1.1 Problem Statement

Accurate prediction of core losses is important in machine loss estimation in machine design, efficiency estimation and uprate studies of hydro generators. Most available core loss prediction models are limited to pulsating flux, neglecting the rotational core loss component or they use pulsating data to approximate it.

This work proposes an engineering approach to compute the core losses in large hydro generators including the rotational core loss component. The method applies measured rotational

core loss data to each FEA mesh element flux density waveforms, to obtain the total core losses.

1.2 Objectives

The main objective of this work is to estimate core losses and determine their distribution in hydro generators. This is achieved by electromagnetic modeling and validation of the hydro generators, which are used in the analysis to determine the distribution of all the core loss components for accurate core loss computation.

Other objectives of this work include;

- To determine the influence of core faults on rotational core losses
- To design and prototype a rotational core loss test setup for core loss measurement of soft magnetic materials used in hydro generators. This includes both the sinusoidal and non-sinusoidal components of the pulsating and rotational core losses.

1.3 Contributions

The contributions of this work can be summarized as follows;

- The use of electromagnetic FEA analysis to explain the difference in performance of generator units with the same design drawings, using only their open circuit characteristic curve test data. This reduces the need for heavy instrumentation and tests on the unit, which is time consuming and expensive.
- Quantification of rotational flux in the machine using the stator area. This permitted the evaluation of the effect of change in stator dimensions and operating point on the distribution of rotational flux in the machine.
- Design of a 2D magnetizer with a wide measurement area of 65 by 65 mm. The test set-up is fully functional and adds to the material characterization capabilities of the laboratory.
- Implementation of feedback control on the flux density waveforms using proportional integral (PI) controllers in the DQ frame. This provides a faster and quicker way to control the flux density waveform, in addition to simulating an arbitrary waveform.
- Estimation of core losses in hydro generators including the rotational core losses, which will be used in determination of hotspots for generator uprate studies.

- Detection of lamination faults in rotating magnetic fields, a tool that can be developed for lamination fault detection in the stator core.
- Analysis of change in winding pattern for phase winding refurbishment of a 32.5 MVA hydro generator. This evaluated each winding pattern in terms of the air gap flux harmonics and electromagnetic forces to recommend the best winding pattern.

This study also resulted in the following technical publications:

Journals

1. J. C Akiror, A. Merkhof, C. Hudon and P. Pillay, "Consideration of design and operation on rotational flux density distributions in hydro generator stators," *IEEE Transactions on Energy Conversion*, vol. 30, no. 4, pp. 1585-1594, 2015.
2. J. C Akiror, P. Pillay and A. Merkhof, "Effect of saturation on rotational flux distribution in hydro generators", *IEEE Transactions on Energy Conversion* - Early Access

Conferences

1. J. C Akiror, A. Merkhof and P. Pillay "Parameter sensitivity of large electric machines," in *Energy Conversion and Congress Exposition (ECCE)*, Milwaukee, 2016.
2. J.C Akiror, A. Arezki, P. Pillay, C. Hudon and C. Millet, "Evaluation of the change in winding pattern of a large hydro generator" in *International Conference on Electric Machines (ICEM)*, Lausanne, 2016.
3. J.C Akiror, P. Pillay and A. Merkhof, "Rotational Core Loss Magnetizer: Design and Core Loss Measurement" in *International Conference on Power Electronics, Drives and Energy Systems (PEDES)*, Trivandrum, 2016 – Accepted.
4. J.C Akiror, A. Merkhof and P. Pillay, "Impact of rotational flux density distribution on the stator core losses in large hydro generators", *CIGRE meeting and colloquium on Rotating Electrical Machines: Requirements, Operation and Maintenance 2015*, Madrid, Spain.
5. J. C Akiror, P. Pillay and A. Merkhof, "Effect of saturation on rotational flux distribution in hydro generators", in *International Electric Machines and Drives Conference (IEMDC)*, Coeur d'alene, 2015.

6. J. C Akiror, P. Pillay and A. Merkhoul, "Detection of lamination faults from rotating magnetic fields," in *Energy Conversion and Congress Exposition (ECCE)*, Montreal, 2015.
7. J.C. Akiror, A. Merkhoul, C. Hudon and P. Pillay, "Consideration of design and operation on rotational flux density distributions in hydro generator stators", in *International Conference on Electric Machines (ICEM)*, Berlin, 2014.

1.4 Limitations

This work focusses on the prediction of core losses in hydro generators including the rotational core loss component. The approach used is based on applying the measured core loss data, including the rotational core loss component, to the numerical model of the generator, which provides a realistic core loss distribution in the machine.

The limitations in this work include:

1. Inability to account for material stress and operating temperature in the core loss measurements. The test bench is incapable of measuring this data, therefore these are not accounted for in the core loss prediction.
2. Exclusion of miscellaneous losses included in no load generator core loss measurement such as eddy currents in the phase windings from slot leakage flux, damper bar losses, rotor surface losses etc, which increase the total measured losses but are challenging to quantify numerically.
3. The curve fitting method used is dependent on measured core loss data, therefore the equations are material specific.

1.5 Literature Review

Core losses are one of the significant losses in electrical machines, mainly because a large portion of the machine volume consists of the core. The volume of the core required is a result of the power rating of the machine. Therefore the reduction of core losses is only possible by selecting soft magnetic materials of higher permeability and thinner gauge, which are characterized by lower losses. These materials are often more expensive than their alternatives,

thus the final choice of material is always a tradeoff between the machine performance and material cost.

The stator materials of large hydro generators require laminations of small thickness (≤ 0.5 mm), high permeability, low loss and mechanical stiffness, which enable it to transmit machine torques, provide mechanical strength against magnetic deformation forces and carry higher magnetic flux [9]. The rotor material on the other hand has a lamination thickness of 2 mm because of the lower core losses from the DC flux, and its requirement to withstand vibration from the rotation. Hence different materials are used in the stator and rotor of large machines. This implies both materials need to be characterized, and their core losses predicted.

Additionally, the process of generator core construction and operation involves material alloying, rolling and grain orientation, operation at high temperature, punching and mechanical clamping. All these factors affect the material permeability and hence the core losses [9]. Some of these effects can be quantified with measurements on material laminations but are difficult to verify in the entire generator both practically and numerically. Moreover calculation of losses from measurements on material laminations represent only a fraction of the losses in the real machine.

Another challenge to core loss estimation in large machines is the inability to include miscellaneous losses present during the machine core loss measurement. Core losses measured using IEEE standard 115 [6] include damper bar losses, eddy currents in the phase windings and space blockers from slot leakage flux, and rotor surface losses among others, which increase with the size of the machine. This explains the insufficiency of core loss models to predict losses especially if these factors are not accounted for.

The rest of this section presents work that has been done on core loss measurement techniques, core loss modeling in both soft magnetic material laminations and electric machines. Core faults specifically interlamination failure and their measurement techniques are also discussed.

1.5.1 Core loss measurement test benches

Magnetic steel materials are characterized by their maximum pulsating core losses at a specific frequency and flux density. Therefore, the accuracy of the core loss measurement method is important, since core loss quantification and modeling is dependent on the availability of core loss data at various frequencies and flux densities. Below are the core loss test benches used to measure core losses.

1.5.1.1 Pulsating core loss test bench

Magnetic steel manufacturers characterize their steel by providing the core loss at 1.5 T for a frequency of either 50 or 60 Hz, which is insufficient for core loss prediction in machines. The Epstein frame test is the standardized test used to measure core losses at various frequencies and flux densities [10]. This test frame has been commercialized due to its high consistency and ease of use. One of the setups available in the Concordia experimental laboratory is by Donart electronics that allows automatic core loss measurement over a wide flux density (**B**) range up to 1.9 T and frequency range of up to 4 kHz, depending the material properties [11].

This commercialized system provides the **B** and field intensity (**H**) curve of the material, and uses the wattmeter method to measure the core losses. Therefore the instantaneous **B**, **H** waveforms are not available and the system is further limited to measurements with sinusoidal excitation. However, in electrical machines the **B** waveforms at different points in the machine are non-sinusoidal. As a result an Epstein based test bench was designed in [12] to allow the measurement of core losses under arbitrary non-sinusoidal excitation. The schematic of this system is shown in Figure 1-3. This setup also allows the calculation of core losses using two methods; the wattmeter, and the area enclosed by the **BH** loop.

Despite its consistency, the Epstein frame test assumes a standard path length of 94 cm, which may not be the effective path length. In [13] the mean path length was found to be dependent on the peak flux density, frequency and permeability of the material under test. The Epstein test also assumes uniform flux density over the material area which is not always the case. These assumptions introduce a level of uncertainty in the measured core loss, which affect their accuracy. However, the Epstein test is consistent irrespective of the systematic errors.

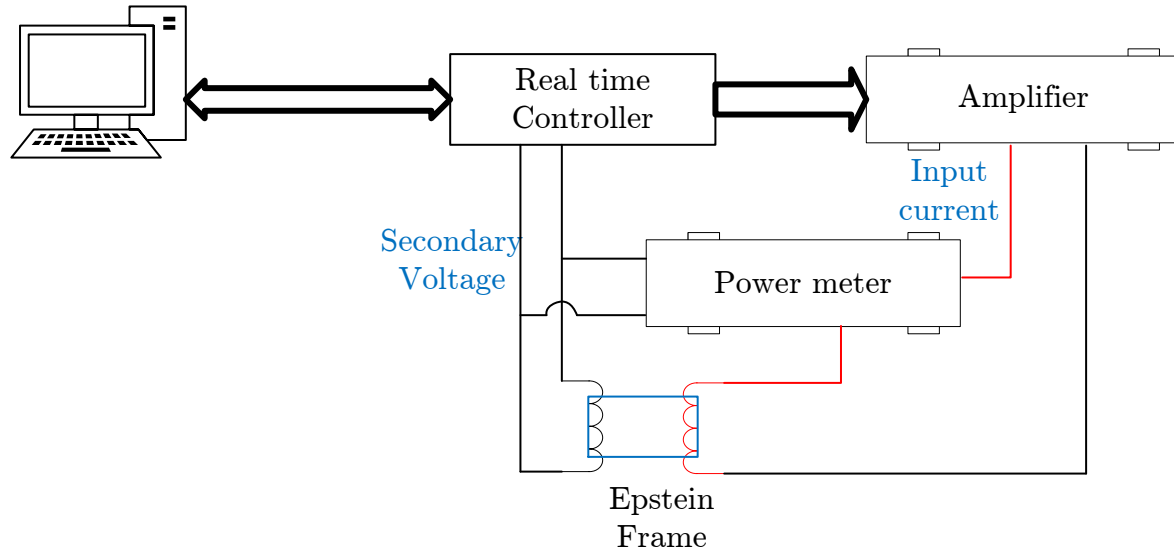


Figure 1-3: Non-sinusoidal excitation core loss measurement schematic.

A variation of the Epstein frame is the ring tester, which consists of a toroid of laminations wound with equal number of primary and secondary turns [14]. The flux path in this method is similar to that in a real machine. However, because the windings are directly wound on the toroid, the flexibility of varying the number of laminations and type of material is eliminated. Variation in the number of laminations allows measurement over a wider frequency and flux density range. The toroid method is rarely used because the winding process is time consuming.

Another commonly used core loss test frame is the single sheet tester, which derives its name from testing only one sheet at a time. Two variations of this tester were proposed in [15], it eliminates the effective path length problems and reduces the number of samples required by the Epstein frame test to one. Moreover, the sample preparation is also significantly lower than the ring tester. Hence the single sheet tester is commonly used by manufacturers for quality control. The main drawback of the single sheet tester is that one sample may not be an accurate representation of the material, for instance a sample cut in the rolling and transverse direction would give different properties. Therefore tests on many samples for the same material are required and the values averaged for a more accurate depiction of the material properties.

1.5.1.2 Rotational test bench

In a rotational core loss test bench, a rotating field is created by two orthogonal pulsating magnetic fields generated by the windings of the test yoke. When a sample is placed in the yoke, the area over which the flux in the sample is uniformly rotating is dependent on the yoke design, which has evolved over the years [16], [17] to include 3D yokes [18]. Consequently, sample shapes have also evolved from cross shaped, hexagonally shaped [19] and square shaped to circular shaped samples.

The method used to measure rotational core losses include the torque metric, thermometric and field metric methods. A torque magnetometer is used with the torque-metric method [20], while temperature sensors like thermocouples are used in the thermo-metric method [21], [22]. Although the torque-metric method allows the measurement of core losses at high flux densities, the required setup is complex hence it is rarely used. The thermo-metric method is an easier technique to use than the torque metric method since core losses are expended as heat. Thus the change in temperature of the steel is attributed to the core losses in the material, as a result of the applied field. Applications of the thermometric method include loss measurement in T-joints of transformers [8], induction motors [23] and determining the temperature distribution in stators [24], [25] of turbine generators. The disadvantages of the thermo-metric method are; placement of the sensors which can affect their functioning or alter the material properties, and slow response time and inability to measure losses at low flux densities when the temperature response is negligible [26].

The commonly used method is the field metric method, which relies on calculating the **BH** loop area using equation (1.1) from the Poynting theorem. This requires the simultaneous measurement of the instantaneous **B** and **H** fields in the sample. Techniques used to measure the **B** field include the needle tip method and the **B**-coils, while for **H** field Hall sensors, **H**-coils, Rogowski-Chattock coil and the magnetizing current method are used [16]. This method is easier to implement compared to the torque-metric method and provides measurements at lower flux densities better than the thermo-metric method. However, its accuracy depends on the proper alignment of the sensors, field uniformity in the sample measurement area, sensor accuracy and

sensitivity, and proper analysis of the measured fields. The main advantage of this method is the ability to measure core losses over a wide range of flux density (0.1 T – 2 T), and the visualization of the **B** and **H** loci, which provide more information on the material properties.

$$P_T = \frac{1}{T\rho} \int \left(H_x \frac{dB_x}{dt} + H_y \frac{dB_y}{dt} \right) dt \quad 1.1$$

where P_T , ρ , T , H_x , B_x , H_y , and B_y are the total core losses including the hysteresis and eddy current components, the density of the sample, the period of the waveforms, the measured fields in the x and y directions respectively. In [18], [21] and [27], a comparison of the thermo-metric and field-metric methods showed a good agreement in the results. Therefore, either method is sufficient for rotational core loss measurements.

In this work, a test bench is designed based on the test setup in [28] to allow a large measurement area of (65 by 65 mm). Moreover a controller is designed to control the flux density waveforms. In another section of this work, the test bench designed in [29] is used to study and measure the effect of interlaminations faults on rotational core losses. Both rotational core loss test setups use the field metric method to measure core losses.

1.5.2 Models for pulsating and rotational core losses

Core loss prediction models have improved over time as the need for accurate core loss prediction under real machine operating conditions became necessary. Steinmetz in [30] proposed the first analytical core loss model which was limited to calculating losses at flux densities less than 1 T. Bertotti in [31] proposed a three term model to include the eddy current and excess loss components. Core loss models have evolved since then to allow better fitting of the measured lamination data and thereafter prediction in a machine. Improvements in the models permitted inclusion of several aspects present in real machines such as non-sinusoidal flux density, minor loops and wide range of flux density operation, time domain calculation, machine drives among others. In [32] and [33], a model for core loss prediction at high frequency and non-sinusoidal flux densities was proposed. The authors in [34] and [35] proposed models for applications using a PWM supply, which is common in drive systems. For a wide frequency

and flux density range calculation, the model coefficients in [36] are considered variable with frequency and flux density, and in [37] and [38], the model allows core loss prediction with minor loops.

Most of the models were validated with core loss measurements in laminations but are seldom used in FEA core loss calculations for entire machines. The FEA core loss calculation models are required to be accurate, simple and less computationally intensive. Some models used in FEA software rely on curve fitting of the measured Epstein core loss data to predict core losses in the entire machine, using empirically based techniques with little physical connotation on core loss behavior. In the following subsections, simple models used to adequately predict core losses in electrical machines, under both pulsating and rotational fields are presented.

1.5.2.1 Pulsating core loss models

In this section some of the pulsating models that include some of the important factors for loss calculation in electrical machines are presented. A two term model in [39] takes into account a correction factor for skin depth and nonlinear material behavior using equation (1.2)

$$P_{IEM,A} = d_1 B^\alpha f + F_{skin} d_2 B^2 f^2 \left(1 + \frac{d_3 B^{d_4}}{F_{skin}} \right) \quad 1.2$$

where d_1 , d_2 , d_3 , d_4 , F_{skin} , B and f are the hysteresis coefficient, eddy current coefficient, coefficients determined from the error between the measured loss and the calculated loss, the correction factor for skin effect at high frequency, flux density and frequency respectively. This model uses constant coefficients; hysteresis coefficients from loss data with DC excitation, eddy current coefficients from the physical material properties, nonlinear component parameters d_3 and d_4 from the iron loss estimation error. Results showed a good correlation with measured data for some materials better than others. For example one of the tested materials had an error less than 15% for flux density higher than 1 T, and frequencies greater than 500 Hz. At lower flux densities however the error was about 50%.

The authors in [40] proposed a time domain function for the hysteresis component, which allows the calculation of losses with non-sinusoidal flux and also the losses in the presence of minor loops as shown in equation (1.3)

$$\begin{aligned}
 p_h(t) &= \left\{ \left| H_x \frac{dB_x}{dt} \right|^{\frac{2}{\beta}} + \left| H_y \frac{dB_y}{dt} \right|^{\frac{2}{\beta}} + \left| H_z \frac{dB_z}{dt} \right|^{\frac{2}{\beta}} \right\}^{\frac{\beta}{2}} \\
 p_c(t) &= \frac{1}{2\pi^2} kc \left\{ \left(\frac{dB_x}{dt} \right)^2 + \left(\frac{dB_y}{dt} \right)^2 + \left(\frac{dB_z}{dt} \right)^2 \right\} \\
 p_e(t) &= \frac{1}{C_e} ke \left\{ \left(\frac{dB_x}{dt} \right)^2 + \left(\frac{dB_y}{dt} \right)^2 + \left(\frac{dB_z}{dt} \right)^2 \right\}^{0.75}
 \end{aligned} \tag{1.3}$$

where p_h , p_c , p_e , kc , ke and β , is the hysteresis loss, eddy current loss, excess loss, eddy current coefficient, excess loss coefficient, the Steinmetz coefficient and $C_e = 8.763363$ respectively. This model was applied to a 2D, 165 W, 4 pole brushless DC motor, and a 3 phase 250 kVA power transformer. Comparison of the measured and calculated core losses returned an error of 4.6% for the motor and 5.5% for the transformer. Although the results from this method were accurate, the determination of some coefficients was not straight forward, while other coefficients were not based on real material data. This is a challenge for application to machine models whose materials are different from what was used.

1.5.2.2 Rotational core loss models

The rotational core loss component has generally been accounted for in two different ways; by adding a correction factor to the total pulsating losses [41] or by adding a correction factor for each individual loss component in the loss separation. In [42], the authors determine core losses in an induction machine using a third order polynomial in \mathbf{B} to describe the measured losses for each frequency obtained from a toroid tester. Discrete Fourier transform (DFT) analysis on the flux density waveforms is used to consider higher harmonic contributions. For rotational losses equation (1.4) was used

$$P_{rot} = [P_{alt}(B_{maj}) + P_{alt}(B_{min})]\gamma(\lambda, B_{maj}) \quad 1.4$$

where P_{alt} , B_{maj} , B_{min} , γ and λ are the pulsating core losses, the peak flux density on the major axis and minor axis, the correction factor and ratio of \mathbf{B} on minor to major axis respectively. In this method the rotational component is corrected for with a factor γ on the total pulsating loss. Up to 40 field harmonics were included in the calculation to obtain an error of 0.9%, when compared to measured results. However, as noted by the authors, the method was very time consuming. Moreover, the polynomial fitting of measured data to determine coefficients is dependent on the available material data, and the equation is unique to each material.

Other methods account for the rotational loss component by including a correction factor in loss separation on only the hysteresis loss component [43], or including the correction factor to both the hysteresis, eddy current and excess loss components individually. In [44] the correction factor was applied to the hysteresis and excess loss components as in (1.5)

$$\begin{aligned} P_{tot}^c = & ((1 - \Gamma) + \Gamma R_H(B_{max}))k_H B_{max}^2 f + \frac{k_c'}{T} \int_0^T \left| \frac{d\vec{B}}{dt} \right|^2 dt \\ & + ((1 - \Gamma) + \Gamma * R_E(B_{max})) \frac{k_e'}{T} \int_0^T \left| \frac{d\vec{B}}{dt} \right|^{1.5} dt \end{aligned} \quad 1.5$$

$$\Gamma = \frac{B_{min}}{B_{max}} \quad , \quad k_c' = \frac{k_c}{2\pi^2} \quad , \quad k_e' = \frac{k_e}{\sqrt{2\pi} \int_0^{2\pi} |\cos x|^{1.5} dx}$$

where R_H and R_E are the rotational loss correction factors corresponding to the ratio between the purely rotational and purely alternating hysteresis and excess loss components respectively. \vec{B} and T are the instantaneous flux density and the fundamental period of excitation respectively. The calculated losses predicted 65% of the measured core losses of 12 hydro generators, which was more accurate than a pulsating model that predicted 51% of the measured losses. However for lack of measured rotational core loss data, the coefficients used were from literature, which is a possible source of error as the coefficients are material specific.

A summary of the core loss model references is presented in Table 1-1, all models can predict core losses with sinusoidal flux density excitation. Model choice is often a tradeoff

between accuracy, available data, level of complexity, computation time and memory. Rotational core loss models can be used to predict pulsating losses, when only one axis flux density component is considered.

Table 1-1 : Summary of core loss models

Model features	Pulsating model	Rotational model
Non-sinusoidal flux density	[32], [33], [40]	[42], [43], [44], [49]
Skin effect	[39]	
Minor loops	[37], [38]	
Drive or inverter system	[34], [35]	
Analytical models applied to machines	[45], [46], [47], [48]	[41]

1.5.2.3 Calculation of core losses in large hydro generators

The models used to calculate core losses in laminations, and applied to smaller electric machines and transformers were presented in the previous sub-section. In this subsection, techniques currently used for core loss prediction in hydro generators with or without the rotational core loss component are presented. Most of the results from these models were compared with experimentally measured core losses in the generator or are from industrial practice.

Based on results from 70 units, rotational core losses in hydro generators were accounted for by multiplying the ring flux test core losses by a factor of 1.55 [50]. In [51], a comparison between the measured and calculated core losses of 46 synchronous generators with different core lengths and three different frame sizes, determined an average design factor of 1.71. These factors account for the differences between the calculated and measured core losses, which may not specifically be associated to the rotational core loss component. For instance in [44] the influence of rotational fields in core loss calculation of 12 hydro generators was studied. The authors determined that with the rotational component, the loss prediction improved by 14%.

However it still did not explain the 35% unpredicted core losses in the machines. Furthermore, core loss correction factors were found to be machine dimension dependent.

More recently in [52] and [53], the authors applied a multi-variable polynomial response surface function method to compute core losses in salient pole synchronous generators in the range 1-10 MW. This approach calculated core losses in each FEA mesh element using a surface fitted on measured pulsating core losses over a wide frequency and flux density range. In addition miscellaneous losses, eddy current losses elsewhere in the machine, were added to the calculated core losses, which predicted the core losses within an error of 10% without a correction factor. For the five machines used, the miscellaneous losses were in the range 7-50% of the measured losses, moreover the methods for calculating them were not referenced.

1.5.3 Core faults

A core fault in hydro generators is the failure of the laminated core, which can be a result of core loosening or inter-lamination failure. Core loosening occurs when the lamination stack is not well tightened, operation of the machine cause the laminations to vibrate and rub against each other deteriorating the core insulation as shown in Figure 1-4 (a). This core fault once detected can be corrected by either tightening the clamping nuts and bolts or by adding shims depending on the location of the fault [54].

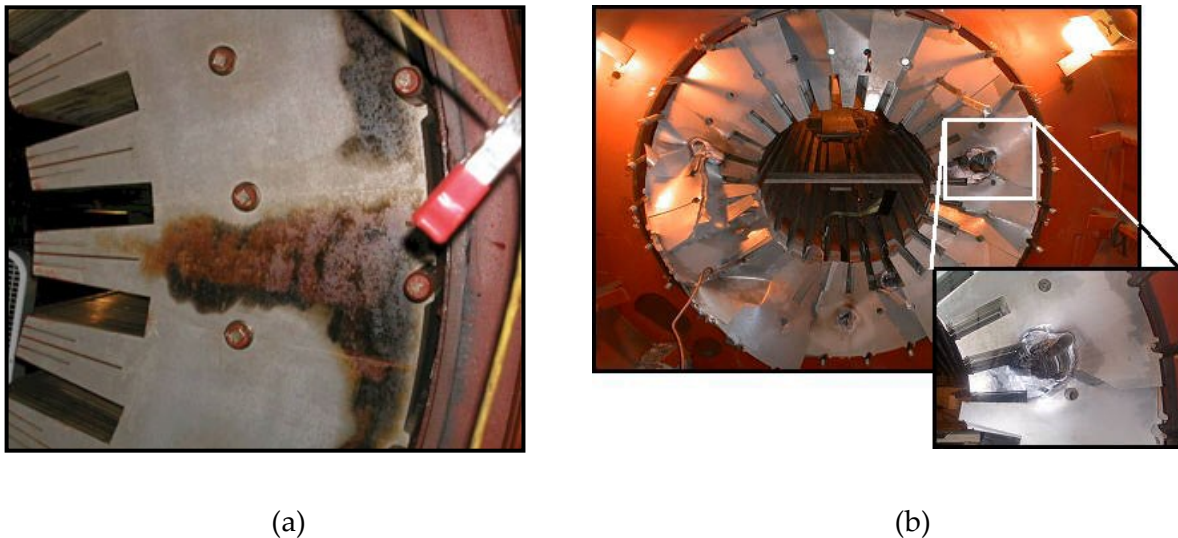


Figure 1-4: Core faults in turbo generators; (a) Effects of core loosening on a 493 MVA, 3600 rpm hydrogen cooled double-tube stack winding designed by Westinghouse [55] , (b) Melting of the 460 MVA, 24 kV hydrogen-cooled generator core due to inter-lamination core fault [56].

Inter-lamination failure occurs when the inter-laminar insulation loses its insulation properties therefore creating a short circuit in the laminations. Failure of lamination insulation in hydro generators leads to localized heating in the stator of the machine. The severity of this can lead to the melting of the core as shown in Figure 1-4 (b), winding insulation failure and eventual failure of the machine. Depending on the location or severity of this fault the entire stator core or a section needs to be replaced.

In [57] and [58], the authors discuss how these faults are initiated, their growth mechanisms and other factors that affect them from mechanical, thermal and electrical action. Keybars welded to the stator frame are used to align lamination segments in the core stack [9], in addition to providing a means of grounding for the core. This however also provides a path for fault currents, any other failure of the lamination insulation forms a closed path for the eddy currents to flow between the connected laminations. Shorting between laminations in hydro generators commonly occurs at the back of the slots [59], and occasionally at the tooth tips.

1.5.3.1 Core fault detection techniques on machines

Different methods have been used to detect faults. Many involve exciting the core and measuring the induced fault current or using thermal imaging to view the hot spots caused by the fault [60]. This is done by placing a magnetizing winding around the stator core to create flux in the stator toroid. The reference turn is then used to measure the induced voltage in the stator core as shown in Figure 1-5. As the flux circulates in the stator, it excites the faults causing fault currents to flow and localized heating.

The original ring flux test requires the stator to be excited to 85% of the rated flux at rated frequency [61]. This is to reproduce machine operating flux levels. The presence of a fault causes localized heating of the machine which can be detected using infrared cameras. The main drawback of this method is its high input current requirement which necessitates high safety measures, a power source and cabling capable of supplying the required current. In addition, a high flux level causes the machine to heat up, and the localized over heating in the fault areas can cause further damage of the core especially because the cooling system is off.

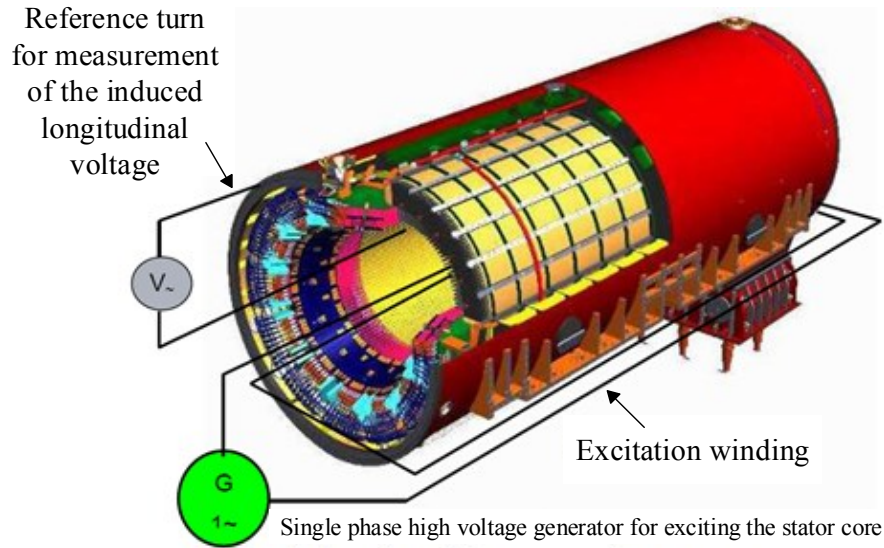


Figure 1-5: Set up of the flux test [60]

A variation of the ring flux test is the high frequency ring flux test [62]. A magnetizing current with a frequency of 500 Hz is used to induce a voltage of the same magnitude as in the original ring flux test, which reduces the current requirement. To detect the faults, both methods rely on an increase in the temperature (or hotspots) in the core and the ability of the thermographic cameras to capture the temperature variation. If the imaging is not sensitive enough, lower temperature faults may not be captured and therefore can easily be overlooked.

Another low excitation method is the Electromagnetic Core Imperfection Detection method (ELCID) [63]. This method uses a lower energy level, 4% of the rated flux at rated frequency, and detects the fault currents by measuring the magnetic fields they induce using a Chattock coil as shown in Figure 1-6. This is a preferred method of test for turbo-generators as it does not require the stator to heat up and the power requirement is low. The main drawback of this method is that its accuracy is dependent on the proper interpretation of the small signals acquired by the Chattock coil. Moreover, determining and categorizing faulty signals from different parts of the stator is not straightforward [64], therefore a lot of experience is required.

In [65] the authors improve the loss detection by using an iron core probe placed in the slot wedge area as shown in Figure 1-7. Using an iron core increases the sensitivity of the measurement hence a better signal to noise ratio, which reduces the commonly observed false

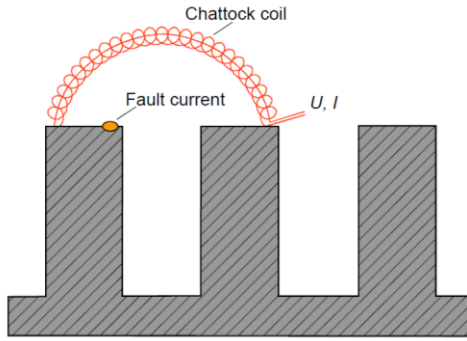


Figure 1-6: Chattock coil placement to measure fault current induced fields [60].

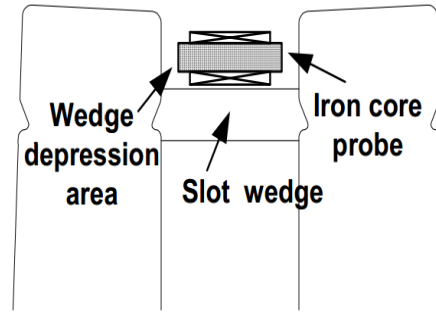


Figure 1-7: Iron core probe placement in the slot wedge [65].

positives in the ELCID method. This method was presented to be more reliable and easier to use, although it requires post processing.

1.5.3.2 Core fault measurement techniques on laminations

In [66] a rig design that measures the effect of lamination faults on a 150 stack of generator laminations is presented. A piece of shifted metal is used to provide a closed path for the flux, and a Hall sensor placed on the lamination surface to measure the field resulting from the fault current. Results showed a variation in the measured flux density of almost 10% in the presence of a fault.

A rotor like structure with pick up coils was used in [67] to measure losses over a stack of laminations. The rotor like structure shown in Figure 1-8 also contained the magnetizing coils and provided a return path for the stator flux. The losses were obtained by using the ampere turns method. One drawback of this method is that the accuracy of the method is dependent on the precise determination of the sensor losses (the rotor like structure). In this application the losses of the sensor are estimated using FEA analysis which may not be a real representation of the losses in the sensor.

Fault detection techniques generally rely on the sensitivity of the measurement method. For instance, in [68] twenty faulted laminations resulted into a 1.6% increase in core losses while in [69], the effect of the number of shorted laminations on the resulting fault current lead to a 50% increase in fault current for forty faulted laminations and 10% increase in the fault current for five

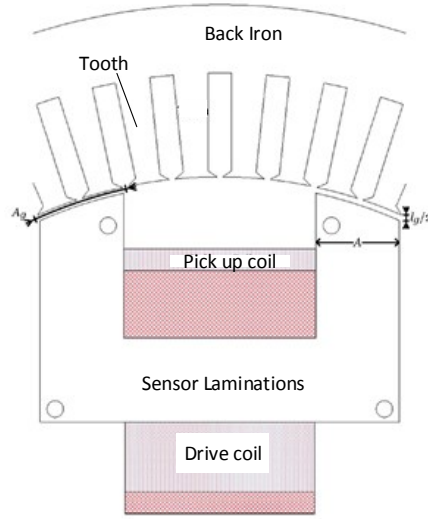


Figure 1-8: Configuration for inter lamination fault testing in the stator using a rotor like structure [67].

faulted laminations. This indicates the importance of using a sensitive measurement technique, which is independent of biasing external fields.

All the above methods are used to detect faults in the generator stator as a whole only considering sinusoidal pulsating flux in the stator yoke. However, the fault can occur in the stator yoke in the presence of rotating flux, which may increase the localized overheating. Part of this work will be to investigate the effect of core faults on rotational core losses.

1.6 Thesis outline

This thesis is organized as follows;

Chapter 1 provides the context for this research by stating the problem addressed, the objectives and importance of this work. A review of the current practices and techniques used core loss measurement and prediction is also presented as a building block to the specific contributions of this study.

Chapter 2 presents the FEA generator modeling and validation with emphasis on the challenges to modeling of large hydro machines. Consideration is given to how simulation and operation parameters affect the FEA model performance.

Chapter 3 defines how rotational flux is identified in the machine, and its distribution, which is used to evaluate the percentage of the machine with rotating flux. The influence of machine geometry and operating point on rotational flux distribution is also presented.

Chapter 4 describes the design of the rotational core loss tester, design of the flux density waveform controller and core loss measurement in soft magnetic materials.

Chapter 5 proposes a method to estimate core losses in the machine, including the rotational and non-sinusoidal components. A comparison of the stator losses with or without the rotational core loss component is also presented for four machine designs.

Chapter 6 applies FEA modelling to; generator phase winding refurbishment and core fault analysis in the presence of rotating flux. Numerical and analytical analysis of both application cases is shown, in addition to the experimental results.

Chapter 7 concludes the work done, provides recommendations and future work.

1.7 Summary

In this chapter, the importance of the accurate core loss prediction in generator design, efficiency estimation and uprate studies were emphasized. Literature relevant to this research was presented including core loss measurement techniques and test benches for both pulsating and rotational core losses.

Several models used to calculate core losses analytically or based on the curve fitting of measured losses were also presented, highlighting their unique features. For instance the ability to predict core losses with non-sinusoidal excitation, minor loops, and the presence of rotational flux.

The currently applied techniques for core loss prediction in hydro generators, and their limitations were also outlined. Finally, core faults in hydro generators are discussed with the aim of investigating the effect of lamination faults on rotating magnetic fields. The next chapter describes the generator FEA model used in this work.

Chapter 2 : Generator Modeling and Validation

Numerical design, modeling and simulation of electrical machines has greatly benefited from the increase in processing capabilities of computers. This has led to development of FEA software packages, which have enhanced rapid prototyping at a lower cost by permitting the prediction of machine performance before prototyping. In addition, FEA modeling enables the analysis of existing machines, as a way of explaining their performance.

In large synchronous machines, FEA modeling and simulation has facilitated the identification of synchronous machine parameters of existing machines [70] [71]; techniques envisaged to replace real-time offline tests. In other works, it has enhanced the study of the machine's response to different operating conditions [72] [73], and the comparison of different machine designs for the same application [74]. This information provides insight on the working and response of the generator to: various operating conditions, different kinds of faults [75], loss distribution and calculation of efficiency. FEA analysis is also invaluable in uprate studies of large hydro generators, as it generates the loss distribution maps and indicates the possible fault locations in the machine.

Other applications of numerical analysis on hydro generators include; the use of 2D FEA to optimize the no load voltage waveform by designing an asymmetrically shifted pole shoe and damper bars [76], implementation of static and dynamic eccentricity studies in 2D [77] and 3D [78], transient characteristics determination of a 199 MVA machine in [79], and generator hotspot determination by coupling the electromagnetic and thermal simulations in [80].

All the above applications require a well-defined FEA machine model, which was validated with experimental measurements prior to being used for the analysis. This section therefore describes the numerical model used in this work, whose validation is also presented. Moreover, the challenges encountered in numerical modeling of large machines are also highlighted. A final model is chosen to represent the generator unit based on its accurate prediction of the generator

performance, when compared to experimental results. The result of this chapter is the generator model used to study rotational flux distribution in chapter 3.

2.1 Modeling

The generator system consists of the turbine, shaft, rotor, stator, windings (both field and phase windings), stator frame, rotor spider, excitation system and other auxiliary systems such as the cooling system, governor system, gate opening system. This work focuses on the electromagnetic aspects of the machine, therefore only the electric and magnetic parts of the generator are considered in the FEA model. Geometrically this includes the excitation system, the soft magnetic core, rotor and stator, and the windings, damper bars, phase and field windings. The step by step creation of the generator FEA model is described in the following subsections.

A 6 m bore diameter, 19 MVA, 13.8 kV three phase hydro generator with 9.92 mm air gap, 780 mm rotor stack length, and 760 mm stator stack length is modeled from the machine drawings in commercial 2D and 3D FEA software [81]. A section of the machine model in 2D and 3D are shown in Figure 2-1. Typically for older machines without drawings, the industrial practice is to use imaging techniques to identify the pole shape. By virtue of the machine size, the required computation time and memory, only the 2D model was considered. The 2D model is an approximation of a 3D model slice assuming the same rotor and stator length. Therefore, the field distribution in the 2D model is similar to the 3D model. Moreover, for core loss estimation, a 2D simulation is sufficient hence it was considered for simulation of the machine in Table 2-1.

Table 2-1 Machine nameplate data

Power	19 MVA	Excitation voltage	117 V
Voltage	13.8 kV	Power factor	0.8
Stator current	795 A	Reference speed	120 rpm
Real Power	15.2 MW	Number of poles	60
Field current	1133 A	Number of slots	336

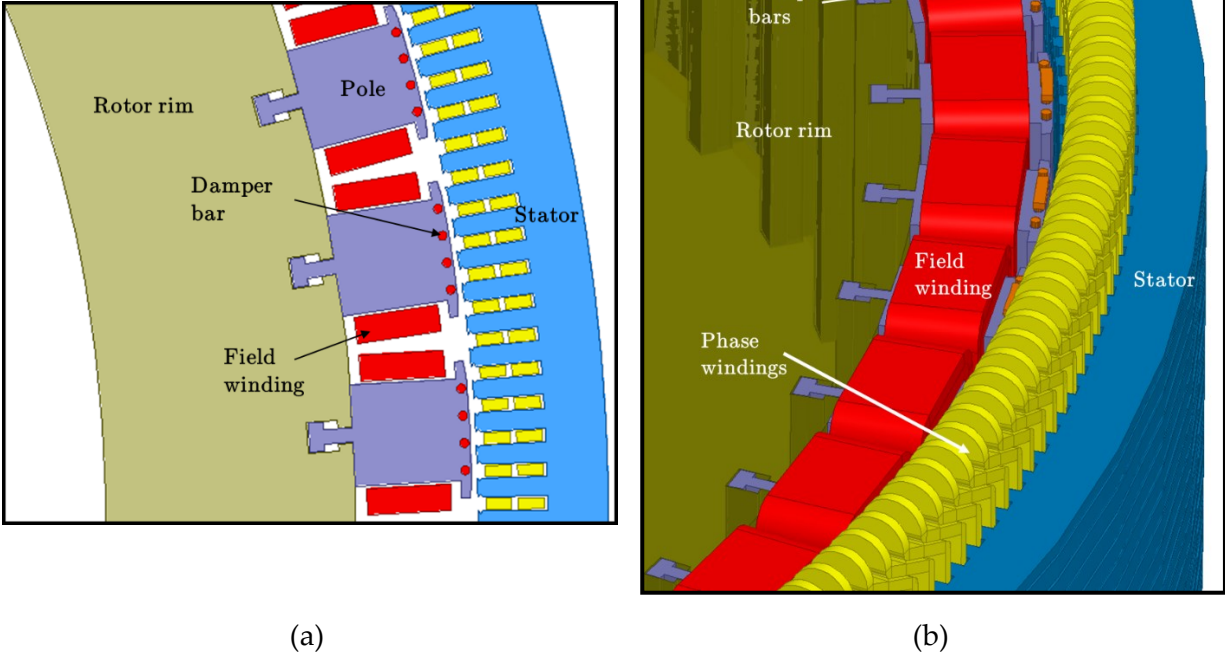


Figure 2-1: FEA model of the 19 MVA, 13.8 kV hydro generator; (a) 2D model, (b) 3D model.

2.1.1 Geometry

Large diameter machines require a lot of computation time and memory even for 2D simulations. For instance, using a quarter of the machine model requires 1.01 GB to mesh 559190 elements, which are less dense, and for one simulation time step 5.31 G memory is required. Therefore to reduce the simulation time and memory requirements, the machine symmetry is exploited with the appropriate boundary conditions to minimize the model size. The armature fractional winding has $1\frac{1}{15}$ slots per pole per phase which means the magnetic symmetry of the machine repeats every 15 poles. However for this machine, the winding sequence only repeats once, and therefore half of the machine (30 poles) is required for simulation.

Master and slave boundary conditions are applied on the edges of the machine, while a zero vector potential boundary is used at the stator yoke edge to limit the flux to the stator boundary. The stator and rotor are of different lengths, therefore an effective length for 2D simulation is calculated using (3.1)

$$L_m = \min(L_s, L_r) - \eta_v b_v k_{bv} \quad 3.1$$

where $\min(L_s, L_m)$ is the minimum of the two lengths, L_m is the effective length, L_s is the stator length, L_r the rotor length, η_v is the number of ducts, b_v is the duct width and K_{bv} is duct loss width coefficient based on air gap flux considering the position and presence of ducts in the rotor and/or the stator [82]. Epstein measured core loss and **BH** curve data for the rotor and stator materials are assigned to their respective parts.

2.1.2 External circuits

The effect of the end winding and damper bar impedances are included in the model using lumped parameters in an external circuit imported into the FEA model. External circuits are also used to impose a load on the machine using the equivalent phase resistances and inductances. Two types of circuits are defined; the phase circuit, which contains the equivalent load and phase end winding resistances and inductances, and the damper bar circuits which contain the equivalent damper bar end winding resistance and inductance.

2.1.2.1 Phase circuits

Figure 2-2 shows the circuit used to emulate the end winding impedences and load quantities, where R_{end} , L_{end} , R_{load} and L_{load} are the equivalent per phase end winding resistance and inductance, and equivalent per phase load resistance and inductance respectively. This is an approximation of the load which is the grid in this case, more detailed models can be used.

The per phase equivalent end leakage inductance and terminal resistance are analytically calculated from the machine geometry, while the equivalent loading per phase is computed based on the required output power, voltage and power factor using (3.2) and (3.3)

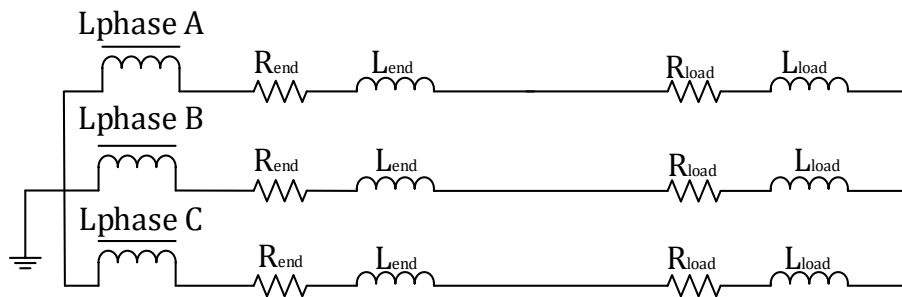


Figure 2-2: Phase winding external circuit.

$$P_{3\phi} = n S_{3\phi} pf$$

$$Q_{3\phi} = \sqrt{(n S_{3\phi})^2 - (P_{3\phi})^2}$$
3.2

$$R_{eq} = \frac{P_{\phi}}{I^2}$$

$$L_{eq} = \frac{Q_{\phi}}{2\pi f I^2}$$
3.3

where n , $P_{3\phi}$, $Q_{3\phi}$, $S_{3\phi}$, pf , f , R_{eq} , L_{eq} and I are the percentage of rated power, 3 phase real power, 3 phase reactive power, 3 phase apparent power, power factor, frequency, equivalent load resistance and inductance, and phase current respectively. For no load simulations, a large equivalent per phase resistance of 10 GΩ is used as the load to emulate an open circuit.

2.1.2.2 Damper bars

Each pole has four damper bars connected at the top and bottom of the pole, and each pole is isolated from another. This is modeled using the external circuit in Figure 2-3 for 30 poles, where R_{dend} , L_{dend} , and R_{pend} are the damper bar equivalent end winding resistances and inductances, and inter pole resistance respectively. A large value of 10 GΩ for R_{pend} is used to isolate the poles as in the real machine, mainly because the external circuit requires all circuit components to be connected.

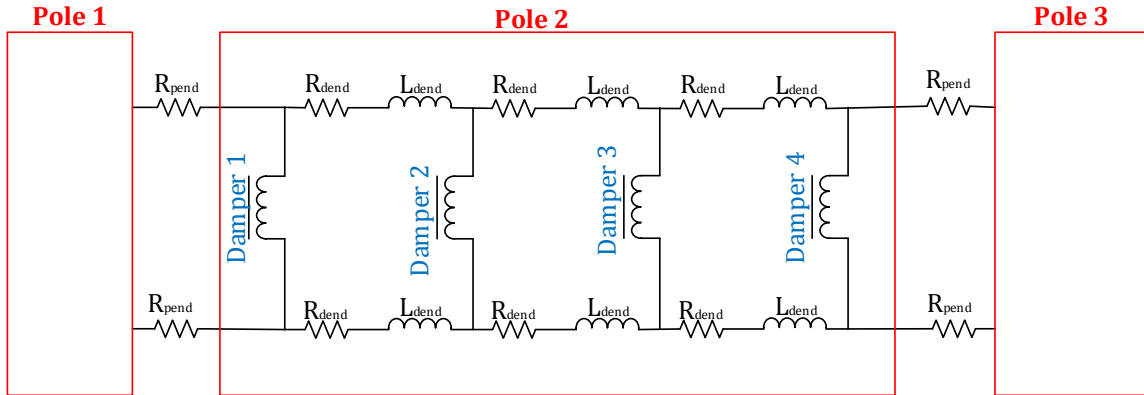


Figure 2-3: Damper bar circuit.

The excitation system is modeled using a constant DC current source. In reality, the excitation system is another machine coupled to the generator shaft. A constant DC current source is a simplification of the excitation system that neglects the transient behavior and interaction between the DC machine and generator. In the future, this DC machine model can be included in the co-simulation with the generator.

2.2 Simulation set-up

A transient non-linear magnetic solver, which computes time domain magnetic fields from winding conductors as functions of time, position and speed was chosen for simulation. This solver couples external circuits, includes rotational and translational motion, the calculation of eddy currents and includes the non-linear field behavior of the magnetic fields.

All coil conductors were assigned to the appropriate phase A, B and C windings as in the machine's winding diagram with two parallel paths in each winding. Stator and rotor core loss post processing, and eddy current solving in the winding are enabled.

2.2.1 Time step and meshing

The simulation time step Δt was calculated using equation (3.4) to sufficiently capture the slot passing harmonics

$$\Delta t = \frac{f}{N_s \omega N_{Spl}} \quad 3.4$$

where f is the frequency, N_s is the number of slots, ω is the speed in rpm and N_{Spl} is the number of samples. Total simulation time is chosen to be long enough to allow the machine to reach steady state. Since the transient time is longer for the loaded condition, simulation time for no load and loaded conditions are different; 0.3 s for no load and 0.5 s for loaded condition are used in this study to determine the rms value of the induced phase voltages and currents.

For preliminary results, length based - inside object meshing was selected based on the adaptive meshing in the software, where the mesh is refined until the field solutions do not

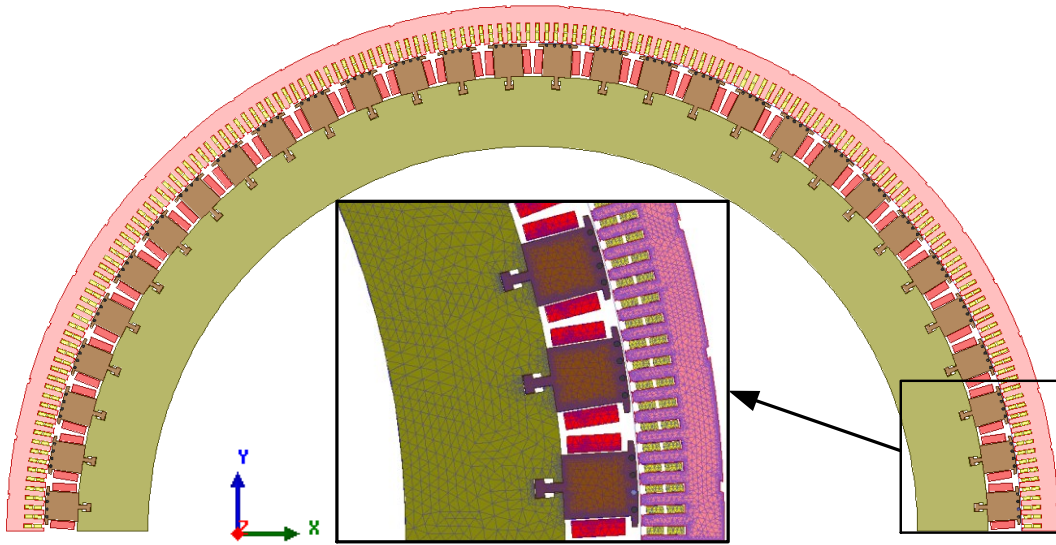


Figure 2-4: Model of the generator showing the meshing

change with mesh refinement. This mesh is later refined in the stator, where the rotational flux distribution and core loss is to be determined. Figure 2-4 shows the meshing details used in different parts of the machine.

2.2.2 Simulation parameters

The machine symmetry multiplier is set to 2 as half of the machine is modeled. This implies that the simulation results are applicably multiplied by 2. Two regions are set in the air gap, one region only encloses the rotor and the second region encloses the rotor and extends to the middle of the air gap. These regions permit motion setup in the rotor for a transient simulation without having the rotor re-meshing at every time step.

Positive rotational motion is setup in the second region with a moving vector of 120 rpm angular velocity in the global Z axis. This sections the meshing in the air gap into a static and sliding mesh, which limits the re-meshing at each time step to a section in the air gap while the rest of the model maintains a static mesh.

Field solutions of two electrical cycles are saved for each time step for post processing. Other solutions such as the induced voltages, winding currents, electromagnetic torque, flux linkage and damper bar currents are saved in the transient solution.

2.3 Model validation

The 2D FEA model of the generator requires validation before being used for any analysis. Model validation ensures that the model accurately represents the intended machine. This is done by comparing the model simulated results and experimentally measured results for each available test point. The model is then tuned to accurately predict the machine performance. However, the availability of experimental results especially for hydro generators is limited by the cost and time required for instrumentation and testing of the generators. This time also translates to the revenue lost during off time. Therefore testing is limited to scheduled maintenance down time or before/after machine refurbishment to verify machine performance.

This section presents the validation of the 2D FEA generator model with experimental results. Moreover, using different simulation and operational parameters as shown in this section, the model can be tuned to represent any machine of the same design.

2.3.1 Experimental results

The common performance tests used in hydro generators are measurement of characteristic curves and the heat run test, which include; the open circuit curve, short circuit curve, temperature rise tests. These tests are also used to determine the efficiency of the machine and are performed based on IEEE std 115 [6] and IEC 60064 [5]. For large machines the method of loss measurement is usually by temperature using the calorimetric method. The tests described in this section were performed by certified industrial personnel, who provided the data for post processing and model validation.

2.3.1.1 Open circuit characteristic curve

Open circuit (OC) test gives the machine saturation curve, and together with short circuit test can be used to determine the unsaturated synchronous reactance of the machine. In this test, the excitation current is varied, and the induced phase voltages at rated speed are obtained with the machine running at no load. Losses obtained in this test include; the rotor copper loss, core losses, friction and windage losses as shown in (3.5)

$$P_{NL_loss} = P_{Cu_rotor} + P_{core} + P_{FW} \quad 3.5$$

where P_{NL_loss} is the no load losses, P_{Cu_rotor} is the rotor copper loss, P_{core} is the core loss, P_{FW} is the friction and windage loss. The rotor copper loss can be obtained from the known rotor resistance and current, while the constant friction and windage losses can be obtained by running the machine at rated speed with no excitation. Core losses can also be obtained at each point on the open circuit curve if the friction and windage losses known [6].

2.3.1.2 Short circuit curve

This test is done with the armature short circuited at rated speed. The field and armature currents are recorded in intervals over a range of 125% to 25% of rated armature current [6]. Losses in this test consist of the friction and windage, core losses, stator and rotor copper losses and stray load losses. With all the other losses known from the open circuit test, the stray load losses which vary with the load can be obtained as

$$P_{Stray} = P_{SC_loss} - P_{NL_loss} - P_{Cu_stator} \quad 3.6$$

where P_{stray} is the stray load loss, P_{SC_loss} is the short circuit loss and P_{Cu_stator} is the stator copper loss.

The open circuit and short circuit tests facilitate the segregation of losses in the machine at any operating point with the assumption that the core losses, friction and windage losses are constant. Sometimes a correction for the friction and windage losses is applied especially if the loss is measured by the calorimetric method.

2.3.1.3 Heat run or temperature rise test

This test is done to determine the temperature rise of different parts in the machine. For different loads, temperature in various parts of the machine is measured and compared to the reference temperature, usually the coolant temperature [6]. Temperature measurement techniques used in different positions in the machine include; thermocouples, resistance temperature detectors (RTDs), and thermometers among others. Results from this test give an indication of the machine's ability to operate at different loading conditions without compromising its insulation class.

2.3.1.4 Calorimetric test

The generator efficiency can be obtained from the segregated losses using the calorimetric method. Losses in machines are expended as heat, therefore cooling circuits are designed to remove most of this heat. The calorimetric method determines losses in the generator by calculating the amount of heat the cooling circuits remove from the machine (evacuated losses) [5]. Given the water flow, inlet and outlet temperatures of the cooling circuits, the losses can be determined using (3.7)

$$P_L = C_p \rho Q \Delta T \quad 3.7$$

where P_L is loss in kW, C_p is the specific heat of water (kJ/kg°C), ρ is the water density (kg/m³), Q is the water flow rate (m³/s), $\Delta T = (T_o - T_i)$, T_o is the outlet temperature, T_i is the inlet temperature all in °C. For a different coolant the appropriate values should be used. Losses in the bearings, and losses due to convection and radiation transmitted by the bottom part of the generator are also added to the total losses using the measured temperatures from the different parts.

2.3.1.5 Air gap flux density measurement

The air gap flux is measured using calibrated circular coil probes placed at different points in the machine air gap. Figure 2-5(a) shows the 10 turn, 1 inch diameter coil probe and their location in the stator bore at C1, C2, C3, C4 as in shown in the schematic of Figure 2-5(b). To locate the sensors, a pole is sometimes removed and the sensor attached to the desired stator tooth packet as shown in Figure 2-5(c). Removing the pole allows proper location of the sensor on the desired stator packet, the pole is replaced for normal operation of the machine.

The flux density in the air gap is obtained by integrating the measured induced voltage across the coils terminals as

$$B = \frac{k}{NA} \int e(t) dt \quad 3.8$$

where B is the flux density, k is the coil calibration constant, N is the number of turns, A is the area enclosed by the coil and e is the induced voltage. A comparison of the results from three of

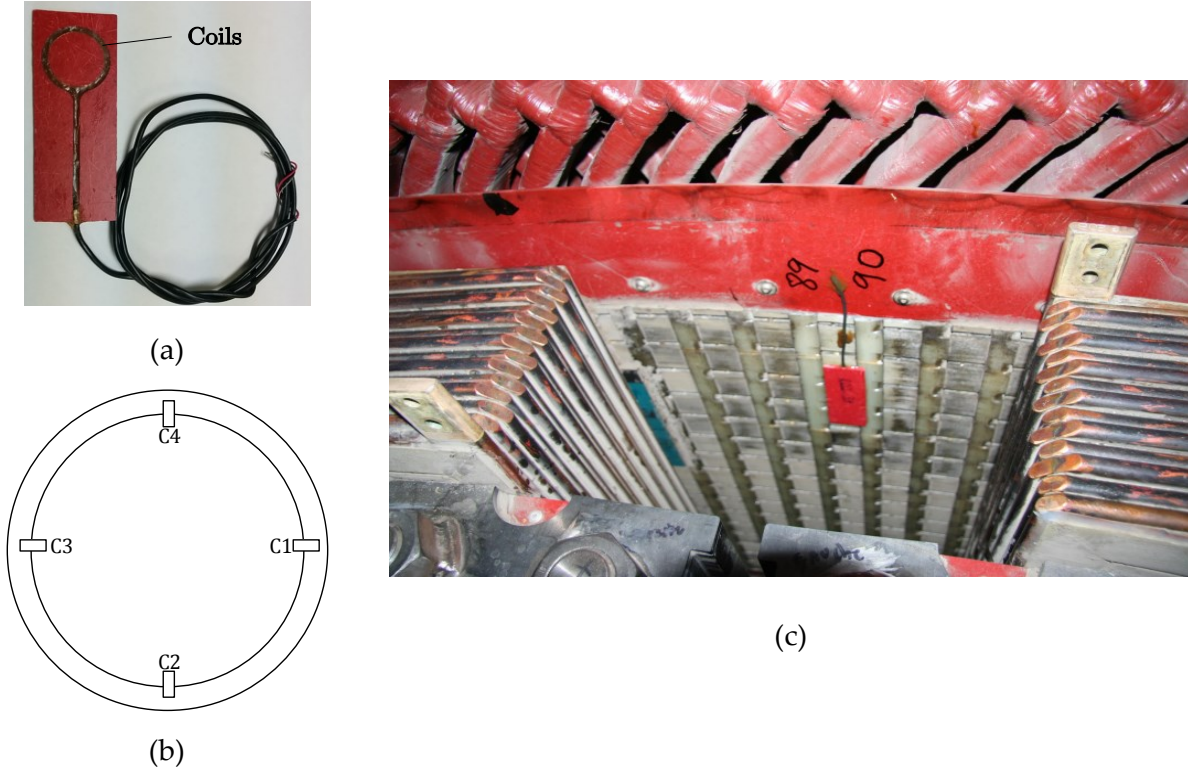


Figure 2-5: Air gap flux measurement; (a) Coil probe used to measure air gap flux, (b) Positioning of the probes in the stator bore, (c) Location of the flux probes on the machine.

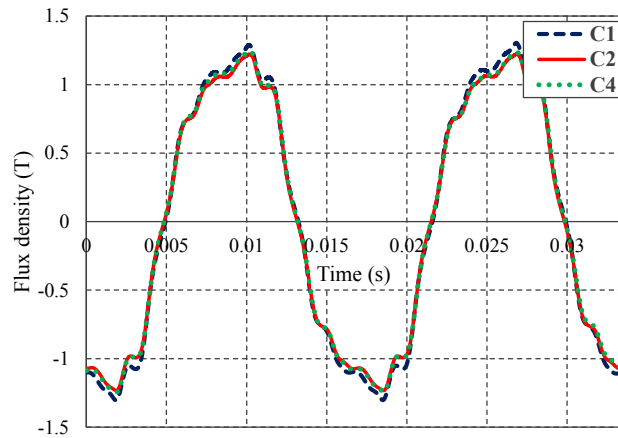


Figure 2-6: Comparison of measured open circuit air gap flux densities

the probes at 77% rated load, were in good agreement as shown in Figure 2-6. The difference in peak flux density values ($C1 = 1.312 \text{ T}$, $C2 = 1.242 \text{ T}$, $C4 = 1.243 \text{ T}$) can be attributed to the slight difference in positioning of the coils axially across the packet. In simulation the flux density in all the different points was the same. For comparison purposes results from C4 were used.

2.3.2 Comparison of simulation and experimental results

Results from four generator units A, B, C, and E of the same machine design are compared with the simulated machine. These machines were commissioned at different times, which implies they are made from different material batches. Therefore it is possible to investigate the differences in material performance. Unit D and B are exactly the same unit with tests performed before and after the collector overheating and high noise level problems were fixed respectively. Unit C results were obtained after the stator parallel paths were changed to increase the phase voltage from 6.9 kV to 13.8 kV. Select tests were performed on each of the machines as shown in Table 2-2.

In this section, the available experimental measurements are compared to the simulated results. Comparison of the results is presented in per unit (pu) with 560 A as the base excitation current, 795 A as the base phase current and rated phase voltage 7.967 kV as the base phase voltage. For each simulation, the induced rms phase voltages and currents are recorded when steady state is reached. The results are averaged over 6 cycles. For comparison with the measured values, the mean of the 3 phases is used.

Open and short circuit curve simulations were done using the parametric analysis setting. In the OC curve simulation, the excitation current was increased from 0 to 1200 A in steps of 50 A. This range is selected to cover both the linear and saturation portions of the open circuit characteristic curve. The simulation time for each step took an average of 32 hours for a single

Table 2-2 Performance tests on the units

Tests		Unit A	Unit B	Unit C	Unit D	Unit E
Open circuit		×	×		×	×
Short circuit		×			×	×
Heat run		×		×	×	
Calorimetric			×			
Air gap flux				×		
Material	BH	×	×	×	×	×
curve						

license processor. In the SC curve simulation, the excitation current is varied in the range 120 A to 680 A in steps of 112 A. This range choice was based on the available experimental data. A $10\text{ G}\Omega$ resistance is imposed on the phases for the OC simulations and the induced phase voltages recorded, while the phase circuits are short circuited in the SC simulations, and armature current recorded for each phase.

Heat run test simulations for the units are done based on the available experimental data. The equivalent impedance per phase for each loading is calculated and imposed on the phases. Excitation current used for each of the heat run points is the same as in the experiment. The induced phase voltages and currents were recorded for each phase.

2.3.2.1 Comparison of open circuit and short circuit data

A comparison of the measured open circuit curves from the different units and the simulated machine is shown in Figure 2-7 (a). Results show a large variation in the open circuit curves among the units, and the simulated results. Units A and E agree until saturation, as do the results of unit B and unit D. After 0.8 pu excitation current, the induced voltage begins to diverge as the machine saturates, implying that at saturation other factors influence the OC voltage output. However, the simulated result follows a different trend from the measured results. It starts off the same as units A and E, and toward saturation it exceeds unit D. Unit B and D which are the same machine also show a variation in their measured results at saturation.

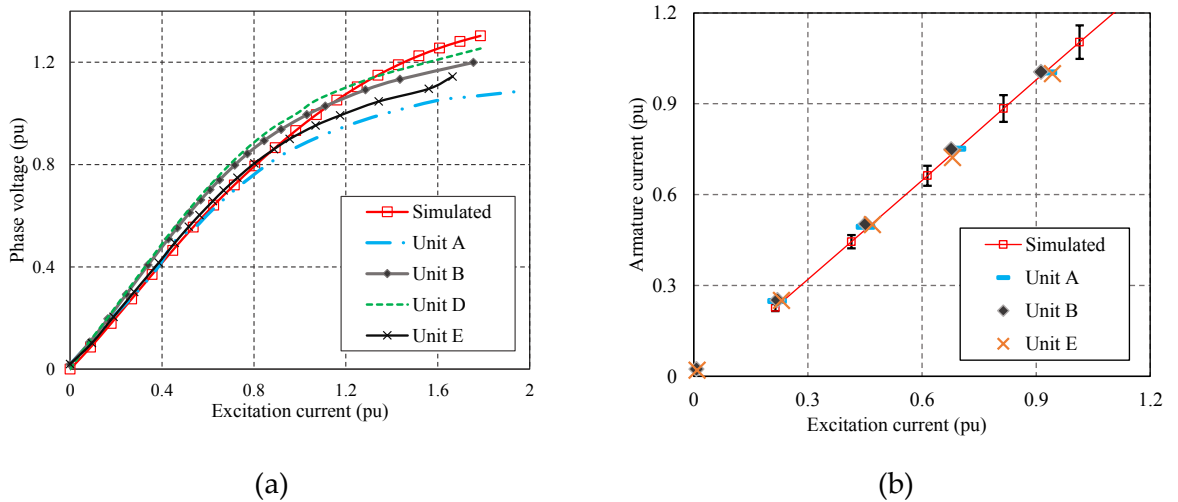


Figure 2-7: Comparison of measured and simulated characteristic curves; (a) open circuit curve, (b) short circuit curve

These results indicate the challenges in simulating units based on only machine dimensions at ideal conditions. At saturation, the units respond differently for several reasons. These include soft magnetic material property deterioration, different manufacturing and assembly tolerances that impact the performance at saturation, change of design parameters due to operation and measurement tolerances that need to be accounted for in the simulated model. Therefore, it is imperative to have more information from experimentally measured results to accurately simulate machine performance in FEA.

The simulated and measured short circuit curve points for the different units are compared in Figure 2-7 (b). Simulated results are shown by a line through points drawn with 5% error bars. Although the simulated is within 5% of all the measured results, a variation in the slopes of the short circuit curves exist. Consequently, a variation in the pu excitation current for rated phase current of 3.8% is obtained as shown in Table 2-3.

These variations in open circuit voltages and short circuit currents result in a variation in the excitation current for rated open circuit voltage (I_{fOC}) or rated short current (I_{fSC}). This amasses to a 15.7% variation in the calculated synchronous reactance (X_{du}) as shown in Table 2-3. Even for the same unit (B and D) the variation in X_{du} observed is 4.4%. All variations are calculated between the minimum and maximum values respectively.

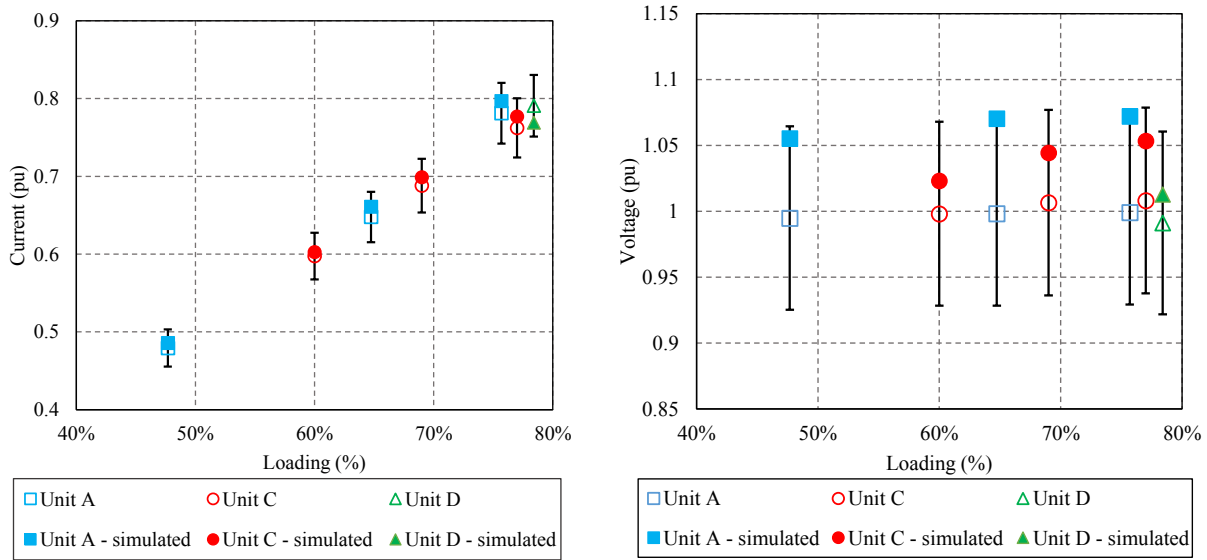
Table 2-3 Synchronous reactance of the units

	I_{f_SC}	I_{f_OC}	
Machine	(p.u)	(p.u)	X_{du}
Simulated	0.922	1.008	0.919
Unit A	0.931	0.995	0.936
Unit B	0.911	0.868	1.049
Unit D	0.912	0.832	1.096
Unit E	0.947	0.948	0.999

2.3.2.2 Comparison of heat run test data

Heat run test points for three units were simulated by imposing the equivalent percentage loading on the machine model. Figure 2-8 (a) and (b) show the pu comparison of the 3phase average rms currents and voltages at different loading. The measured and simulated currents agree within the percentage error bar of 5% as shown in Figure 2-8 (a). The simulated values are generally greater than the measured values except for unit D, where the measured current is 2.8% higher than the simulated current. Unit C had the best correlation with the simulated currents, the percentage error was less than 1.9%.

Simulated voltages were also higher than the measured voltages as shown in Figure 2-8 (b) plotted with error bars of 7%. All simulated voltages for Unit C were within an error of 4.6%. This comparison shows that while numerical modeling gives a good approximation of the machine performance, the numerical model often requires further tuning to accurately represent the machine.



(a) (b)
Figure 2-8: Comparison of measured and simulated heat run test data; (a) open circuit curve, (b) short circuit curve

2.3.2.3 Comparison of air gap flux data

The air gap flux was measured at different loading conditions on unit C, Figure 2-9 shows the comparison of the measured and simulated results at no load and 77% of rated load. Results showed a good agreement at no load in Figure 2-9 (a) and a 12% variation in peak value for 77% of rated load in Figure 2-9 (b); with the simulated values being higher than the measured. This good correlation of the air gap results is in line with the good correlation of the heat run test points for unit C, whose values were closest to the simulation results. It can therefore be inferred that the numerical model as is, can only be used to represent unit C. Unfortunately the OC and SC curve test data for this unit are unavailable to fully ascertain the inference.

2.3.3 Effect of parameter variation on performance

As alluded to in the previous section, for the model to represent any of the units, model tuning is required. In this section, different design parameters are varied and their impact on the open circuit curve quantified. The open circuit curve is used because it is a good depiction of an ideal functioning of the machine without armature reaction, stator copper losses and stray losses.

The machine performance with the changed parameters is compared to the previously simulated machine and two units A and D, whose open circuit voltages are at the lowest and highest extremes respectively as shown in Figure 2-7 (a). Two points of comparison on the open circuit curve are considered; excitation current of 0.357 pu in the linear region, and 1.786 pu in

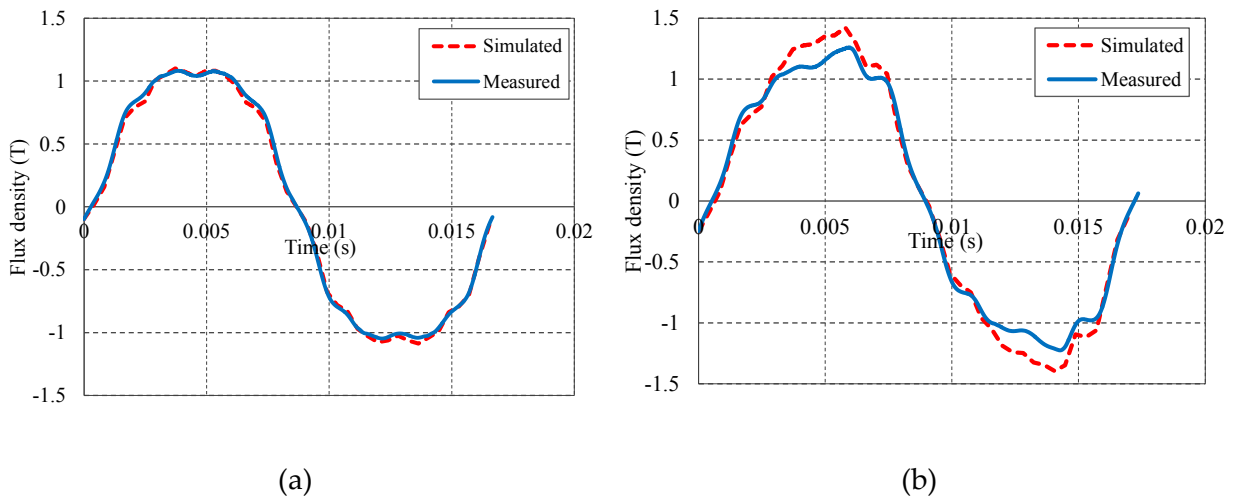


Figure 2-9: Comparison of measured and simulated air gap flux data; (a) No load, (b) 77% of rated load

the non-linear region towards saturation. These exact points are obtained by interpolating or extrapolating the measured data of units A and D using cubic splines.

Comparison of the changed parameters is done with the previous model labeled 'Simulated' and with the units. 'Simulated' represents the FEA model with ideal conditions; design air gap length of 9.92 mm, Epstein measured **BH** curves of the stator and rotor materials, 2D effective length of 750.65 mm. Comparison between models with changed parameters and 'Simulated' indicates the impact of the specific parameter on the open circuit curve, while comparison with the units provides an explanation for the difference in performance between the units.

2.3.3.1 Selecting the effective length

Defining an effective length for 2D simulation of large machines is a challenge because the stator and rotor lengths are different. Moreover, the stator or rotor or both could have radial air ducts of different dimensions located in different places axially along the machine length. In [83] the authors propose a technique to determine the effective 2D length interpolatively using 3D magnetostatic simulations. This method is still very computationally intensive for large diameter machines, therefore was not used in this work.

Alternatively three lengths, which give a good representation of the possible 2D effective length of the generator were simulated; the first effective length was considered an average of both the stator and rotor lengths (770 mm). The second length was computed using equation (3.1) considering the duct loss width coefficient, $k_{bv} = 1$. This assumes that the ducts do not affect the field or flux density in the stator. The length (658 mm) therefore only accounts for the actual magnetic core length in the stator. The third length is when the effects of the ducts are considered in the stator, and therefore indirectly influence the 2D model effective length. A length of 750.65 mm is used for the third case, calculated by using a function for k_{bv} as in [82].

Generally, a longer length gave a higher output voltage as shown in Figure 2-10 (a), where the simulated represents the third length case. Table 2-4 shows that using a length of 658 mm decreases the output voltage by 12% from the 750.65 mm case, and increasing the length to 770 mm increases the output voltage by 3%, in both the linear and non-linear regions. As a result,

the 658 mm values are even less than the values of unit A and only approach them towards saturation. Assuming an average length of 770 mm over estimates the equivalent length because the length of the stator also includes air ducts that are not accounted for. In the rest of this work the effective length of 750.65 mm is considered.

2.3.3.2 Variation of the air gap length

The air gap reduction in a large diameter machine occurs during operation due to rotor breathing, which is the expansion of the rotor especially at high excitation currents. Moreover, the uneven air gap along the axial or radial length of the machine due to eccentricity and/or circularity also significantly affects the effective air gap hence the machine performance [84].

In normal operation of large hydro generators air gap length measurements have shown variations of up to 30% from the design air gap. Any changes in the air gap length result into changes in the air gap reluctance therefore affecting the induced voltage. Some points on the OC curve were simulated with a 10% and 20% reduction in the air gap length. Figure 2-10 (b) shows results for the 20% air gap reduction, labeled 'Air gap'.

Table 2-4 Effect of parameter variation on open circuit voltage

Parameters		Simulated		Unit A		Unit D	
I_r (p.u)		0.357	1.786	0.357	1.786	0.357	1.786
Simulated				1%	22%	-16%	4%
Material	Stator -20% μ	-0.3%	-10%	1%	9%	-16%	-7%
	Rotor -20% μ	-1%	-11%	-0.2%	9%	-17%	-7%
	Stator and Rotor -10% μ	-1%	-11%	-0.2%	9%	-17%	-7%
Stack length(mm)	658	-12%	-12%	-11%	7%	-26%	-9%
	770	3%	3%	4%	25%	-13%	7%
Air gap reduction	-20%	19%	4%	20%	27%	1%	8%
Air gap reduction and material		19%	-8%	20%	13%	0.2%	-4%

*Using percentage difference; negative numbers indicate the simulated values are less than the measured values, the reverse is also true.

Simulated – Stator and rotor materials and airgap as in drawings, stack length 750.3mm.

Material -20% μ – Either only the rotor or stator material permeability is reduced by 20%

Stator and Rotor -10% μ both stator and rotor permeability reduced by 10%

Stack length – Different lengths simulated 658mm and 770mm, the default used for all other simulations is 750.3mm

Air gap plus material – Air gap is reduced by 20% and the material permeability is also reduced by 20%

Comparison of these results with the design air gap labeled ‘Simulated’ in Table 2-4 shows that the reduction in the air gap increases the voltage in the linear region by 19% and by 4% at saturation. Consequently, the open circuit voltage in the linear region agrees with unit D by 1% and at saturation by 8%. Compared to unit A, the difference in the results is 20% in the linear region and 27% at saturation. However, when unit A is compared to results from the design air gap (‘Simulated’), in the linear region there is a difference of 1% while in the non-linear region it is 22%. This suggests that although units A and D have the same design drawings, in operation, unit D has a smaller operational air gap compared to unit A.

The large discrepancy at saturation of units A and D with the simulated, which was higher than both units, hints at another significant modeling parameter, the machine **BH** curves. The effect of the machine **BH** curves at saturation therefore needs to be examined.

2.3.3.3 Variation of the rotor and stator **BH** curve

The general trend in simulated results was high saturation OC voltages, as observed in all the presented simulation results. This indicates that the magnetic material **BH** curves used in simulation have higher saturation than those in the real machines. Therefore, the Epstein measured **BH** curves need to be attuned for the effects of tensile stress and material deformation, which occur at different stages of generator manufacture.

In [85] the authors show a decrease in remanent flux and maximum permeability by over 40% for several deformation levels of less than 20% in low carbon steels. This finding was similar in fully processed electrical steel investigated in [86], where the authors investigated the recovery of some magnetic properties by annealing. For a deformation of 0.5%, the total losses increased by 30%, and highly deformed materials did not fully recover with annealing. Both references reported an increase in core losses and coercive force, a decrease in remnant flux and permeability, as a function of the level of deformation.

The effect of manufacturing processes on the stator core losses is presented in [87] for a small machine and in [88] for laminations. Of all the manufacturing processes like punching, laminating, housing and winding, the laminating process increased the loss by over 25% at the two flux density points tested. This verification of material properties after machine construction

is challenging for large diameter machines with high current and safety requirements. Therefore taking an engineering approach, the permeability of the stator and rotor magnetic materials are reduced by 20% and the new **BH** curves obtained accordingly. The material permeability may be reduced by any amount depending on the level of deformation, a value difficult to ascertain for the entire machine, hence the assumption.

Results with the new **BH** curves are shown in Table 2-4 and Figure 2-10 (c) when only the stator material permeability is reduced by 20%, and when both the stator and rotor materials are reduced by 10%. With the new permeability, the OC voltage at saturation is less than the initially

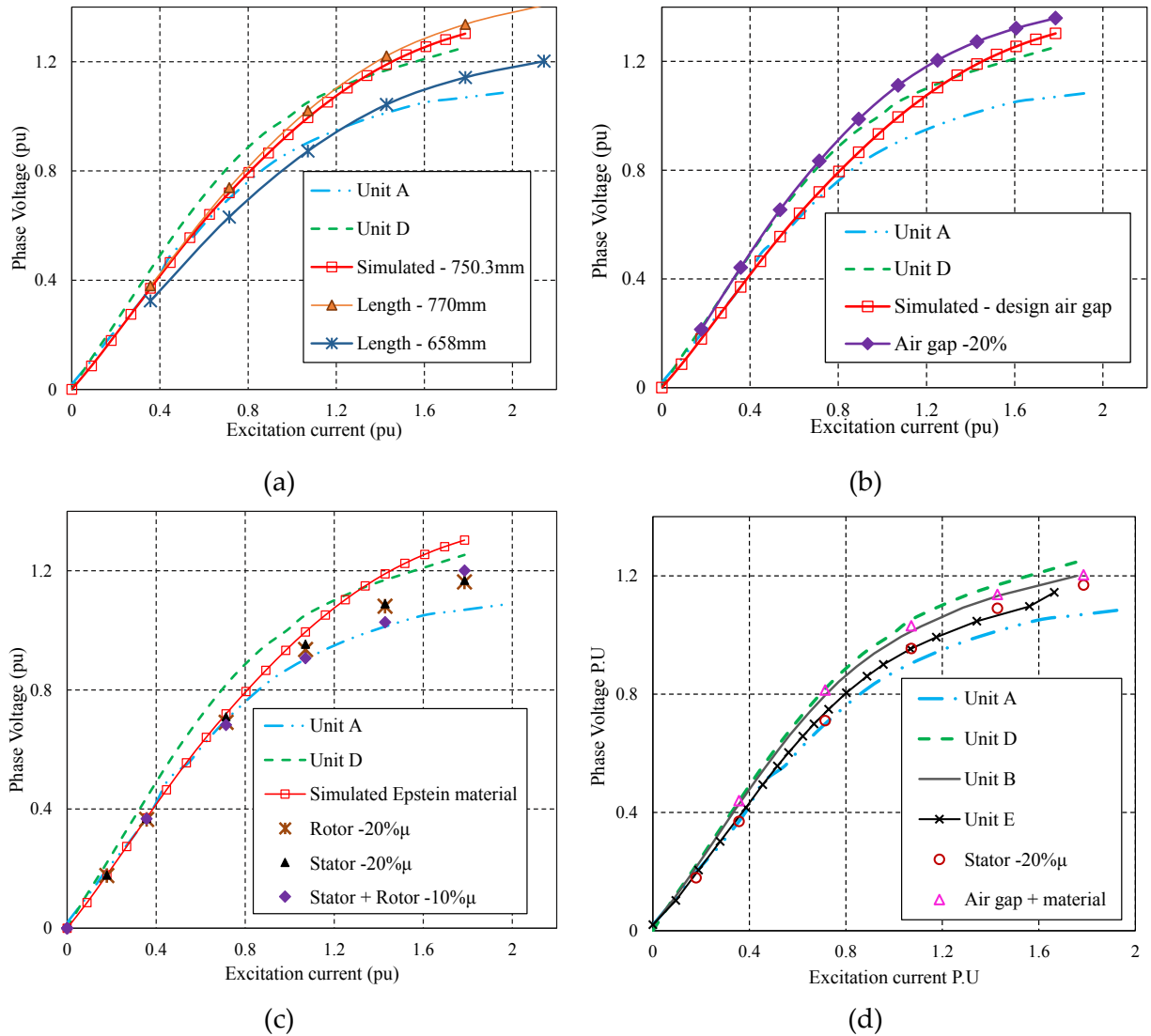


Figure 2-10: Effect of change in simulation parameters; (a) Effective length, (b) Air gap length, (c) **BH** curve permeability, (d) Combination of air gap length and material permeability

simulated by 10%. And when compared to unit A, the difference reduces from 22% with the original permeability to 9% with the reduced permeability. For unit D, the value decreases from 4% above the measured to 7% less than the measured. Reducing the stator material permeability by 20% or reducing both materials by 10% reduces the OC voltage in the non-linear region as shown in Figure 2-10. These results confirm the inadequacy of Epstein measured **BH** curves in numerical modeling of large hydro generators, at least for this set of machines.

2.3.3.4 Residual flux effect

Measured generator test results with no exciter current indicated a voltage at the phase terminals of the units from the residual flux. This residual flux can bias the OC voltage when the excitation current is applied, or contribute to the material saturating at lower excitation. When calculated, the residual flux OC voltage of unit D was equivalent to having an excitation current of 15 A. When this current is accounted for in the simulations, the additional induced voltage was less significant after the linear region.

2.3.4 Final model parameters

While the same machine drawings can be used to model different units, the FEA model needs to be validated to represent a specific unit. Comparison of the simulated and measured results reveal operational and simulation parameters that may be over looked by the design drawings, and need to be accounted for.

As shown in Table 2-4, the difference between the performance of units A, E and unit D is the difference in the operating air gap. Unit D has a smaller operational air gap, 20% less than units A and E. This could be a result of rotor breathing during machine operation or assembly tolerances during installation.

The degradation of material magnetic properties, specifically the permeability is an important aspect to consider when modeling generators. A degradation in permeability of 20% assumed on the Epstein measured **BH** curve of the stator resulted in a more realistic trend in the simulated values, particularly at saturation. This is shown in Figure 2-10 (d), where modification of the stator material **BH** curve, labelled 'Stator -20% μ ' led to a good agreement with results of

unit E. Modification of both the air gap and material also shown in Figure 2-10 (d) resulted in a good agreement between the simulated results and unit B.

A combination of the air gap and **BH** curve properties explains the previous difference between the measured and simulated results. It affirms that a difference in the air gap creates the variation in the output between the units (A and E) and units (B and D). Therefore, FEA simulations showed that it is possible to certainly explain the variations in OC performance of different units with the same design based on the air gap and material properties of the stator magnetic material.

The final model selected represents unit E, with an effective length of 750.65 mm, design air gap length of 9.92 mm and modified stator material permeability. In the next chapter, this model is used to study the distribution of rotational flux in the machine.

2.4 Summary

This chapter fully described the 2D FEA model of the hydro generator used in this work including the geometry, external circuits, and other simulation settings such as time step and type of solver. The challenges to numerical modeling of hydro generators were also outlined. Epstein measured **BH** curves were found to overestimate the permeability and the saturation point of the machine's soft magnetic material, for the generator units considered. As a result the numerical OC voltage at saturation was higher than the measured values.

For machines with the same design dimensions, units A, B, C and E, a change in the simulated material properties and air gap length explained some of the discrepancies in the OC voltages of the different units as shown in sections 2.3.3.3 and 2.3.3.4. The reduction in the effective air gap was about 20% for one of the units, a value within the range of measured air gap lengths.

It is recommended that all 2D FEA generator models be validated using experimental results from the intended machine, before being used for any analysis. This is also applied to machines with the same geometrical dimensions.

The result of this analysis was a selection of the final machine model to represent unit E, whose rotational flux distribution will be determined in the next chapter.

Chapter 3 : Rotational flux Distribution

To appropriately account for rotational core losses in electrical machines, a clear understanding of the rotational flux distribution in the machine under different operating conditions is required, in this case the machine is a hydro generator. This chapter describes how rotational flux in the machine stator can be identified, which leads to the quantification of rotational flux in the machine.

The variation of rotational flux with the stator yoke, air gap length and core operating point are studied as considerations for rotational flux in machine design. Moreover, the studies are verified with real operational machines of different dimensions.

3.1 Definition of rotational flux

A simulation of the 2D generator model with an excitation current of 1090 A, which corresponds to the maximum excitation current at full load. This current was extrapolated from the available heat run tests. Figure 3-1 (a) shows the flux density distribution in a section of the machine, and Figure 3-1 (b) the flux lines. Figure 3-1 (c) indicates the areas where the field is either pulsating or rotating. Figure 3-1(c) i) is an approximation of a pulsating field while Figure 3-1(c) ii) is an approximation of a rotating field. Figure 3-1 (c) iii) and iv) are approximations of elliptical fields, which are special cases of rotational fields. The figures were plotted using the extracted non-sinusoidal flux density waveforms (B_x and B_y) at their respectively labeled stator positions for one electric cycle.

As indicated in the figures, pulsating flux only exists in the stator tooth, while the rest of the stator has two dimensional flux, either rotating or elliptical flux. Therefore estimating core losses using only pulsating core loss models is inadequate for core loss prediction in machines. Moreover, the localization of rotational flux affects the distribution of core losses in the stator core, which could result in localized heating of the core or hotspots.

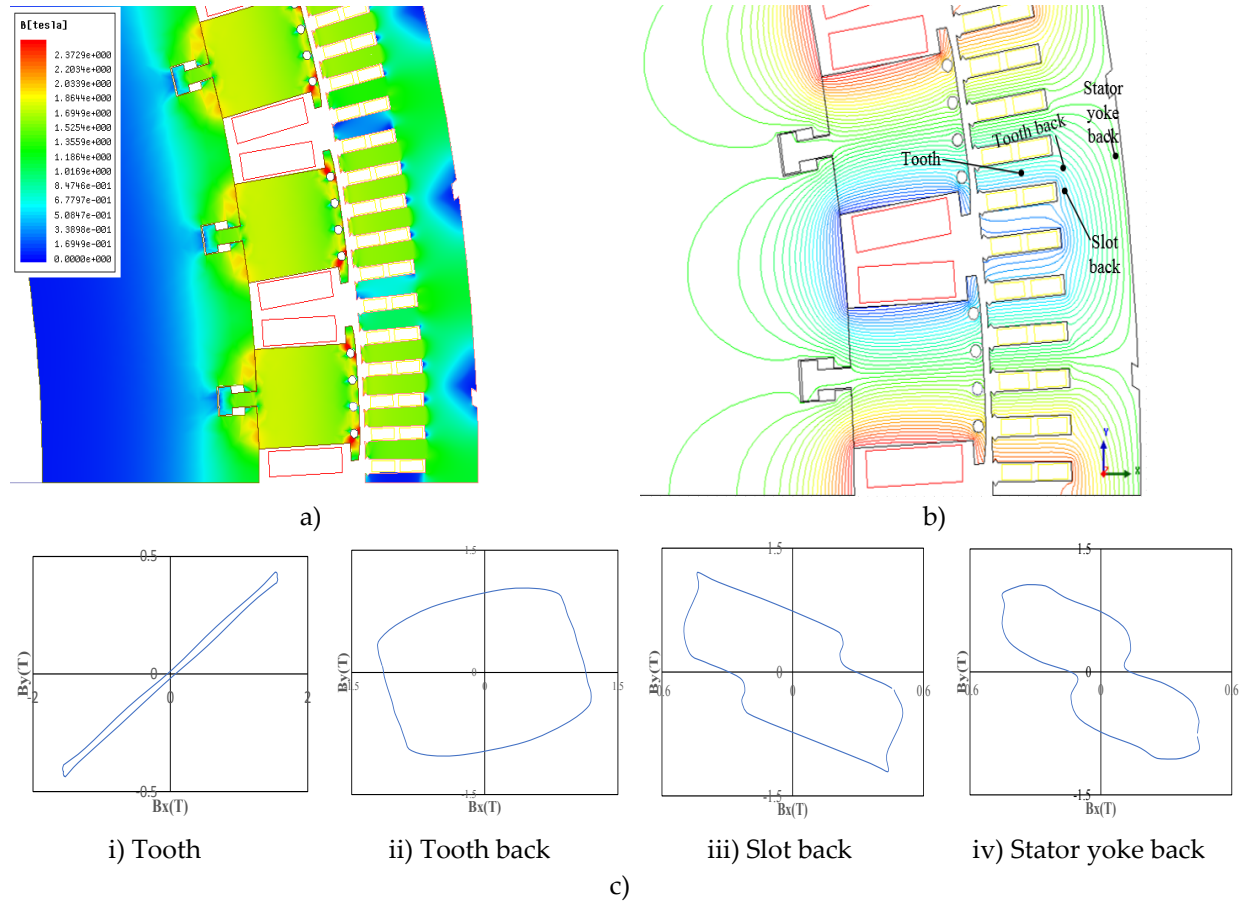


Figure 3-1: Simulation results of the machine model at $I_f = 1090$ A; (a) Flux density magnitude distribution (b) Flux lines (c) Flux density loci at different points in the stator

3.1.1 Aspect ratio

Aspect ratio is used to identify rotational flux distribution in different parts of the stator after post processing the extracted field data. As shown in Figure 3-2, the aspect ratio, R is defined as in equation (3.1)

$$R = \frac{B_{min}}{B_{max}} \quad 3.1$$

where B_{min} and B_{max} are the minimum and maximum flux density as defined in Figure 3-2. This ratio is used to distinguish between pulsating and rotational flux. It is calculated from the fundamental components of the flux density loci.

As seen in Figure 3-2 (b), when $B_{min} = 0$, $R = 0$, the ellipse in Figure 3-2 (b) reduces to a line as in Figure 3-2 (a), signifying pulsating flux. When $B_{min} = B_{max}$, $R = 1$, the ellipse in Figure 3-2 (b)

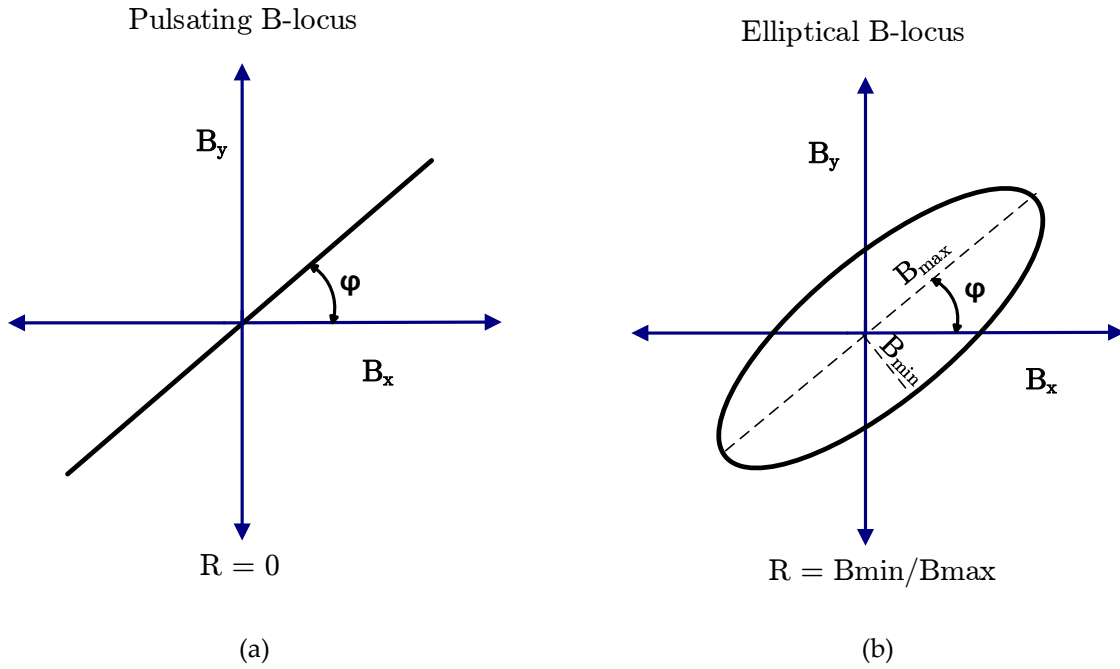


Figure 3-2: Flux density loci; (a) Pulsating flux locus (b) Rotating flux locus

becomes a circle, signifying rotating flux. Any other values of B_{min} result in rotational flux described by ellipses with values of $0 < R < 1$.

The loci in Figure 3-2 are plotted at an angle φ from the B_x axis to account for the orientation of the point geometrically. In cases where the geometrical axis is in line with the B_x axis then $\varphi = 0$.

A fine uniform mesh (maximum length 2.5 mm) is selected for the stator and the simulation repeated. The uniform stator mesh makes the calculated aspect ratio R in the stator independent of the mesh size. Aspect ratio, R is calculated in each mesh element from the extracted orthogonal flux density components and mesh co-ordinates for one electric cycle. The data is only extracted when the simulation reaches steady state, as transients bias the aspect ratio distribution. The spatial distribution of R across the stator in Figure 3-3 is plotted using the calculated R and the mesh coordinates. Most of the stator has rotational flux except the stator teeth and the back of the stator yoke. This is visible in all the non-blue zones where $R > 0$. At the teeth roots the flux is purely rotating with $R > 0.9$ visible by the red zones.

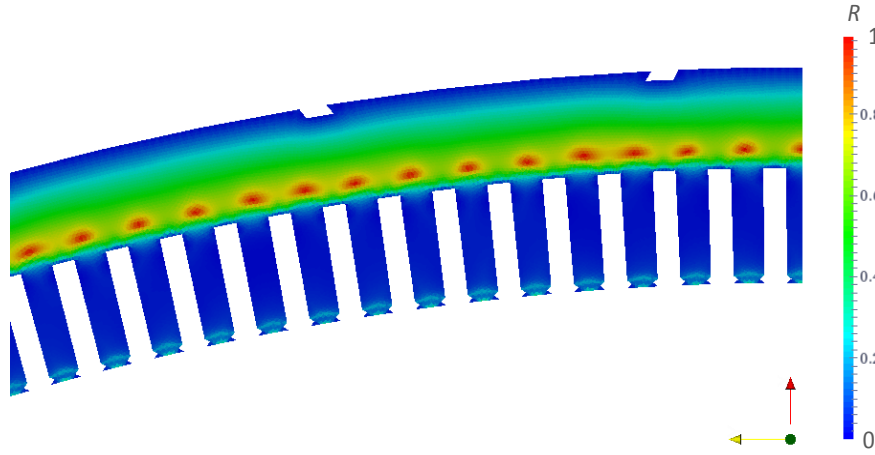


Figure 3-3: Plot of aspect ratio across the stator

3.1.2 Percentage area calculation

Post processing of simulation data involves extracting mesh flux density and mesh coordinates that can be used to obtain the surface area of the stator. Using the calculated aspect ratio in each mesh element, the percentage of stator area with a specific aspect ratio can be calculated using equation (3.2)

$$S_R(\%) = \frac{\sum_{i=1}^n A_i}{\sum_{i=1}^{all} A_i} \quad 3.2$$

where S_R , n , A are the percentage of the stator area, the number of R occurrences and area of the mesh for a specific aspect ratio R respectively. This equation takes into account the weight of each mesh area therefore, can be used when the mesh elements are of different sizes. In this study however, a uniform mesh was used which simplifies the equation by only considering the count of a certain R over the total count of R in the stator. This computed area gives a better understanding of what percentage of the stator has a specific aspect ratio, pulsating or rotating flux. In addition, it can be used to categorize the variation of rotational flux with different parameters.

Table 3-1 shows the aspect ratio distribution using equation (3.2). Results show that 34.2% of the stator area has pulsating flux ($R = 0$), implying that 65.8% of the stator has rotational flux ($R > 0$). Also included in Table 3-1, is the calculation of the aspect ratio using the extracted non-

sinusoidal \mathbf{B} waveforms instead of only their sinusoidal fundamental components. Comparison of both distributions shows that using the extracted non-sinusoidal waveforms reduces the pulsating flux in the stator by 6.7%, which increases the rotational flux ($R > 0$) increases by the same value.

Table 3-1 Aspect ratio percentage distribution in the stator

Aspect Ratio, R		Sinusoidal flux density (%)	Non-sinusoidal flux density (%)
0	Pulsating	34.2	27.5
0.1		15.7	28.1
0.2		9.2	8
0.3		7.9	6.8
0.4		7.4	6.9
0.5	Elliptical	7.5	8.2
0.6		8.7	9.9
0.7		5.8	3.9
0.8		2.7	0.7
0.9		0.8	0
1	Rotating	0.1	0

This no load $I_f = 1090$ A simulation point is considered the base case, which is defined by the design air gap length and design stator yoke depth. The subsequent studies compare the rotational flux distribution of this machine design and different designs using S_R .

3.2 Variation of the rotational flux with design and operating point

Rotational flux distribution in small machines has been shown to vary with pole pitch, stator tooth width [89] and stator yoke length [90]. In [91], an analytical model was proposed to characterize flux density in the stator core from slot dimensions. The studies however did not quantify by how much the rotational flux varied with the change in geometric dimensions. Moreover, the analysis was limited to smaller sized machines, specifically induction machines. Large diameter machines include different dynamics that may be neglected in the analysis of smaller machines.

This section therefore uses S_R to study the variation of rotational flux with the stator yoke depth, air gap length and operating point of the machine. The study with change in geometrical parameters provides considerations for machine design in relation to rotational flux distribution, while the change in operating point uses a given machine design, and studies the variation of rotational flux with the core **BH** curve operating point. The distribution of rotational flux is important as it relates to the non-uniform distribution and the total calculated core losses.

3.2.1 Yoke depth influence on rotational flux distribution

The effect of varying the yoke depth on the rotational flux distribution was studied using a constant excitation current. This ensured the same operating point on the machine **BH** curve. Thus, any variation in rotational flux is entirely related to the change in the yoke depth.

All stator dimensions are kept constant, and only the yoke depth is varied. The slot/yoke depth ratios simulated are 1.23, 1.10, 0.99, 0.90 and 0.83, which correspond to -20 %, -10 %, design length, 10 % and 20 % variation in yoke depth, respectively. These values were selected to allow for variations in yoke depth due to errors, margins or tradeoffs made in the machine design stage. Figure 3-4 shows the variation of the rotational flux distribution in the stator with yoke depth. As the yoke depth is increased, the stator area with rotational flux increases, specifically for $R > 0.7$, which is visible with the increase of the red zones as the yoke depth is increased.

A numerical representation of the results is presented in Figure 3-5, where the pulsating component ($R = 0$) reduces as the yoke depth is increased, inferring an overall increase in rotating flux. For instance from a 20% smaller yoke to a 20% larger yoke than the design, the pulsating flux reduces by 3.2%. For $0.1 \leq R \leq 0.5$, the area of the stator with rotating flux also reduces with increase in the yoke length. Comparing the 20% smaller yoke to the 20% larger yoke, the rotational flux reduces by 9.7%. However for $0.6 \leq R \leq 1$ the area of the stator with rotating flux increases with yoke depth. The rotational flux increases by 15.9% between the 20% smaller yoke and the 20% larger yoke. This is visible by comparing the design length (green bar) with the 20% increase in yoke length (yellow bar), which increases the rotational flux by almost twice, especially for $R = 0.8$, $R = 0.9$ and $R = 1$.

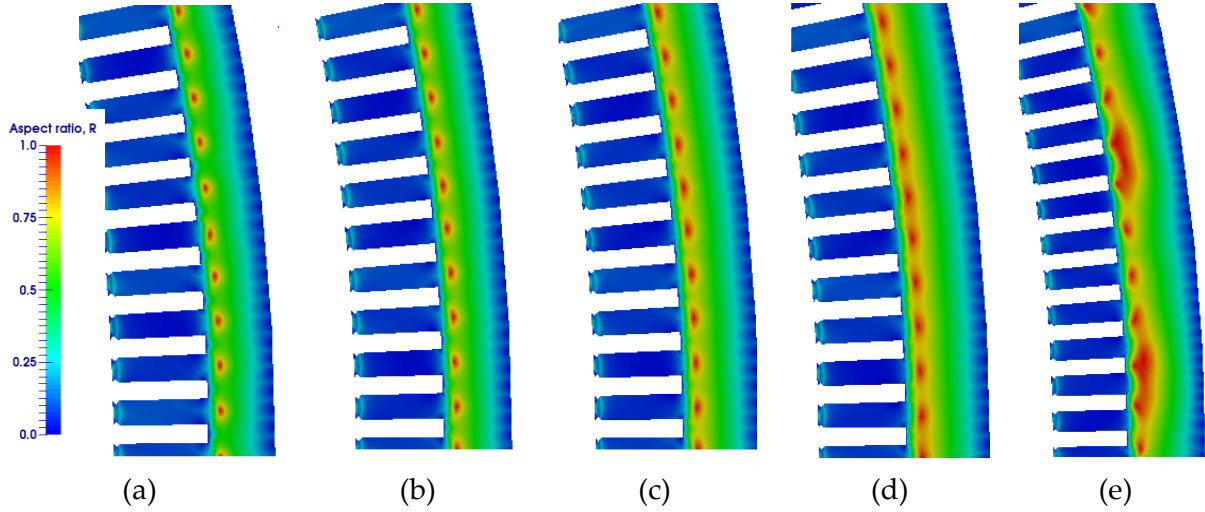


Figure 3-4: Aspect ratio, R for different yoke lengths; a) 20 % less than the design length; b) 10 % less than the design length; c) design length; d) 10 % more than the design length and e) 20 % more than the design length.

3.2.2 Air gap length influence on rotational flux distribution

Thermal expansion of the rotor during machine operation can lead to a variation in the air gap length. Eccentricity and circularity of both the rotor and stator can also cause a non-uniform operational air gap different from the design air gap, sometimes even axially along the machine. This has an effect on the air gap flux magnitude and harmonics, which impact the machine total core losses in the stator.

The air gap was decreased by 10 % and 20 % as shown in Figure 3-6, where the stator area with pulsating flux ($R = 0$) decreases with the air gap. For $R = 0.1, 0.2, 0.7, 0.8$ and 0.9 , the rotating flux increases. Between $R = 0.3$ to $R = 0.5$ the rotating flux in the machine remains almost constant. The 10% and 20% decrease in air gap length, reduced the pulsating flux by 6.6 % and 8.8 % respectively in comparison to the original design.

For variation in the yoke depth and air gap length studied, a constant field current was assumed. However, in the actual design, increasing the yoke depth while maintaining the same rated voltage may require an increase in the excitation current because the volume of the stator increases. And in the case of the air gap length, decreasing the air gap length may require a

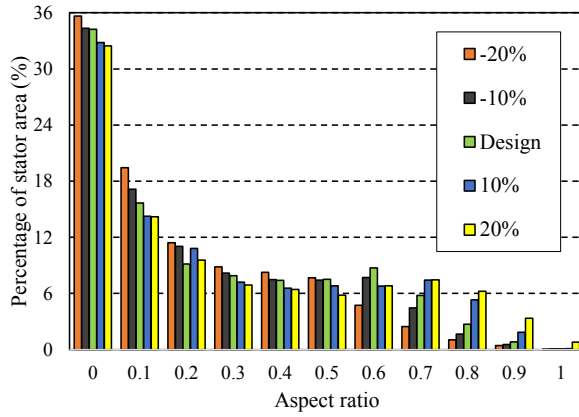


Figure 3-5: Effect of increase in yoke depth on rotational flux distribution.

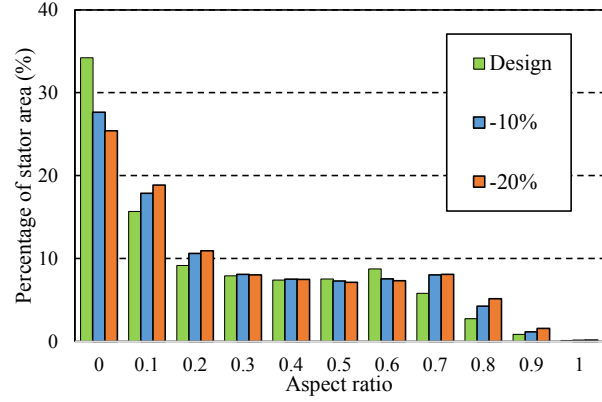


Figure 3-6: Effect of change in air gap length on rotational flux distribution.

decrease in the excitation current for the same open circuit voltage, as the air gap reluctance is reduced.

3.2.3 Influence of the machine BH curve operating point on rotational flux distribution

The point of operation is indicative of where on the **BH** curve the stator is operating. Examples of the machine operating at different points on the core **BH** curve occur in the comparison of the no load and full load operation, change in machine power factor and change in the percentage loading. These operating points require a change in the field current that also causes a change in flux density level in the stator. Other variations in field current can occur after a machine uprate.

In this section, the effect of the machine operating point on rotational flux distribution is studied. This is done on an existing machine design, therefore the machine dimensions are maintained constant and only the **BH** curve operating point is changed. Open circuit simulations with different field currents, which sequentially change the flux density level in the stator, are used. The other set of results is obtained by varying the output power of the machine, which changes the power, but maintains the same **BH** curve operating point.

3.2.3.1 Saturation

The effect of saturation on rotational flux distribution in the stator is shown by increasing

the excitation current. Different excitation currents (I_f) are chosen for simulation as shown in Figure 3-7. The excitation current for the linear region is $I_f = 401$ A, the excitation current for rated voltage is $I_f = 560$ A, the excitation current in the non-linear region $I_f = 900$ A, and $I_f = 1090$ A which corresponds to full load excitation current.

Figure 3-8 shows a section of the generator model indicating four points in the stator selected to represent different sections in the machine; the stator tooth, back of the tooth, slot back and stator yoke. Flux density waveforms for one cycle are extracted at these points as the excitation current is varied. Figure 3-9 shows the loci of the extracted B_x and B_y waveforms at each of those respective points. All the waveforms are non-sinusoidal as characterized by the irregularly shaped loci, which expand as the current is increased. Additionally, as the material saturates the flux density magnitude increases and the waveform shapes change accordingly. This is clearly observed by comparing the flux density loci corresponding to the lowest and highest excitation currents simulated, 401 A and 1090 A.

As the material saturates, changes in the flux density waveforms occur at different points in the machine. For instance at the back of the tooth, the flux loci becomes more circular with increasing excitation current. These changes affect the aspect ratio distribution within the stator of the machine. Figure 3-10 (a) and (b) show a plot of the aspect ratio for the stator with $I_f = 401$ A and $I_f = 1090$ A. There is an increase in the $R = 0.2$ visible around the ends of the stator tooth for

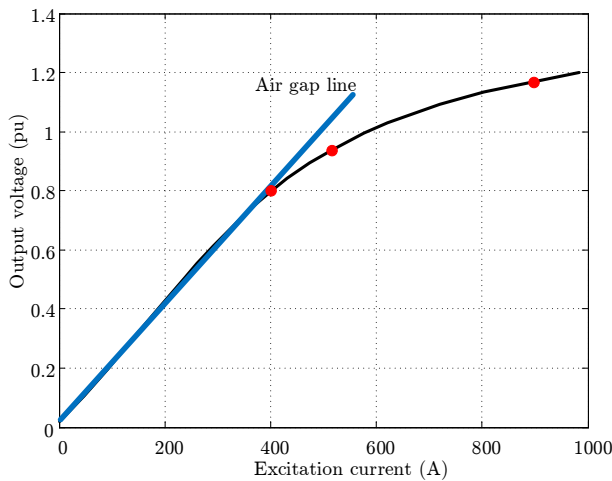


Figure 3-7: Measured open circuit curve of the 19 MVA generator showing simulated points.

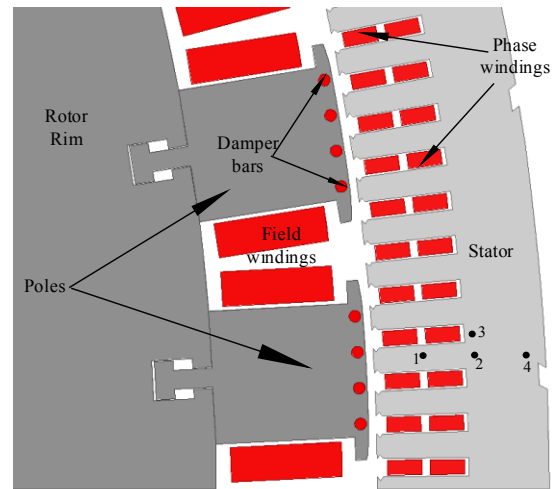


Figure 3-8: 2D FEA model showing points where field data is extracted.

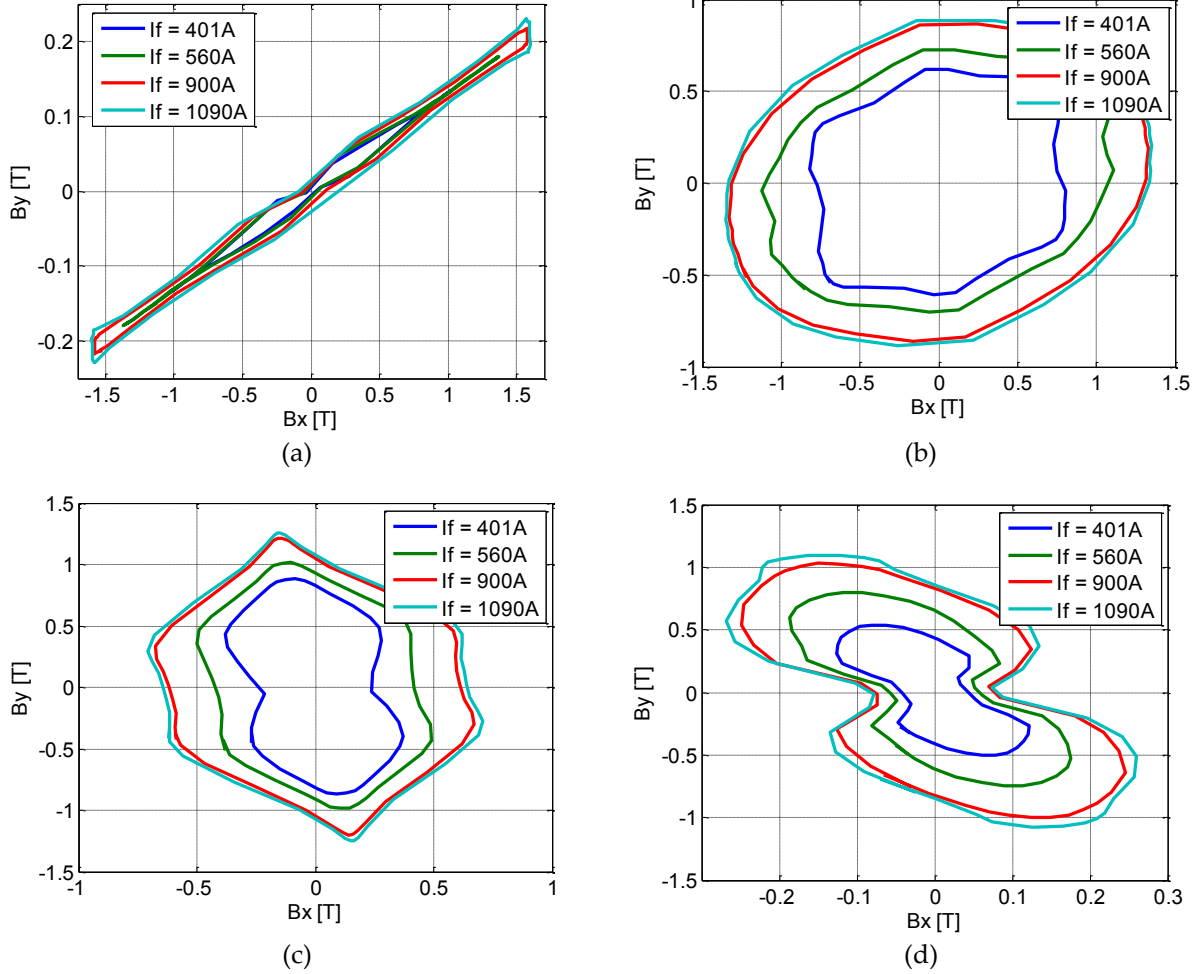


Figure 3-9: Flux density loci at; a) Point 1: middle of the tooth b) Point 2: Back of the tooth c) Point 3: Back of the slot d) Point 4: Back of the yoke

the $I_f = 1090\text{ A}$ aspect ratio plot. The rotational flux with $R > 0.6$ also increases with I_f , visible by an increase in the red and yellow zones of Figure 3-10 (b).

A numerical representation of this is shown in the bar graph of Figure 3-11, which also includes results obtained from the other simulated currents. As the current is increased and the material saturates, the pulsating flux ($R = 0$) reduces by 2.76% comparing $I_f = 560\text{ A}$ to $I_f = 1090\text{ A}$ as seen in Figure 3-11. For aspect ratios $R > 0.5$ the rotating flux generally increases with current. For example at $R = 0.7$, rotational flux increases from 1.96% at $I_f = 401\text{ A}$ to 7.54% at $I_f = 1090\text{ A}$. In conclusion, increasing the excitation current, which relates to the BH curve operating point, results in an increase in rotational flux for $R > 0.5$ and a decrease in rotational flux for $R < 0.5$.

3.2.3.2 Percentage loading

Operation of the machine under different loading conditions was also investigated as shown in Figure 3-12. The excitation current for each condition was obtained based on the available experimental data at different machine loadings. External circuits were used to emulate the different machine loads connected to each phase. For the different loads, the change in rotational flux distribution was insignificant. However a comparison of no load and any loaded condition shows huge differences in the flux distribution.

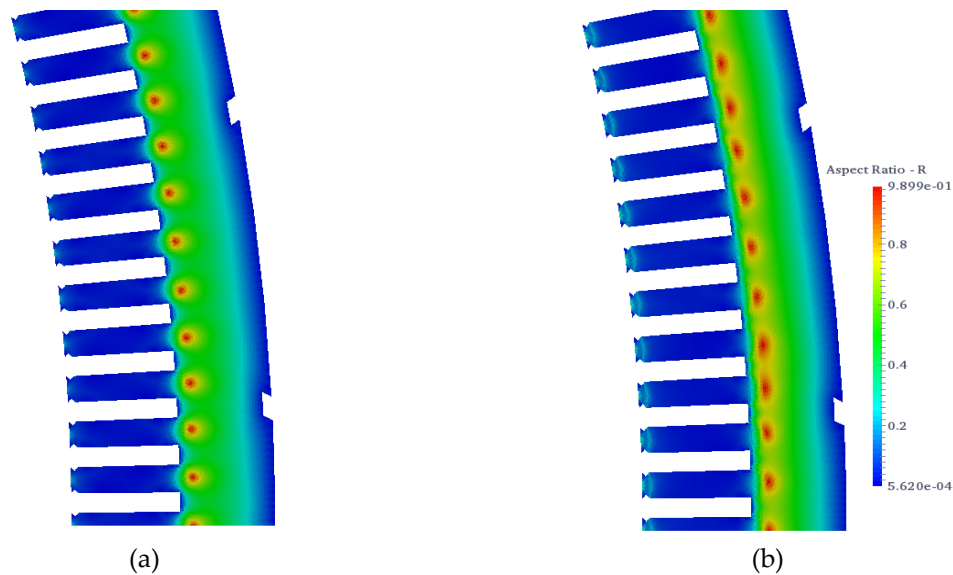


Figure 3-10: Effect of saturation on rotational flux density distribution; (a) $I_f = 401$ A, (b) $I_f = 1090$ A

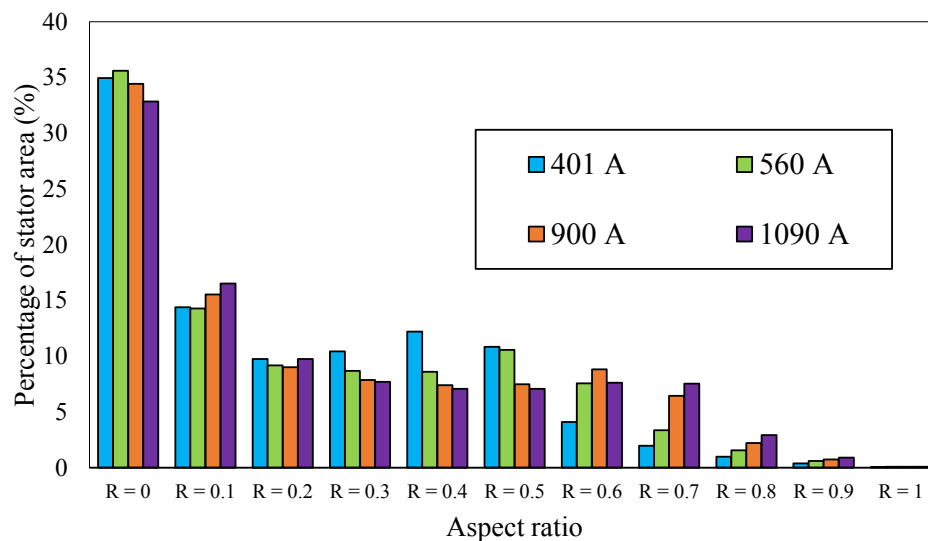


Figure 3-11: Effect of saturation on rotational flux density distribution using stator area

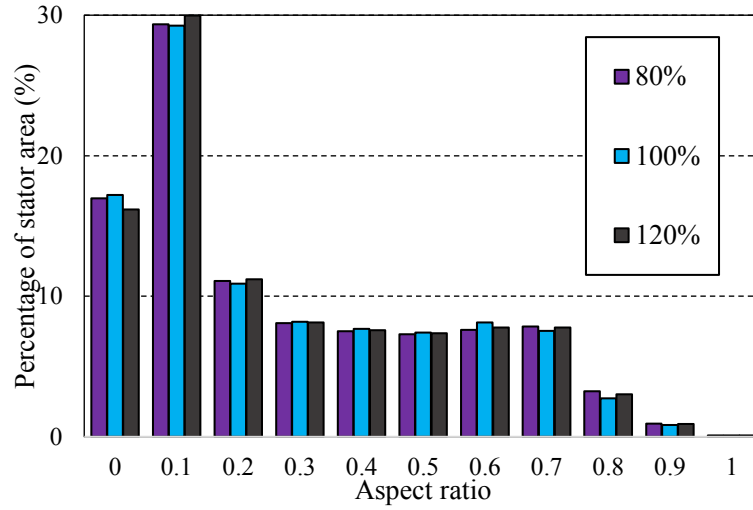


Figure 3-12: Percentage of stator area verses aspect ratio at three machine loadings

3.3 Discussion of the results

In previous the yoke variation studies, an increase in the yoke depth increases the percentage of rotational flux in the stator. Although one would argue that for the same excitation, a large stator yoke implies a lower flux density magnitude, and therefore a lower loss. However, since rotational flux presents more losses than pulsating flux for the same flux density magnitude, a large distribution of rotational flux generally increases the losses in the yoke even at relatively lower flux densities than in the teeth.

Variation of the air gap showed a 6 % increase in the stator area with rotational flux for a 10 % decrease in air gap at no load. For a 20 % decrease in the air gap, an increase of 8 % in the stator area with rotational flux was observed. This implies that further decrease in the air gap has the potential to increase the rotational flux. Moreover, a decrease in the air gap corresponds to an increase in the flux density level in the machine. Both factors would significantly increase the core losses in the machine.

As the material saturates, the rotating flux component for $0.6 \leq R \leq 1$ increases from 7.4% to 19% for current increase from $I_f = 401$ A to $I_f = 1090$ A. Consideration should therefore be given to the choice of maximum core flux density in the design stage, specifically the stator yoke, which has rotating flux.

Increase in output power did not show a significant increase in the percentage of rotational flux when the load was increased from 80% to 120% for the same power factor. This can be attributed to the core already operating at saturation and therefore any increase in power does not yield a significant change in the flux density distribution. However, in comparison to the no load case, there is a difference in the flux distribution.

Aspect ratio distribution does not take into account harmonics and flux density magnitude which are also affected by the air gap length and the output of the machine. Increase in output power and decrease in air gap length increased the magnetic loading of the core and therefore more losses.

These results provide a guide line in the required measurements of rotational loss data. Ideally even with the presence of all this rotational flux, if the flux magnitude is very low, the contribution of the rotational losses to the total core losses will be low. Knowing the percentage of rotational flux and its distribution provides a base for developing a model that can sufficiently predict total core losses in generator stators based on the flux distribution.

3.4 Different machine designs

Previous results showed the variation in rotational flux distribution with changes in the stator yoke and air gap lengths. The results were based on varying the parameters of an existing design, which may not be realistic as machines are optimized for certain ratings and meet certain design criterion. This section compares already existing machines to present a more realistic variation in the rotational flux distribution with machine parameters.

Table 3-2 shows the parameters of different hydro generators compared in this study, where Machine 1 is the previously designed machine. The other machine models were prepared in the same 2D FEA software. For each machine the tooth/yoke depth ratios are as follows 0.99 for Machine 1, 0.699 for Machine 2, 0.928 for Machine 3 and 1.310 for Machine 4. Using the magnetic and winding symmetry, 17 of 68 poles are modeled for Machine 2, 5 of 60 poles are modeled for Machine 3, and 19 of 76 poles are modeled for Machine 4. Appropriate boundary conditions are applied to the model boundaries, and the skew in Machine 2 is ignored.

For comparison purposes, the simulations for each machine are done at the excitation current for rated voltage in open circuit. Figure 3-14 shows the aspect ratio distribution for each machine, which indicates the dependence of the rotational flux distribution on machine dimensions. The increase in the red and yellow zones indicate the increase in rotating flux with $R > 0.8$, which is seen to increase from Machine 4 to Machine 3, then to Machine 1 and lastly Machine 2 with the largest red zones. Machine 2 further has the largest green zones with $0.4 \leq R \leq 0.6$ rotating flux, signifying an expected increase in rotational core losses in Machine 2 compared to other machines.

A quantitative distribution of rotational flux in the machines is shown in Figure 3-14, which highlights the pulsating flux in each machine with the green color. The rest of the flux is rotating with different aspect ratios, $R > 0$. A large pulsating flux signifies less rotational flux and vice versa. The difference in machine size and dimensions captures the effect of machine dimensions on the rotational flux distribution.

Table 3-2 Machine parameters

Machine	1	2	3	4
Power rating (MVA)	19	32.5	122.6	65
Voltage (kV)	13.8	13.2	13.6	13.8
Current (A)	795	1422	5129	2719
Excitation current I_f (A)	1090	875	726	1220
Power factor	0.8	0.8	0.9	0.85
Frequency	60	60	60	60
Speed (rpm)	120	105.9	120	94.7
Poles	60	68	60	76
Slots	336	432	504	396
Slots per pole per phase	1 13/15	2 2/17	2 4/5	1 14/19
Dimensions				
Tooth width (mm)	32.11	33.6	42.94	48.71
Tooth depth (mm)	112	146.304	159	160
Yoke depth (mm)	113	209.296	171.3	122.05
Air gap (mm)	9.92	11.887	15.9	12.7

Machine-3 had the largest percentage of pulsating flux hence less rotating flux, which can be attributed to a combination of a large air gap and a smaller yoke depth i.e. ratio of slot/yoke depth of 0.928. The yoke depth is not oversized and therefore the rotating flux is limited. These results are consistent with the previous results in section 3.2, where rotational flux increases with the decrease in air gap length and increase with yoke depth.

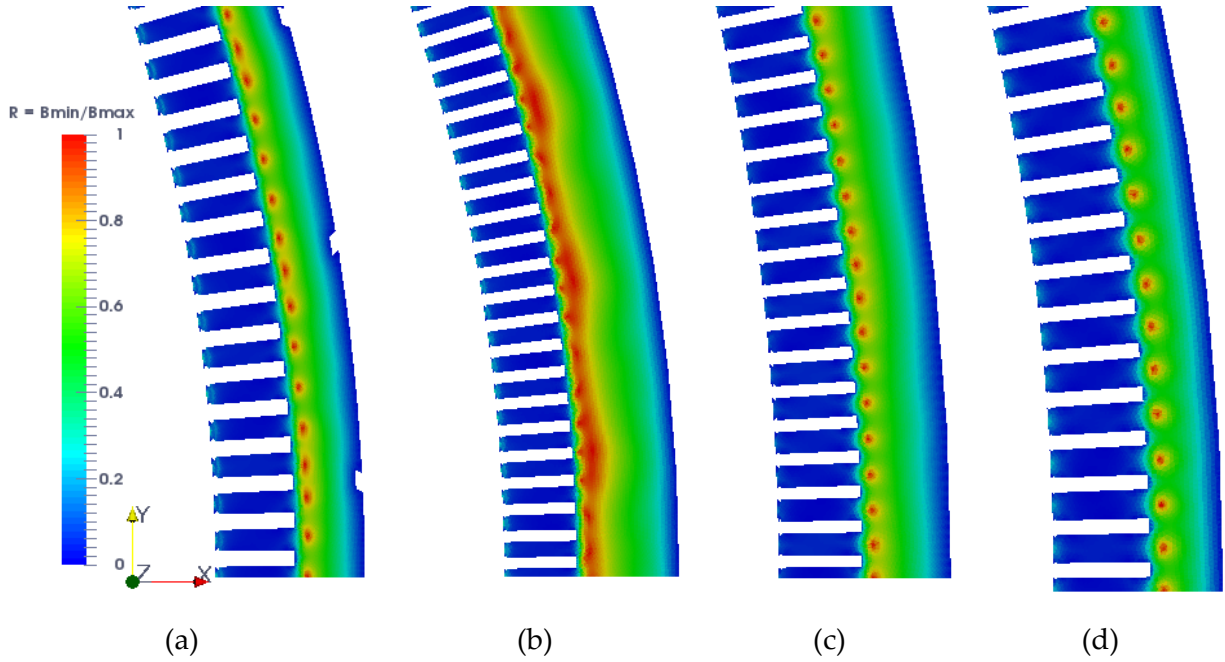


Figure 3-13: Aspect ratio distribution in different machine designs; (a) Machine 1, (b) Machine 2, (c) Machine 3 and (d) Machine 4

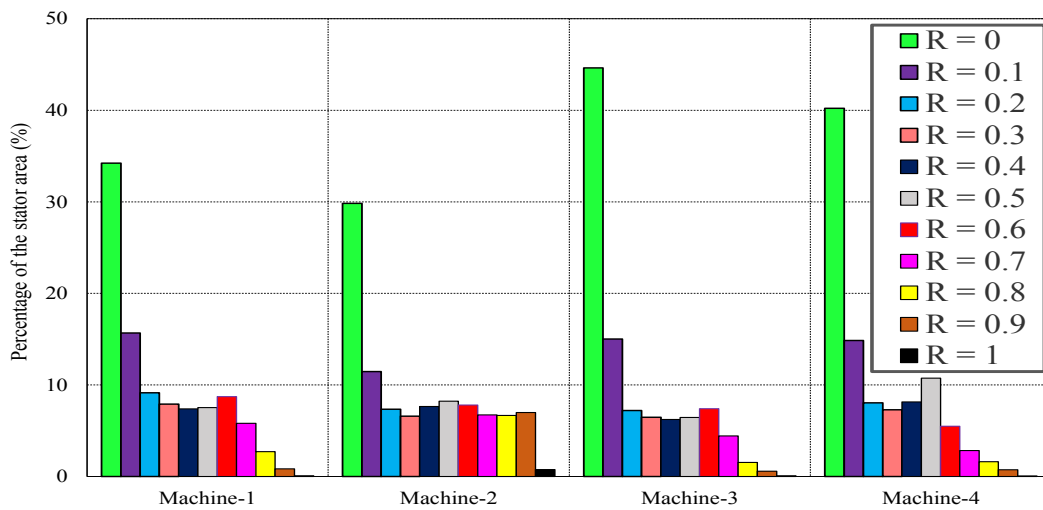


Figure 3-14: Comparison of the aspect ratio - R variation in different machines under open circuit conditions.

Machine-4 had the next largest pulsating flux, its dimensions follow the same trend of a larger air gap compared to Machine-2 and Machine-1 and an even smaller yoke depth than Machine-3. The slot to yoke depth ratio for Machine 4 was 1.310, it's yoke depth is smaller than the slot length. Machine-2 had more rotating flux compared to Machine-1 despite having a slightly larger air gap. This is because the yoke depth of Machine-2 is longer which diminishes the effect of a large air gap as seen from the comparison of the slot/yoke depth ratio; Machine-2 is 0.699 and Machine-1 is 0.99. Consequently, Machine-1 design has a tradeoff between the small size of the air gap and the yoke length that evens out; giving less rotational flux than Machine-2.

3.5 Summary

In this chapter, rotational flux distribution in the machine is obtained and quantified as a percentage of the stator area with rotational flux. The quantified rotational flux distribution was used to study how rotational flux varies with the machine design (yoke depth and airgap) and operating point (on the **BH** curve and loading).

From the base case results, the pulsating flux occupies about 34 % of the stator, which means the remaining 66% is rotational flux, which includes all aspect ratios $0 < R \leq 1$. The distribution of rotational flux was sensitive to design parameters; rotational flux increased with a smaller air gap length and a longer yoke depth. This was verified with different machine topologies.

Increasing the operating point from the linear part of the **BH** curve to the saturation point, also showed an increase in the rotational flux. This provides an aspect to consider in machine design and operation, which is, that the core should not be operated at saturation.

The results from this chapter will be considered in the core loss measurement and estimation in the following chapters.

Chapter 4 : Magnetizer Design Core Loss Measurement

Core loss estimation requires measured core loss data of the material samples used in the machine. Commonly available material data is based on the standard Epstein test, which is insufficient for core loss prediction in machines with rotational flux, as was shown in the previous chapter. Therefore, in this chapter a rotational flux magnetizer is designed and prototyped. Factors in the FEA design process such as the effect of sample diameter, winding distribution, number of slots, and yoke thickness on the flux density uniformity in the sample are presented.

A full description of the test bench is given including the software block diagrams used. Safe operating procedures for the rotational test setup are included in the appendix. Rotational core losses at different frequencies, flux densities and aspect ratios are measured and used in the next chapter to estimate core losses in the generator. Measurement results on loss separation are also presented.

A previously designed rotational test bench is also used to study the effect of interlaminar faults on rotational flux distribution and core losses. Numerical and experimental results are presented.

4.1 Design of the magnetizer

The design of the magnetizer started from the analysis of the existing state of the art test setup in the IREQ laboratory. Analysis of the 2 phase, 8 pole, 5 mm yoke depth frame with a 58 mm diameter sample was performed in 3D FEA. The inadequacy of the magnetizer led to a design of another frame based on the magnetizer design presented in [28].

In the proposed design, a larger sample diameter allows a 65 by 65 mm measurement area. Moreover, the combination of the winding distribution and the yoke depth reduce the z-component of the magnetic field intensity in the sample measurement area. This section presents the design process and analysis.

4.1.1 State of the art

From literature and previous prototypes in [16], [19], [92] and [28], the state of the art is to distribute the phase windings for a more uniform field distribution in the sample. An example of this is shown in Figure 4-1, where the winding is distributed. The 3D FEA model of the 8 pole, semi-distributed 2 phase winding magnetizer capable of producing a rotating magnetic field in a circular sample. This magnetizer design is based on a magnetizer previously used to magnetize and levitate a disk in a rotating field during heat treatment. Its ability to generate a uniform rotating field in a circular disc sample was investigated.

The dimensions of the magnetizer are; yoke depth of 5 mm, outer diameter of 120 mm, and inner diameter of 60 mm enclosing a sample of 58 mm diameter. The magnetizer is modeled as a solid with a stacking factor of 0.96 in the z direction. A sample of gauge G29 was considered with 0.3556 mm depth. An air box with a 10% padding offset on each side of the magnetizer outer dimensions was used to limit the simulation space and stray fields.

Figure 4-1 (b) shows the winding distribution consisting of concentrated phase windings with 50 turns on the direct axes and 35 turns on the middle poles. The middle pole turns are alternated to increase the air gap MMF uniformity. These concentrated windings are modeled as

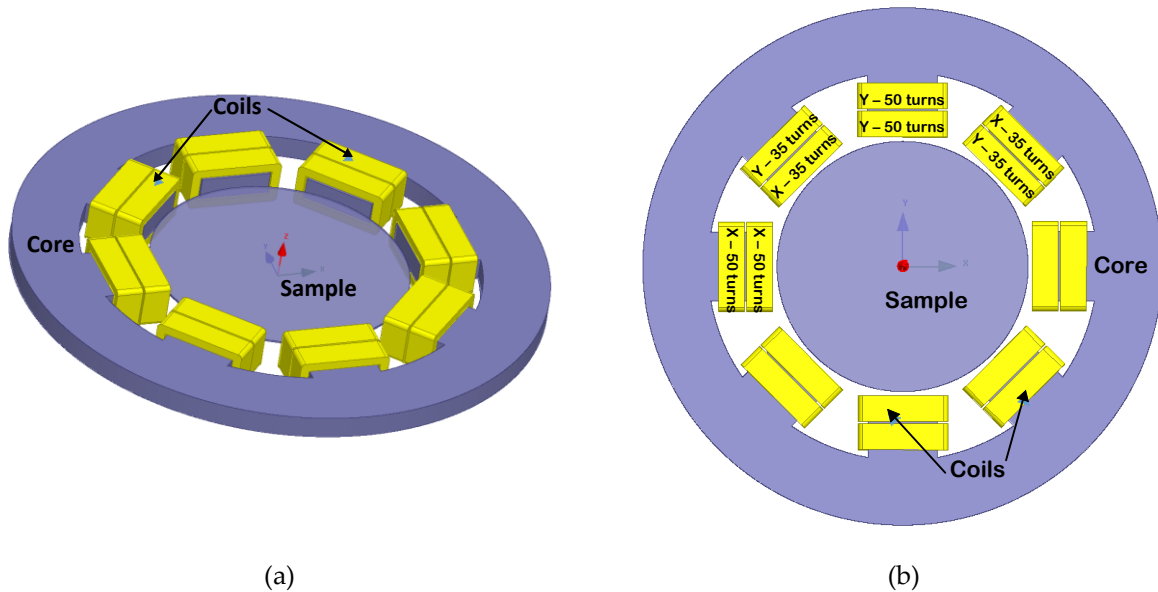


Figure 4-1: 8-pole magnetizer, (a) 3D model, (b) 2D view with the coil number distribution.

solids with their respective number of turns as the number of conductors in the coil terminal. Each coil is assigned to a stranded winding with the appropriate current direction to allow the flux to flow through the sample from one pole to its opposite pole.

The same magnetic material is used for both the sample and the magnetizer to avoid any effects of the difference in material permeability. Meshing in the yoke, sample and concentrated windings are also selected to ensure continuity in the flux distribution without being very dense to require longer processing time and more memory. Transient simulations with a time step of 1 ms for one electrical cycle is used and the field data saved for post processing.

Simulations to ensure uniformity of the field in the sample are performed with a peak sinusoidal excitation current of 10 A per phase, and a 90° phase shift between the phases. As shown by the flux density distribution in the frame and sample of Figure 4-2 and Figure 4-3, the field distribution in the sample is non uniform. Moreover, the yoke also shows significant levels of flux density. This implies that the yoke can easily get saturated therefore introducing some non-linearities in the sample, which bias the measured sample fields.

The non-uniformity in the flux density distribution in the sample also varies with the rotating flux vector. This is shown by the difference in the flux density distribution in the sample in Figure 4-2 and Figure 4-3, where the flux vector is 45° from the x axis and directly on the x axis respectively. Consequently, defining a measurement area on the sample is difficult as the measurement area is required to have uniform flux distribution in all the flux vector rotations/magnetization directions.

Modifications to the yoke like tapering of the poles, changing the winding configuration, increasing the number of poles and dimensions of the yoke and sample did not yield significant differences in the sample field uniformity for all magnetization directions. An analysis of some yoke designs is presented in [28], where a stator core yoke design with a sinusoidally distributed winding is reported to have uniform field distribution in the sample for all measurement directions. This stator yoke design is adopted and suited to meet the size of available material samples, as presented in the next section.

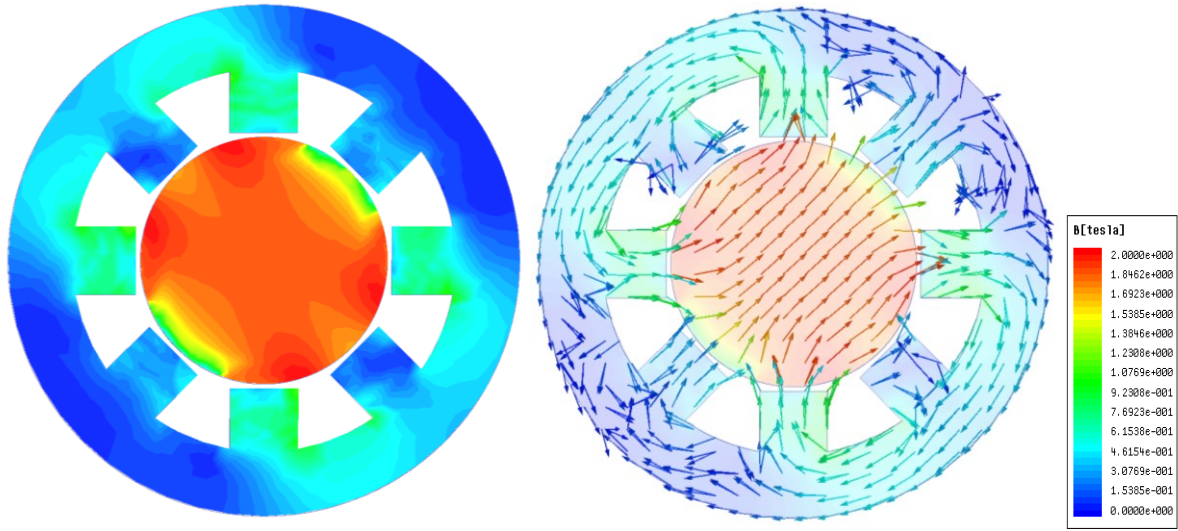


Figure 4-2: Field distribution with current of 10 A for the flux vector at 45° from the x, (a) Flux density distribution, (b) Flux vector..

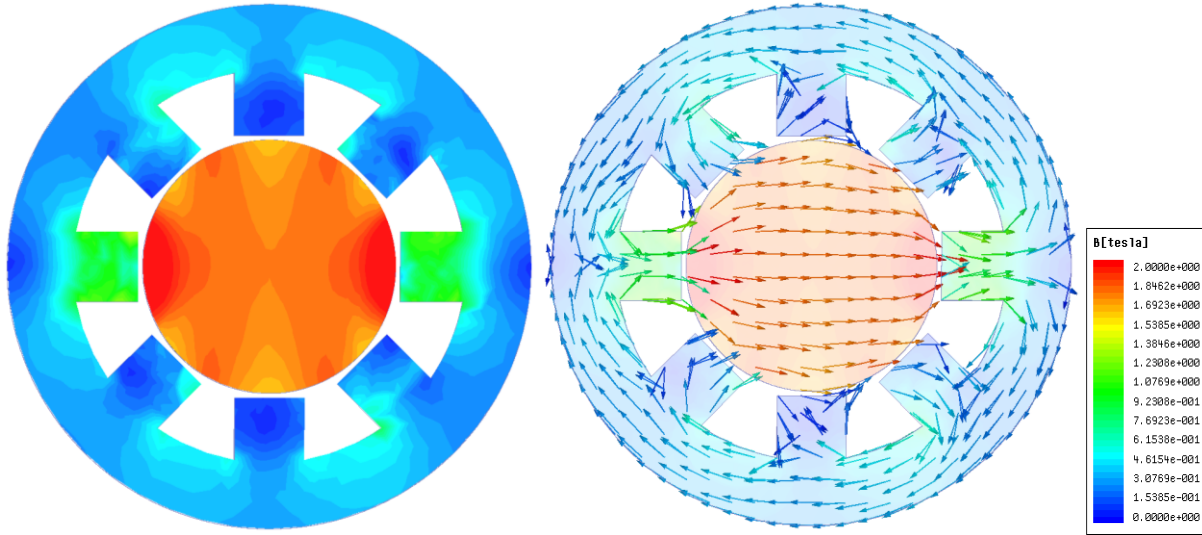


Figure 4-3: Field distribution with current of 10 A for the flux vector in the x, (a) Flux density distribution, (b) Flux vector.

4.1.2 Proposed magnetizer

Characterizing generator cores is a challenge as most of the generators are old and the core material used is unavailable. The only core material available for characterization of the old generator cores is the shims used to level the stator yoke, whose width is 150 mm. Moreover, the thickness of the shims is uneven especially at its edges, therefore the magnetizer inner diameter was set to 140 mm. This limits the sample diameter to less than 140 mm, where the shim thickness

is even. Furthermore, as shown in [28], wider diameter yokes and samples mitigate the field intensity z-component above the sample thereby allowing a large measurement area.

To allow enough space for sample placement without significantly increasing the MMF required to magnetize the sample, two sample diameters were investigated, 136 and 134 mm. These correspond to 2 mm and 3 mm air gap between the sample and the core inner diameter.

The design choice is based on the magnetizer design in [28] which showed that a sinusoidally wound induction machine stator is capable of producing a uniform field in the sample. For the selected sample and yoke diameters, 24 slot, 36 slot and 48 slot designs with windings as shown in Figure 4-4 were investigated in 3D. 2D simulations were insufficient as they would imply the same sample and yoke depth, which is not the case. A higher number of slots for the same dimensions would be more complicated to model and manufacture.

The two phase coils are modeled as solids in each slot with a unique number of turns sinusoidally distributed in each slot as shown in Figure 4-4 for one phase, the other phase is 90° phase shifted. All winding patterns are limited to a maximum 8 coils per slot, this ensures similar slot loading. Figure 4-5 (a) shows the 3D models of the magnetizer corresponding to the presented windings. The effect of the end windings is included by modeling the coils longer than the core. A peak current of 10 A is used to excite the cores and the resulting flux density distribution in the sample is as shown in Figure 4-5(b).

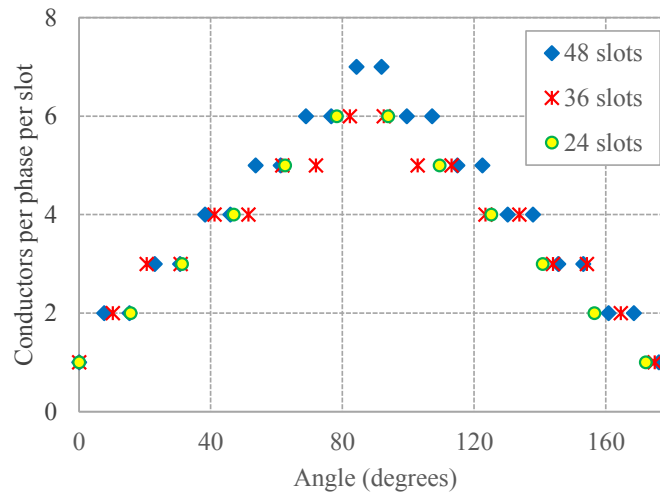


Figure 4-4: .Winding pattern for the different number of slots designs

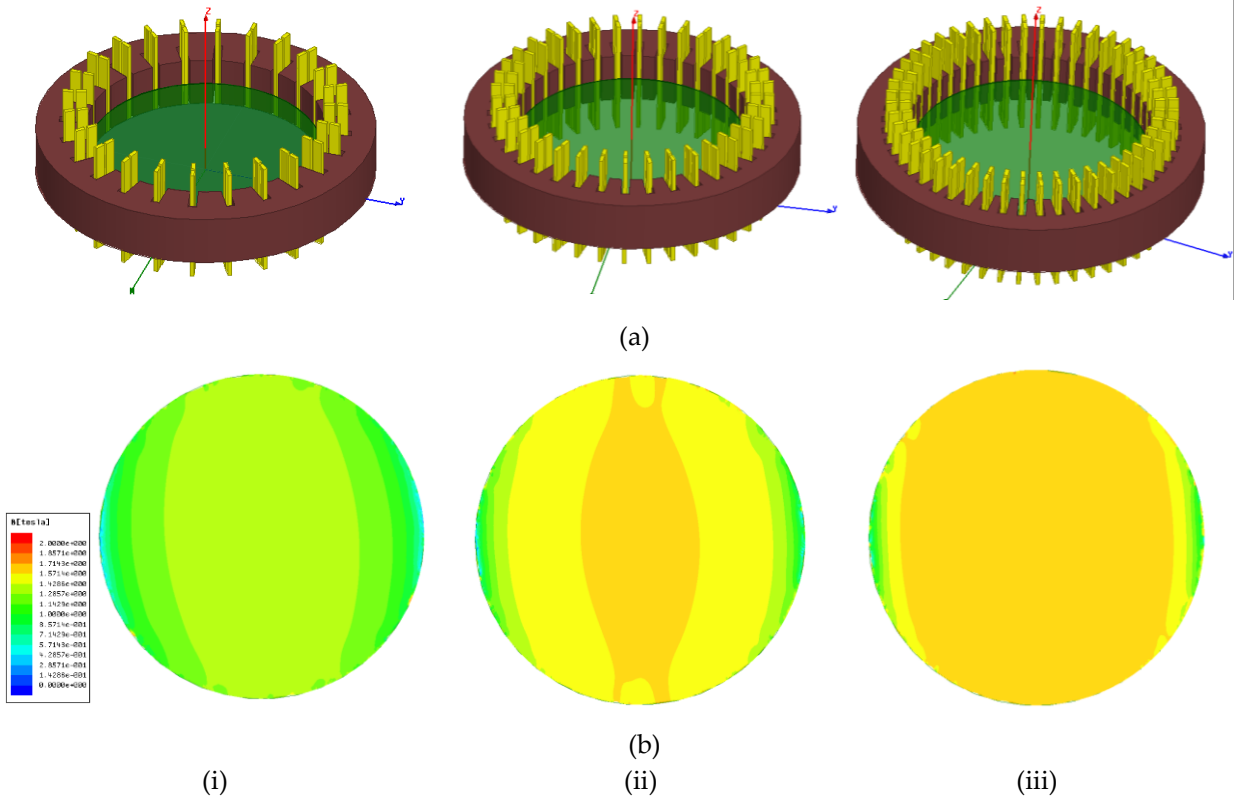


Figure 4-5: The different magnetizer slot number (a) 3D models, and (b) Flux density distribution in sample, for i) 24 slots, ii) 36 slots, iii) 48 slots

Results indicate that the 48 slot winding offers a large uniform area compared to the other winding and slot combinations. Moreover, for the same current in all windings, the 48 slot model provides a higher flux density in the sample. Therefore, the 48 slot model was selected for further modification. In all the modeled cases, the flux density distribution in the sample does not vary with the rotating vector but only rotates with it. This is a benefit of a sinusoidally wound winding.

4.1.2.1 Modification of the 48 slot magnetizer

The selected 48 slot magnetizer model is modified to ensure the maximum possible measurement area. Measurement area here is defined as the area over which the flux density and field intensity distribution is the same or within a few percentage differences for all flux density level and flux rotations. Magnetizer design considerations are given to the yoke depth, winding pattern and sample diameter, which result in maximum measurement area.

For comparison purposes all the flux density distributions across the sample diameter are obtained in the middle of the sample, while the field intensity distributions are obtained 1 mm above the sample. This gives the actual representation of where the respective field quantities will be measured in the real set up using the available coil sensors. In the real set up, the **B**-coils are wound around the sample while the **H**-coils are placed on top of the sample.

To maximize the flux density in the sample, the number of coils per slot was increased to ten based on the coil sizing presented in the appendix. For a maximum of 10 coils per slot, two possible winding patterns were considered. Figure 4-6 shows a section of the two winding patterns for one phase. The same magnetizer dimensions are used to simulate the two windings for comparison purposes. Winding1 has a maximum of seven coils compared to winding2 with a maximum of six coils.

Figure 4-7 shows a comparison of the flux density and field intensity across the sample with the design variations. 'Design' indicates the magnetizer with 30 mm yoke depth, sample diameter of 136 mm, and winding2. 'Sample – 134 mm' indicates a sample with a diameter of 134 mm and yoke depth of 30 mm using winding2. 'Winding1' shows the same yoke dimensions, sample diameter of 136 mm using winding1, and yoke depth 60 mm and 20 mm corresponds to their respective yoke depths for 136 mm sample diameter with winding2.

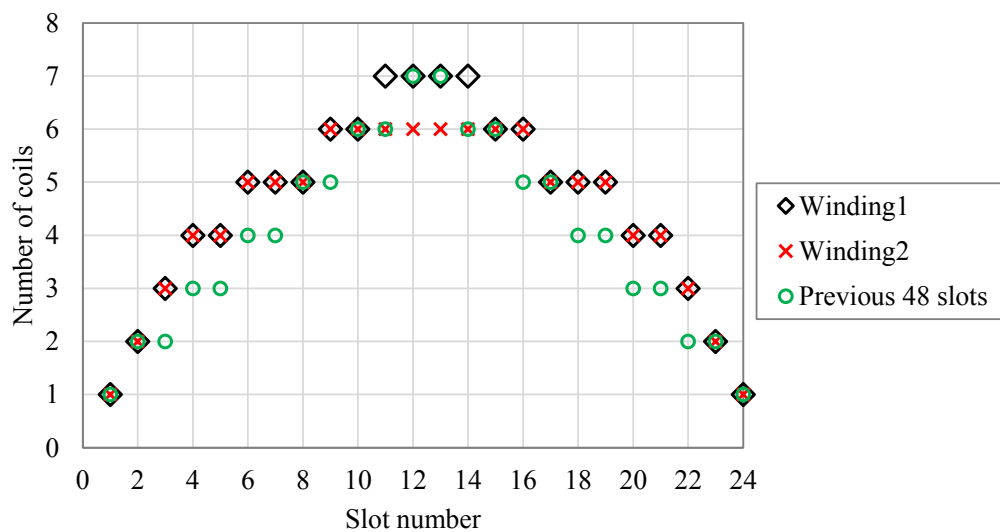


Figure 4-6: Winding patterns

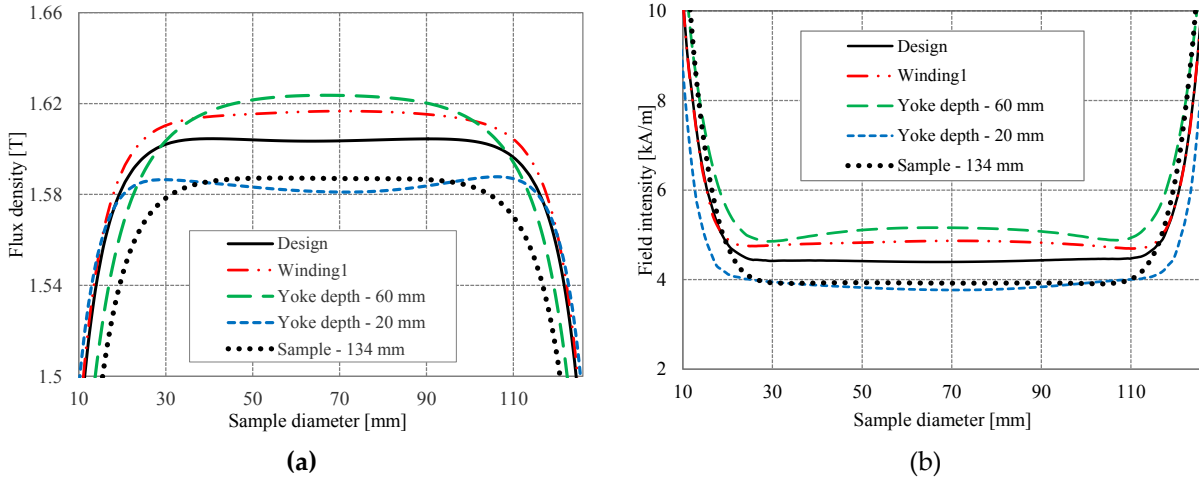


Figure 4-7: (a) Flux density distribution in the sample x-axis with the flux vector in the positive X direction for different design modifications at 10 A

The flux density and field intensity distribution across the sample is the worst case, when both the flux vector and line across the sample diameter is on the x axis. For the same flux vector direction, the flux density across the sample in other directions is more uniform.

A comparison of all the cases shows that the flux density distribution across the sample in the 'Design' case is more uniform over a wider sample diameter. This is indicated by the flat line between 50 and 90 mm along the sample diameter. The sample with 134 mm also shows the same uniformity however would require a higher current to achieve the same flux density level because of the increased air gap reluctance.

The sample flux density increased with the yoke depth. Results showed that with a 20 mm depth, the flux is less in the center, while with a 60 mm depth the center is much higher. A 40 mm yoke depth was also simulated (results not shown) showed a much smaller measurement area compared to the 30 mm yoke depth. Additionally the 40 mm showed a very large field intensity variation at low flux densities.

Winding1 showed a higher flux density as expected because of the increased MMF with the extra turns. However, this higher flux did not necessarily correspond to a large measurement area as in 'Design'. Winding2 is therefore the preferred winding.

The above results are also consistent when the field intensity distribution across the sample. Therefore, the 'Design' case was chosen as the final design of the magnetizer. Table 4-1

shows the possible measurement areas on the sample at low flux density of 0.56 T and high flux density of 1.6 T. This is indicated by the percentage difference between the value in the middle of the sample and the values at their respective distances from the center.

The flux density distribution across the sample diameter at both flux levels is uniform as shown by the small percentage difference. The field intensity 1 mm above the sample surface however shows a higher percentage at lower flux densities especially for the larger measurement area of 65 by 65 mm. As a result, in the prototyped magnetizer, the B-coils are threaded through holes with a measurement area of 65 by 65 mm and the H-coil dimensions are 53 by 53 mm, which ensures that the measurements at both low and high flux densities are within an error of 5%.

Table 4-1 Measurement area on the sample

Area (mm)	B				H			
	0.5634 T		1.6035 T		0.379029 kA/m		4.408308 kA/m	
20 by 20	58 mm	78 mm	58 mm	78 mm	58 mm	78 mm	58 mm	78 mm
	0.1%	0.0%	0.0%	0.0%	0.5%	0.5%	0.4%	0.1%
40 by 40	48 mm	88 mm	48 mm	88 mm	48 mm	88 mm	48 mm	88 mm
	0.2%	0.0%	0.0%	0.1%	2.9%	3.0%	0.9%	0.7%
60 by 60	38 mm	98 mm	38 mm	98 mm	38 mm	98 mm	38 mm	98 mm
	0.1%	-0.1%	0.1%	0.0%	14.7%	14.7%	1.3%	1.6%
65 by 65	35.5 mm	100.5 mm	35.5 mm	100.5 mm	35.5 mm	100.5 mm	35.5 mm	100.5 mm
	0.0%	-0.3%	0.0%	0.0%	21.6%	22.1%	1.2%	1.8%

4.1.2.2 Final magnetizer parameters

Figure 4-8 shows the 3D model of the final magnetizer design. The two phase coils are modeled as solids in each slot with a unique number of turns in each phase coil per phase as shown in Figure 4-9. The numbers in red indicate the number of turns in each slot, indicated with the black numbers. The arrows indicate the direction of current flow in each coil. In the FEA model, each coil is modeled longer than the core to include the end winding effect of the flux density

distribution in the magnetizer core and sample as previously done.

Simulation results of the flux density distribution at 10 A is shown in Figure 4-10 and Figure 4-11 at two different flux vector orientations. The flux density distribution in the sample is uniform for the new magnetizer in all flux vector rotation directions. Moreover, for a sample flux density of 1.6 T, the yoke maximum flux is about 0.4 T, which implies that the material will saturate much faster than the yoke and therefore the yoke non-linear effects will not be included in the measured sample fields.

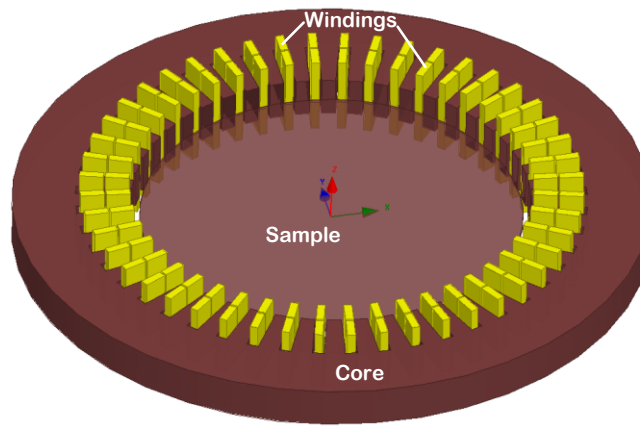


Figure 4-8: 3D model of the new magnetizer design.

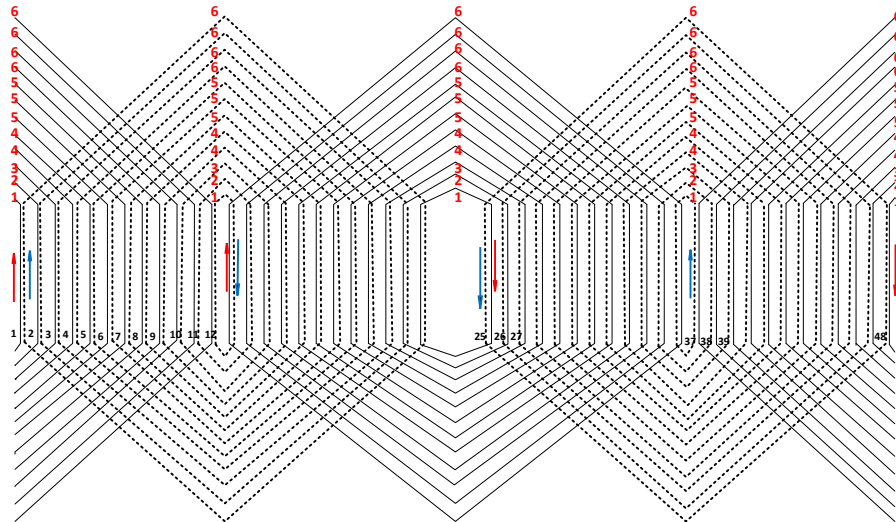


Figure 4-9: Sinusoidal winding diagram showing the number of coils per turn in each slot

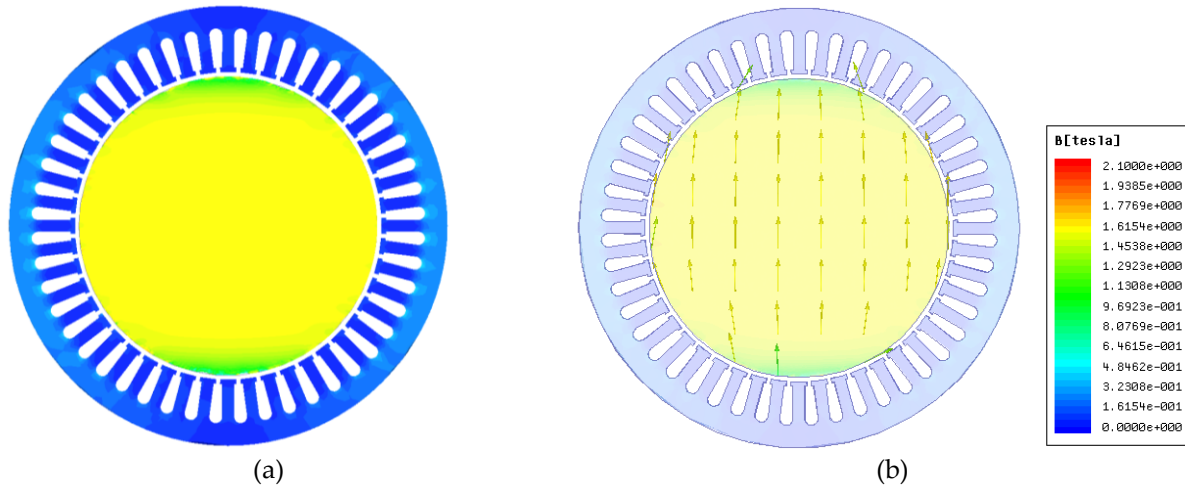


Figure 4-10: Field distribution at 10 A with the flux vector in the y, (a) Flux density distribution, (b) Flux vector in the sample.

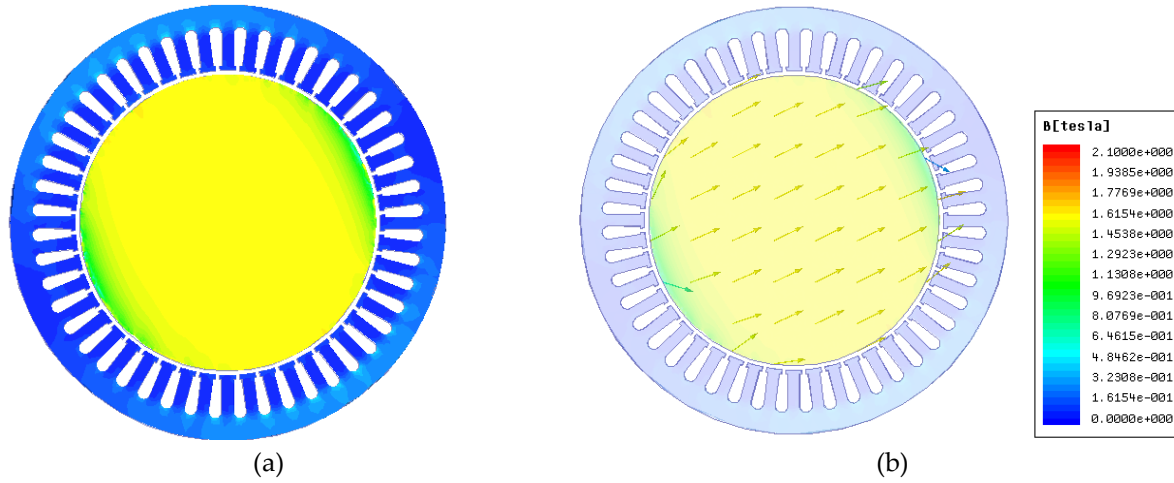


Figure 4-11: Field distribution at 10 A with the flux vector at 45° from the y, (a) Flux density distribution, (b) Flux vector in the sample.

A uniform flux density distribution in all the flux vector directions indicates a wide area over which the coil sensors can be placed. A wide measurement area is synonymous with a larger number of sensor turns and therefore better sensitivity of the sensor. The magnetizer achieves a large measurement area of 65 by 65 mm.

4.1.3 Comparison of the testers

Similar simulation parameters are used to compare both testers such as; a fine sample mesh, non-linear transient solver with 0.166 ms time step, the same material is assigned to both yokes and samples, and comparisons are made for the same flux density level in the sample. Table 4-2 below shows a summary of the dimensions of the two rotational flux magnetizers.

Table 4-2 Comparison of the testers

	Previous Design	New Design
Sample diameter (mm)	58	136
Yoke depth (mm)	5	30
Winding	Concentrated Semi distributed	Sinusoidally wound
Air gap length (mm)	1	2
Measurement area		65 by 65 mm

A comparison of the flux density distribution in the sample for both testers at different magnetization directions (indicated by the black arrow) is shown in Figure 4-12 for the same excitation current. However, to have the same flux density level in the sample for comparison purposes, a 5 A current is used in the previous tester and by virtue of its size, 10 A is used in the new magnetizer. The 8 pole yoke magnetizer still showed the same distribution of flux density as with the 10 A current except for the lower flux density magnitudes.

The results of the previous tester showed that at each magnetization direction, the flux density distribution in the sample changes, while the new tester exhibits consistency in the flux distribution across the sample diameter for all magnetization directions. This change in

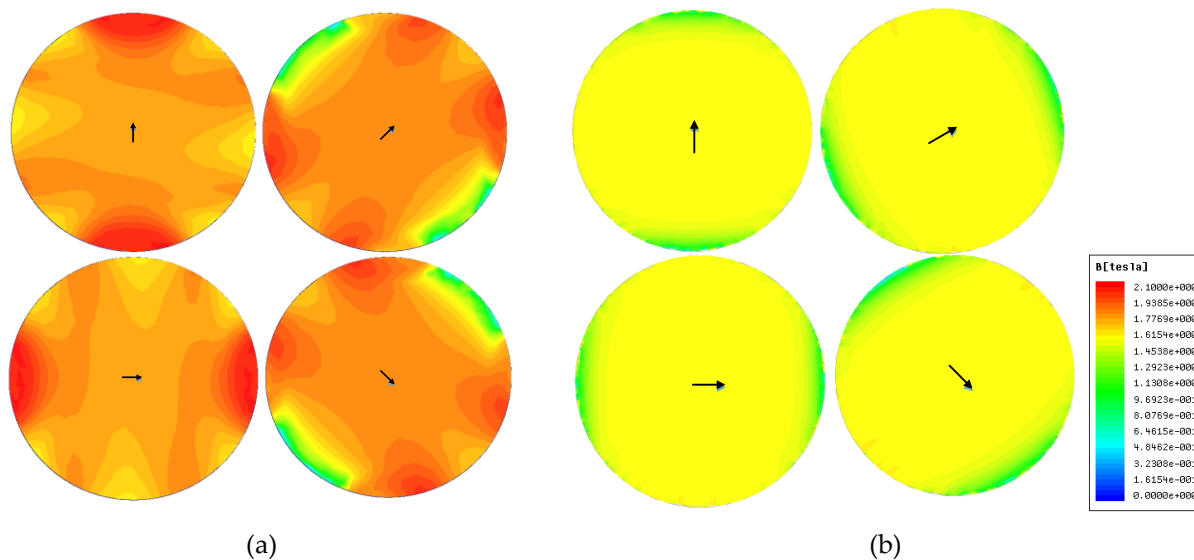


Figure 4-12: Flux density distribution in the sample; a) previous magnetizer, b) New magnetizer

distribution as the flux vector rotates limits the area over which the flux density is constant therefore significantly reducing the measurement area, and the limiting the **B** and **H** coil dimensions.

Smaller **B** and **H** coil dimensions limit the number of coils in the sensor, reducing their sensitivity. Moreover, a smaller measurement area averages the material properties over a small area which may not be an accurate representation of the material properties.

4.2 Core loss measurements

The final magnetizer design was prototyped and the measurement test bench set up as shown in Figure 4-13. Signals are generated in LabVIEW and via the NI USB-6356, they are converted from digital signals to analog signals, which are amplified to power signals to excite the core. Digital multimeters are used to monitor the excitation current in each phase to ensure the limit of 10 A is not exceeded. The measured phase voltages, **H** and **B** coil voltages are acquired simultaneously with the DAQ card.

The acquired coil voltages are post processed to calculate the rotational core losses. This is done by averaging the acquired 3 cycles over 100 iterations, this eliminates any errors from the acquisition. Additionally, over 7000 points are acquired per cycle for 60 Hz measurements to increase the post processing accuracy. At higher frequencies the sampling time is appropriately reduced. Details on using the LabVIEW program VI (front and back panel), procedure for core measurement and specifications of the setup components are presented in the appendix.

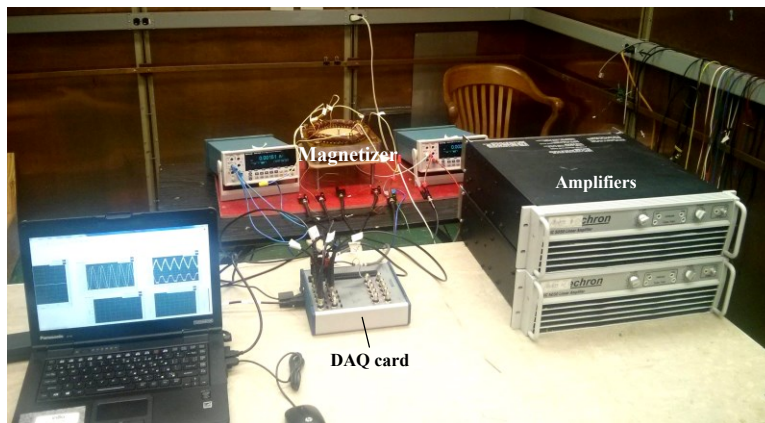


Figure 4-13: Core loss measurement setup

4.2.1 Pulsating core loss measurements

The material sample is anisotropic, therefore the **BH** loops in the rolling direction (X direction) and the transverse direction (Y direction) are different as shown in Figure 4-14 (a). This implies that the measured pulsating core losses should be representative of the material properties in both directions.

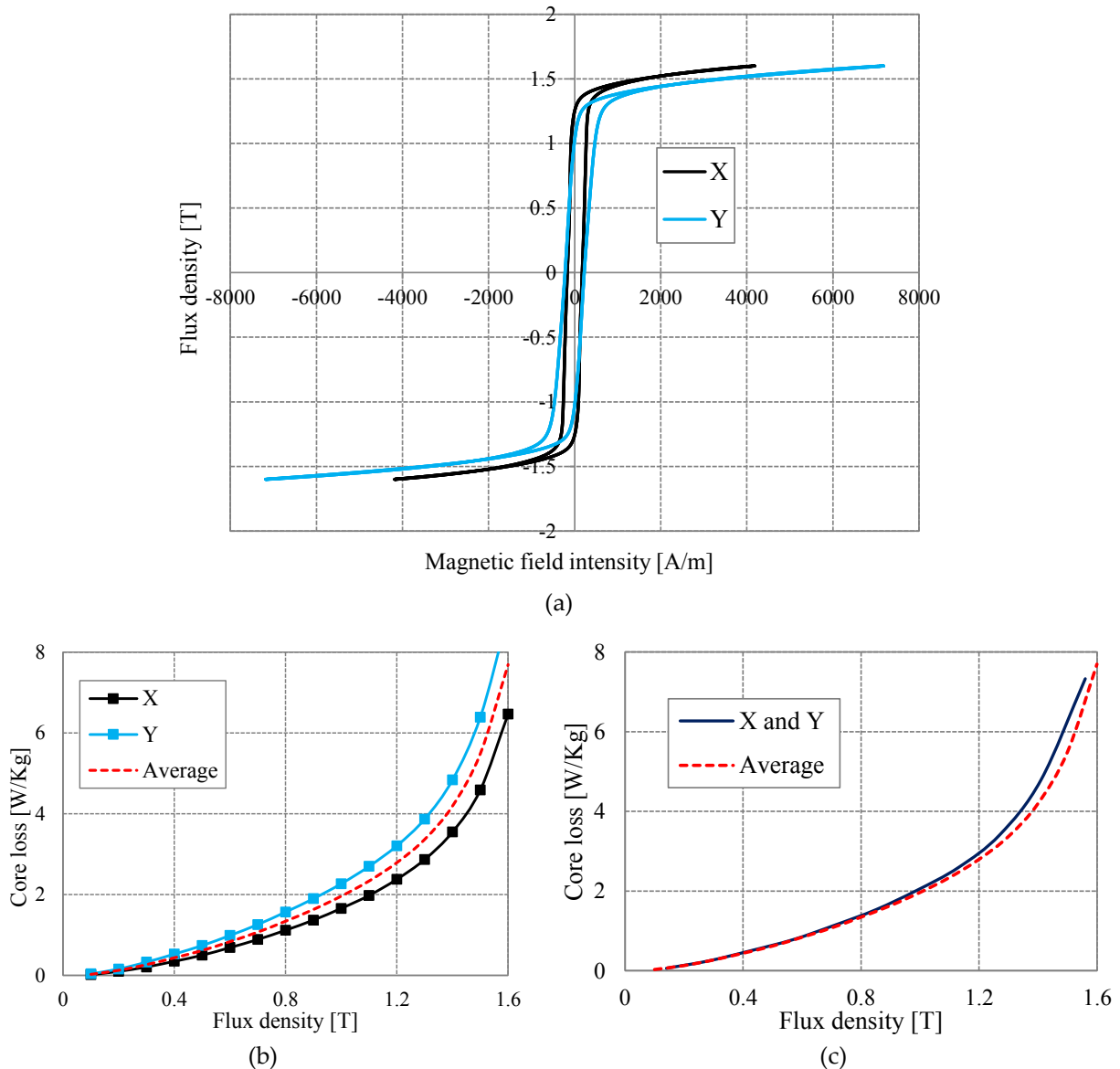


Figure 4-14: Pulsating core loss measurements at 60 Hz, (a) Measured **BH** loops of the X and Y, (b) Measured losses when x and y are excited independently and their average is the total core loss, (c) Measured losses when x and y are excited simultaneously, and the result is compared to the average from (b).

Pulsating core losses were hence measured using two different approaches; exciting the phases independently and averaging the results, and exciting the phases simultaneously with $R = 0$. When the phases are excited separately, the total loss is considered an average of the two separate losses as in Figure 4-14 (b). When both phases are excited simultaneously with $R = 0$, the result is indicated as X and Y in Figure 4-14 (c). Comparison of the two approaches showed that the results agree until around 1.2 T, after which the loss with both phases excited becomes higher than the average. For all the pulsating loss measurements considered in this section, the first method was used.

Figure 4-15 shows the measured sample **BH** loops at different flux densities when the x is separately excited. As expected the larger loops fully enclose the smaller loops, which shows consistency especially at coercivity. Measurements at other frequencies, 200 Hz and 400 Hz are also shown in Figure 4-16. As the frequency increases for the same level of flux density, the eddy current losses increase, which causes the **BH** loop to expand as shown in Figure 4-16 (a), where all the loops are measured at 1 T. Figure 4-16 shows the corresponding core losses at different flux densities for the different frequencies.

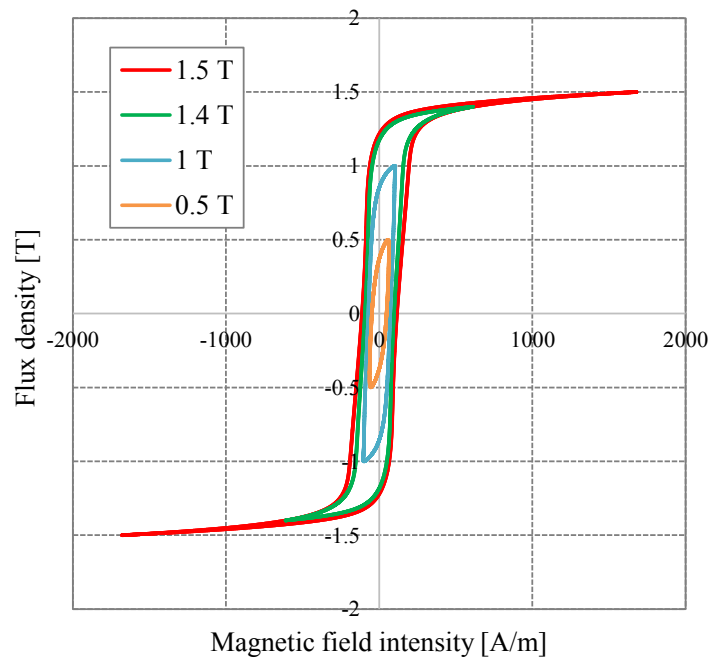


Figure 4-15: Measured BH loops at different flux density levels

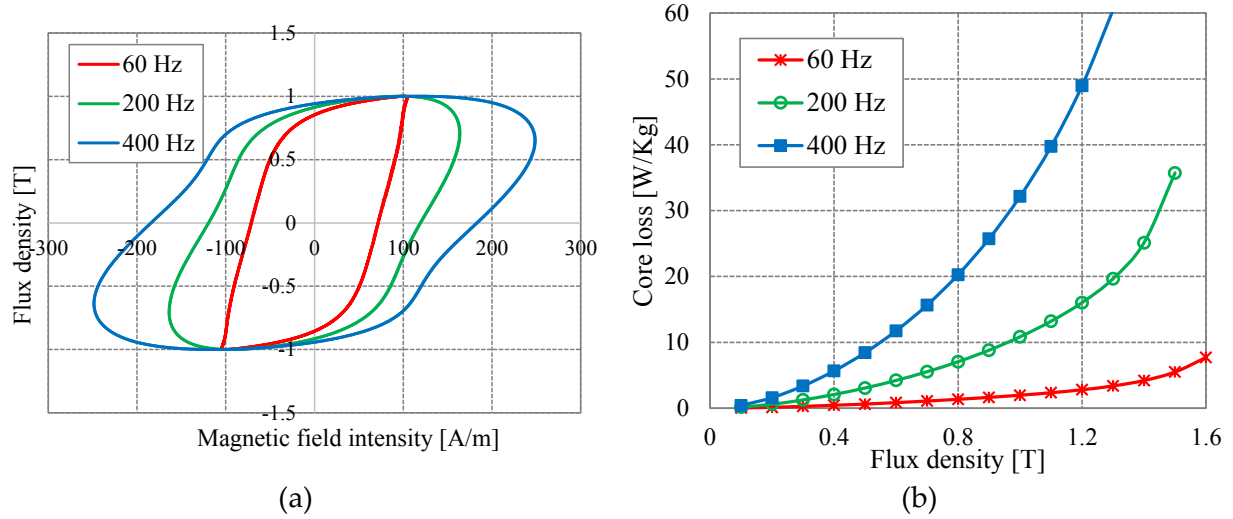


Figure 4-16: (a) Measured **BH** loops at 1 T for different frequencies, (b) Measured core losses at different frequencies

4.2.2 Rotational core loss measurements

Rotational core losses are measured by exciting both phases simultaneously with the exciting voltages 90° phase shifted from each other. For measurements at different aspect ratios R , the phase shift between the angles is varied as shown in Table 4-3. In all the cases, the flux density magnitudes (B_x and B_y) are kept the same. Losses are measured in the clockwise and counterclockwise directions, and the total losses obtained as an average of the losses from both directions. This eliminates any effects from sensor misalignment.

Figure 4-17 shows rotational core loss measurement results at 60 Hz, in the clockwise and counter clockwise directions, and measurements for different aspect ratios. The measurements show that as the aspect ratio increases for the same flux density, the associated losses also increase. At around 1.5 T, the losses seem to converge and the $R=1$ losses begin to decrease.

Table 4-3 Angles for different aspect ratios

R	0	0.2	0.4	0.6	0.8	1
Angle ($^\circ$)	0	22.6	43.5	61.95	77.3	90

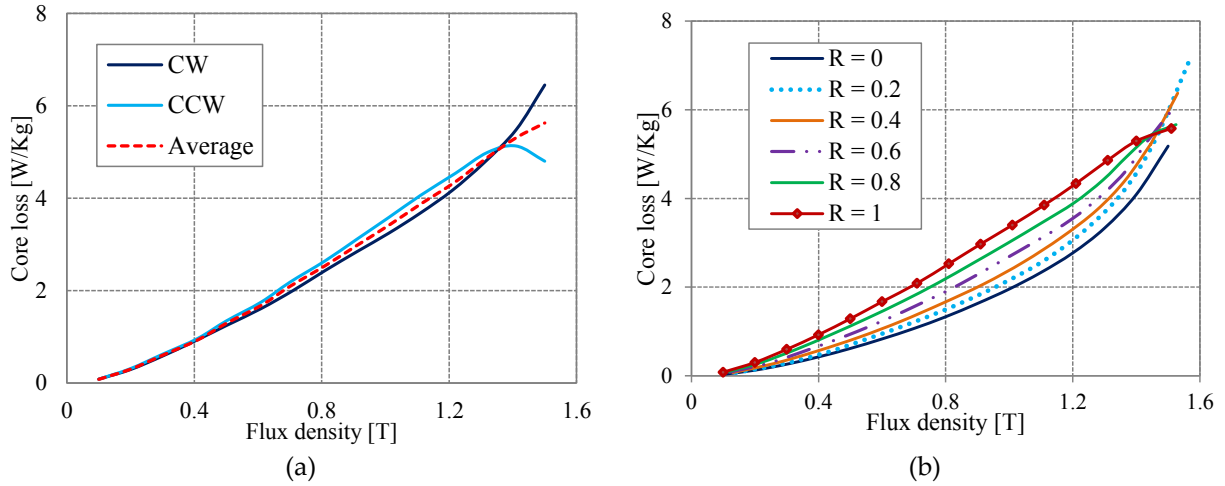


Figure 4-17: Measured rotational core losses at 60 Hz for; (a) Aspect ratio $R = 1$ in the clockwise and counter clockwise direction, (b) Different aspect ratios.

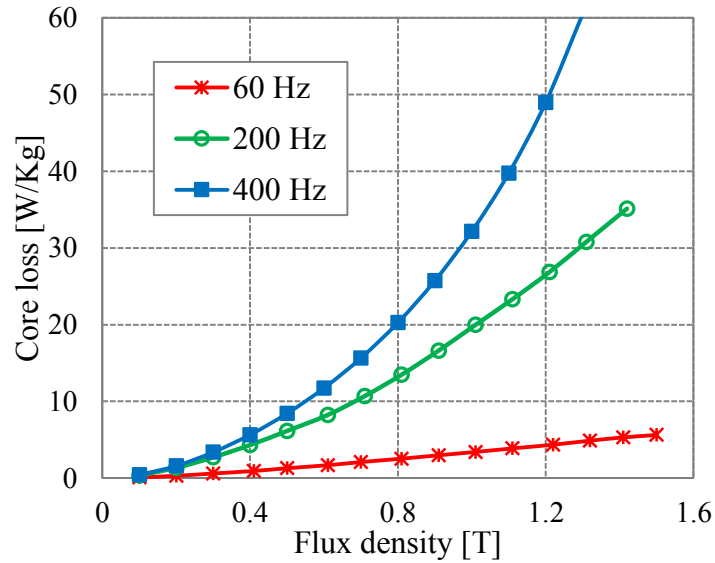


Figure 4-18: Measured core losses at different frequencies

Measurements at 200 and 400 Hz were also performed as shown in Figure 4-18, the trend obtained is similar to that of the pulsating losses previously shown. Core loss measurements at higher frequencies however require a lower sampling time compared to measurements at lower frequencies. Low frequency measurements are important for loss separation, while high frequency measurements are important for inclusion of harmonics in core loss calculation.

In the next section, measurements at a low frequency of 10 Hz were performed to enable loss separation. Core loss measurements at frequencies less than 10 Hz were difficult as the captured waveforms were very unstable.

4.3 Loss separation

Loss separation is when the measured core losses are separated into their loss components, hysteresis loss and eddy current losses. The eddy current losses are frequency dependent losses, therefore at core loss measurements with DC excitation is equivalent to hysteresis losses. However, the fieldmetric method of core loss measurement used is dependent on the induced sensor voltages based on Farady's law, which requires a change in the magnetic field ie frequency. Thus, to use this method for loss separation, measurements at the lowest frequency possible can be considered hysteresis losses as eddy currents at that frequency are negligible.

Rotational core losses were measured at 10 Hz, the lowest frequency possible. Attempts to measure core losses at frequencies less than 10 Hz were futile as the captured waveforms were very unstable. Figure 4-19 shows the loss separation, where the loss at 10 Hz represents the hysteresis loss and the difference between the losses at 60 Hz and 10 Hz represents the eddy current losses at 60 Hz.

The Steinmetz equation (4.1) in [30], which separates the losses into the hysteresis and eddy current component only was used for loss separation

$$P_c = K_h B^\alpha f + K_e B^2 f^2 \quad 4.1$$

where K_h is the hysteresis coefficient, B is the flux density, α is the Steinmetz coefficient, K_e is the eddy current loss, and f is the frequency. The hysteresis losses per cycle at 10 Hz were curve fitted

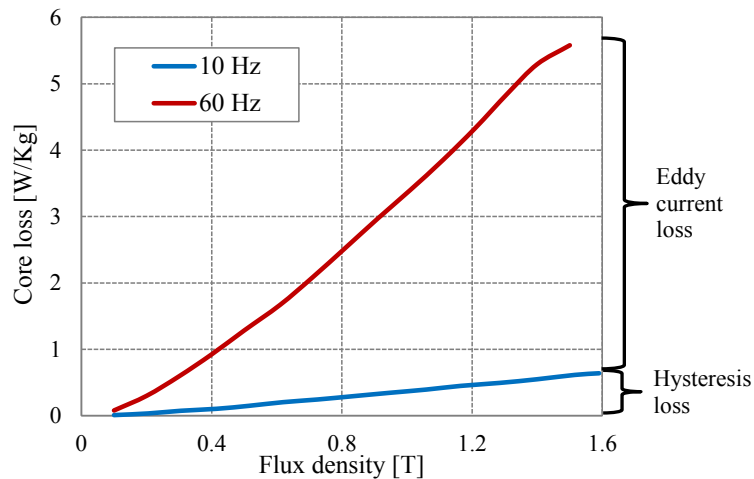


Figure 4-19: Measured rotational core losses at 10 Hz and 60 Hz

to obtain the K_h and α assuming constant coefficients. These coefficients as shown in [93] are flux density and frequency dependent, therefore this is a simplification of the coefficient values.

Figure 4-20 (a) shows that the assumption of constant coefficient is sufficient since the measured and predicted losses are in good agreement. Using the determined coefficients shown in Table 4-4, the hysteresis losses at 60 Hz were determined and subtracted from the measured core losses at 60 Hz. Figure 4-20 (b) shows the loss separation at 60 Hz. This approach can be used to determine the loss separation at any frequency provided the measured results at that frequency are available.

Loss separation can also be used as a technic to predict core losses in the electrical machine under ideal conditions such as sinusoidal flux densities. However, for any prediction, low frequency measurements are required which can be a challenge to obtain especially because the rotational core loss measurement is still a manual process, therefore measurements at several frequencies is cumbersome. In the next chapter other ways to estimate core losses in the machine are presented that only require measurements at the operating frequency of the machine. Moreover, consideration is given to the non-sinusoidal flux in the actual machine.

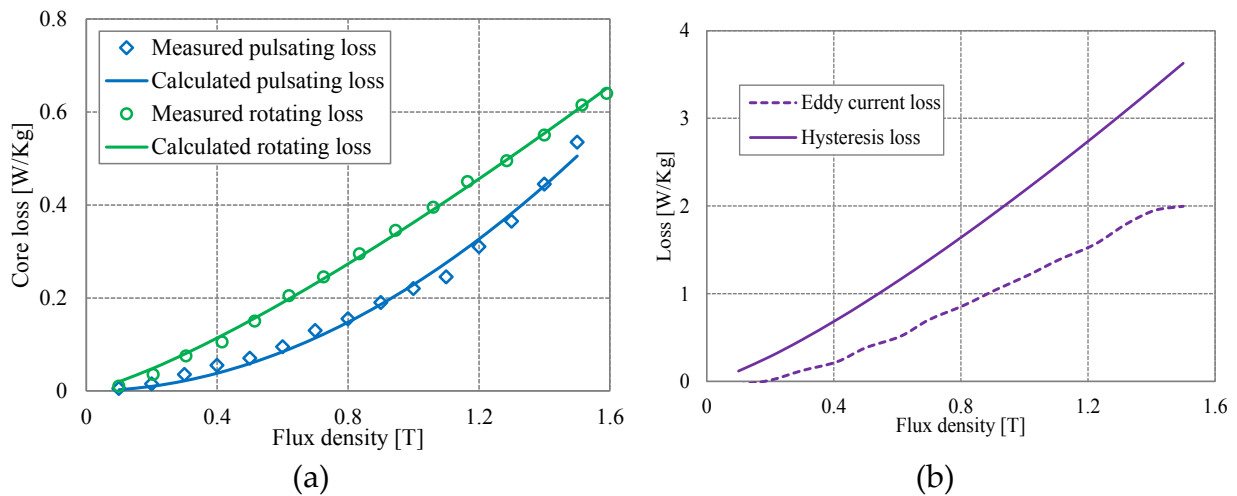


Figure 4-20: (a) Measured and predicted losses at 10 Hz, (b) Loss separation at 60 Hz

Table 4-4 Coefficients for hysteresis loss calculation

Coefficient	Pulsating loss	Rotating loss
K_h	0.02288	0.03624
α	1.954	1.263

4.4 Inter lamination faults

Shorting between laminations in hydro generator cores occurs in the stator yoke and at the edges of the stator teeth. Rotational flux which covers over 60% of the stator as was shown in chapter 3, also occurs in the stator yoke, and is a potential source of localized heating from the associated core losses. The presence of lamination faults can further accelerate the localized core overheating.

In literature, work has been done on the detection of lamination faults by only considering pulsating flux, this work therefore focusses on lamination faults in a rotating field. This was done by FEA modeling and simulation of lamination faults on a rotational core loss test bench. The main aim of this work was to provide an understanding of the flux distribution in the core, in the presence of a fault. One of the modeled faults was implemented in the samples and the associated losses measured at different frequencies.

4.4.1 FEA model preparation

The single sheet rotational test rig in [29] was designed to measure rotational core losses in a single 200 mm diameter sample using the field metric method. The magnetizing field in this setup is provided by two sets of orthogonal windings in each pole arranged in the Halbach array. Two sets of **B**-coils are wrapped around the sample in the x and y directions, and **H**-coils are placed above and below the sample in a 50 by 50 mm measurement area at the center of the sample. The measurement of the field quantities averages the material effects with in this 50 by 50 mm sample measurement area.

A 3D model of the test rig is shown in Figure 4-21 with two samples of 0.3556 mm thickness each and a spacing of 0.05 mm between them, to account for surface insulation on the samples. Non-oriented M15G29 magnetic steel was used for both the poles and the samples, and was considered isotropic in this 3D simulation i.e. having the same permeability, magnetic coercivity, conductivity and permittivity in all three axes. It is possible to consider an anisotropic material with separately defined tensors relative to the coordinate system. However this requires material property data in all the axes currently unavailable.

The poles were modeled as a solid object with a stacking factor of 0.96 in the Z-direction, while the sample laminations were individually modeled. This simplifies the model from using separate lamination layers for the 20 mm pole depth, which is not only challenging to draw but would also have a very dense mesh that requires a lot of memory and processing capabilities. Moreover, it also reduces the memory requirement, mesh and required simulation time.

X and Y phase windings were modeled as copper bars with a height longer than the poles to include the height of the end windings. Each bar was assigned a current direction with the same number of conductors to model the turns per pole in the setup. This also further reduces the simulation time compared to when the end windings and individual number of turns are considered. The winding impedance is added in the external circuit.

In simulation, current type windings are considered and therefore 60 Hz sinusoidal currents are directly assigned to the windings. A fine mesh of 2 mm for the samples was sufficient

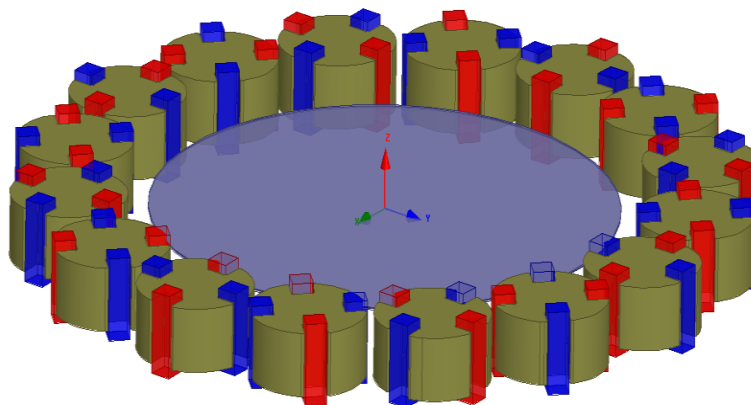


Figure 4-21: 3D model of the test rig with two laminations, the red shows the y coils and the blue the x coils

for both computation and simulation time. Eddy current effects were also enabled in the samples to include their effects in the flux distribution in the material. A nonlinear transient solver with a time step of $5.2\text{e-}4$ s was selected for the simulations for one 60 Hz cycle.

The setup was designed for one lamination, therefore another lamination causes the samples to be unsymmetrically centered along the pole depth. Simulations were therefore performed to ensure uniform flux density distribution in both samples prior to the fault analysis. Flux density along lines on the x and y axes in the middle of each sample, were used for the comparison.

Figure 4-22 shows a comparison of flux density distribution in the lower sample when one or two samples are used in the setup for the same magnetizing current. The profile shows that the flux density distribution along the sample diameter in the x and y directions is the same, only the magnitude of the flux density is different. The magnitude of the flux density with two samples reduces by 0.4% from that of one sample for the same magnetizing current, therefore an additional sample requires more magnetizing current to achieve the same flux density level compared to when one sample is used.

A comparison of the flux density distribution in both the upper and lower samples was also done to ensure uniformity of the flux density and field intensity in both samples. Simulation results in Figure 4-23 showed that the addition of another lamination does not affect the flux density uniformity in both samples. Both samples had the same magnitude and distribution of

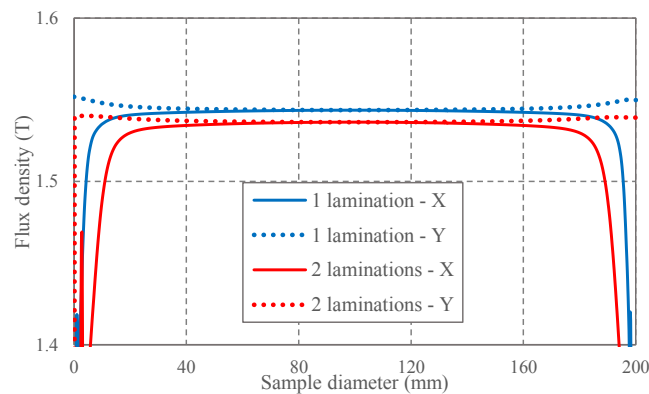


Figure 4-22: Comparison of flux density distribution across the lower sample in the x and y directions when one or two samples are used in the setup

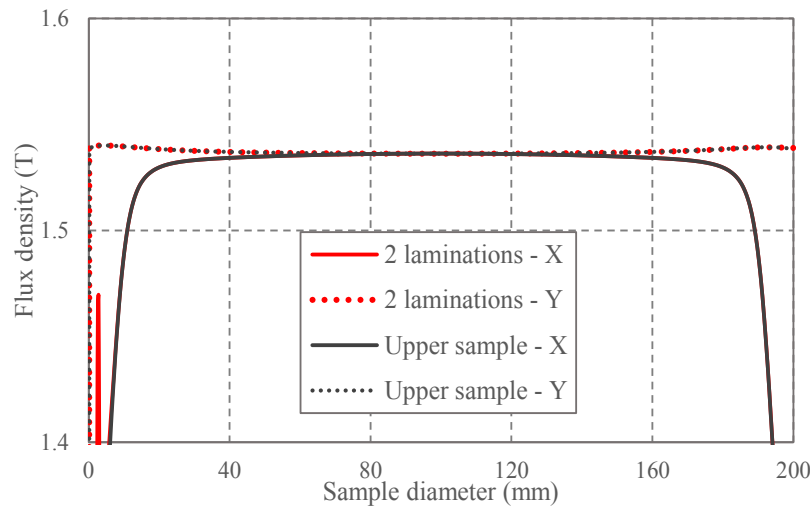


Figure 4-23: Comparison of the flux density distribution across the sample in the x and y direction on the lower and upper samples

flux density with no effect of the Z-offset on the second sample. Comparison of \mathbf{H} above and below both samples also showed no effect of sample stacking.

4.4.2 Simulation of the fault

Localized faults were modeled by creating contact between the two lamination samples, in the location of the fault. In a physical system, the contact resistance between the laminations is a function of the area of contact. This contact resistance was not included in the FEA simulations because at the point of fault there is continuity between the laminations. The fault therefore assumes the same resistance as the sample, which negates the need to define contact resistance.

Different positions and sizes of faults as shown in Figure 4-24 were modeled and simulated. A 20 mm diameter fault, Fault A, was realized on the x and y axes, 30 mm from the middle of the sample on the x axis and 70 mm from the middle of the sample on the y axis. This simulates the effect of fault position either near or further from the center of the sample. Fault B of 40 mm diameter shows the effect of having the fault away from the measurement axes, in addition to considering an increase in the fault size, while Fault C of 140 mm diameter shows the effect of the size of the fault.

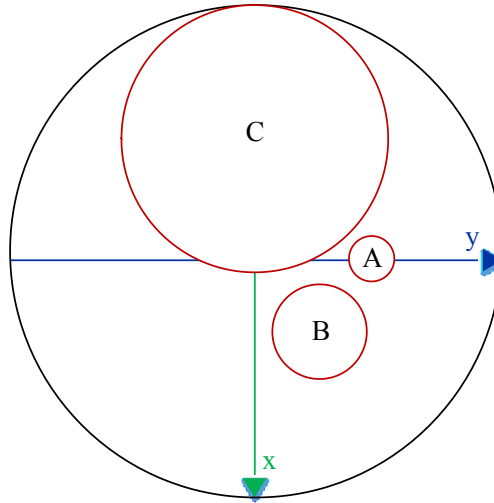


Figure 4-24: Sample with location and size of different faults; Fault A is 20 mm in diameter; Fault B is 40 mm in diameter and Fault C is 140 mm in diameter

Figure 4-25 shows the flux density distribution in the samples when the flux vector is aligned with the x and y axes for the different fault locations and sizes, using the same magnetizing current. The top figures, (i) are when the vector is aligned with the x axis, and the bottom figures, (ii) are when the vector is aligned with the y axis. Figure 4-25 (a) has no fault and shows the flux density distribution across the sample under normal operation. It indicates that the flux density is mostly uniform across the sample except at the sample edges, which have lower flux density. This is due to the design of the setup. Figure 4-25 (b) and (c) show Fault A in two locations and Fault C respectively.

The presence of a fault causes non-uniform flux density distribution within and around the fault area. As the flux vector rotates, these regions of non-uniformity also rotate hence affecting the sample area in and around the fault. The size of the sample area affected by the fault is also dependent on the magnetization direction and the presence of an adjacent fault as in Figure 4-25 (b). This can be attributed to the fact that as the magnetization vector rotates, the flux density distribution around the fault also rotates, and an interaction between two adjacent faults causes a redistribution of the flux within the sample. A large fault as in Figure 4-25 (c) shows the flux density distortion with one side of the fault having a higher flux density and the other having a lower flux density.

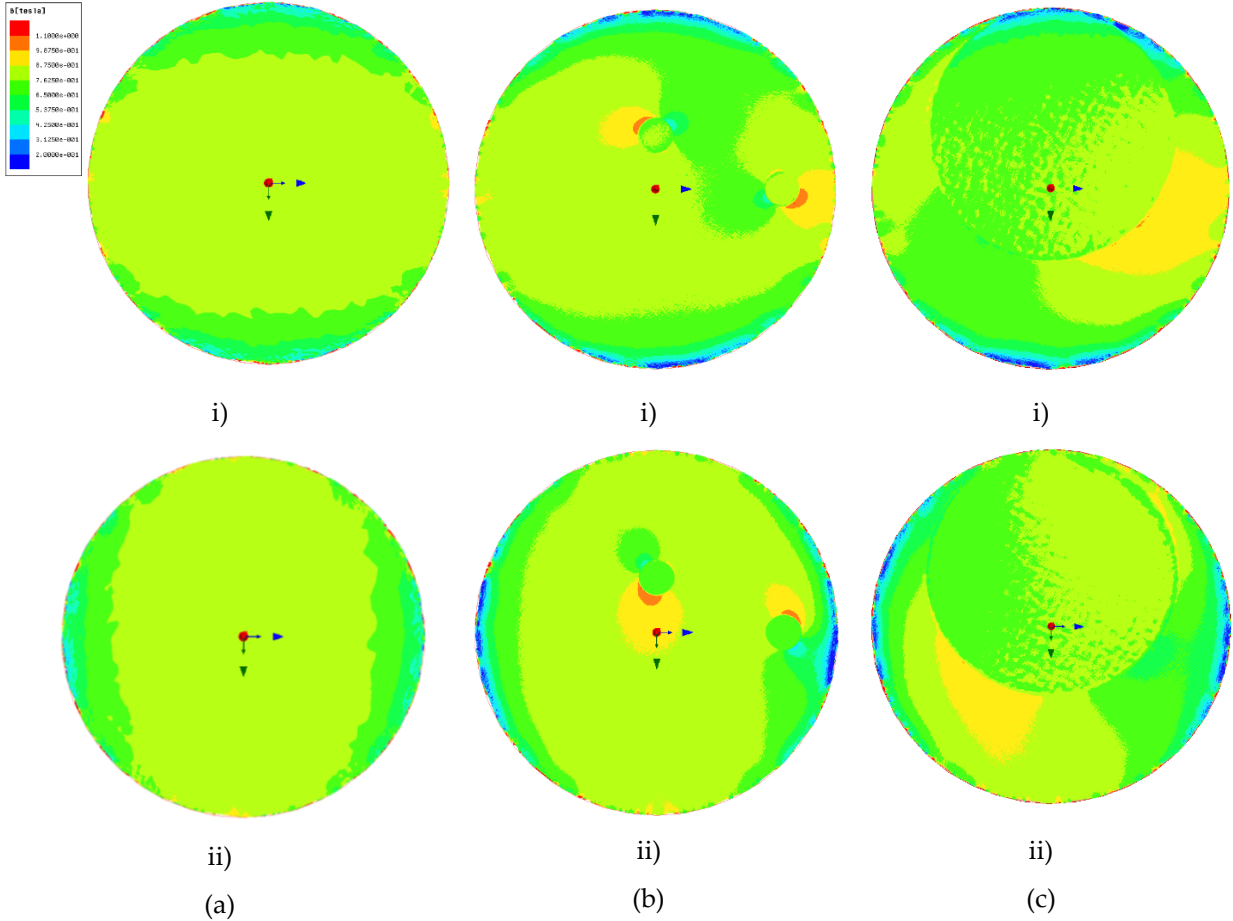


Figure 4-25: Flux density distribution in the sample with the flux vector i) aligned to the - X axis and ii) aligned to the Y axis, for; a) No fault in the sample, b) With fault A on the X and Y axis 30 and 40mm from the center of the sample, c) With fault aligned to the X axis

The magnitude of flux density and field intensity across the sample, for all fault cases was compared using the extracted quantities in the middle and above the sample respectively. Figure 4-26 shows the flux density magnitude across the sample diameter in both the x and y axes, at the time instant when the magnetizing vector is in the x direction. The no fault condition indicated by a blue line in Figure 4-26 provides a reference for all the other cases. Each of the faults show unique signatures in the localized flux density plots, which is generally indicated by a lower flux density in the position of the fault.

Fault B, which is not aligned with any axis also shows a distortion in the flux density magnitude across the sample, indicating that the fault also alters the flux density distribution in the area around it. The observed level of flux distortion is dependent on the size and location of the fault with respect to the axes where the flux is measured. For instance Fault A on the x axis in

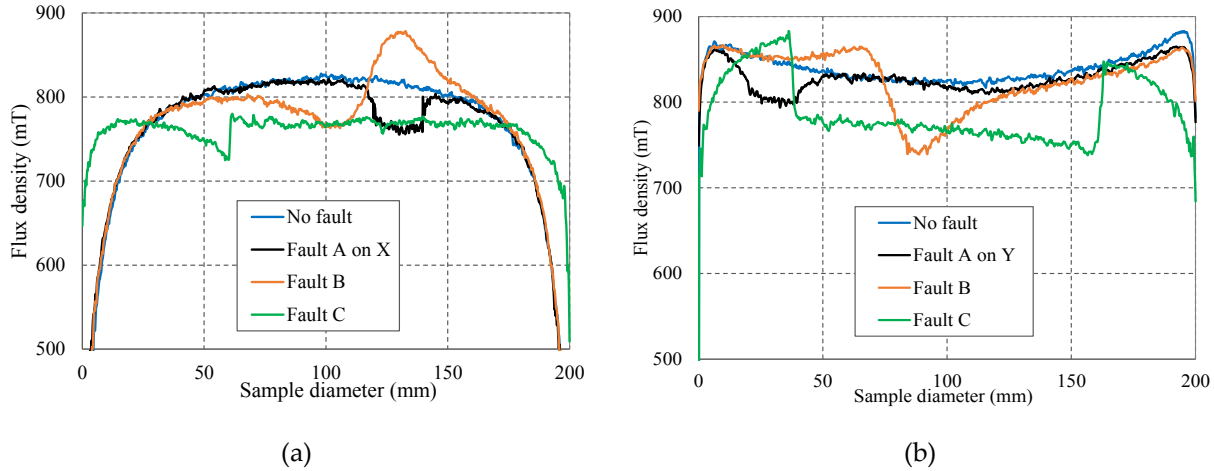


Figure 4-26: Flux density magnitude in the middle of the lower sample with the flux vector in the $-X$ direction (a) In the X direction (b) In the Y direction

Figure 4-26 (a) shows a larger decrease in the flux magnitude compared to the same fault on the y axis in Figure 4-26 (b).

A comparison of other field quantities; magnetic field intensity on the sample surface and current density in the middle of the sample, is shown in Figure 4-27. It was observed that the presence of a fault makes no significant difference in the H profile except for a small fault, which shows spikes in the field intensity at the edges of the fault as indicated in Figure 4-27 (a). At the fault edges, there is a sudden change in the material permeability across the sample which causes the field intensity to also suddenly change even for a somewhat smaller change in flux density. For larger faults this H peak is evened out over a large area and the spikes are less significant as seen with Fault C in Figure 4-27 (a).

The current density magnitude, which shows the eddy currents on the x axis in the middle of the lower sample was also plotted as shown in Figure 4-27 (b). These eddy currents increase in the presence of a fault compared to the no fault case. For example, the average current density across the sample diameter as in Figure 4-27 (b) with no fault is 12.9 kA/m^2 compared to 40.9 kA/m^2 , 23 kA/m^2 , 75.2 kA/m^2 for Fault A, Fault B and Fault C respectively. Fault B current density is less than Fault A current density because Fault B is not directly on the axis where the current density is obtained. The current density plots are obtained on the x -axis with the flux vector also on the x -axis.

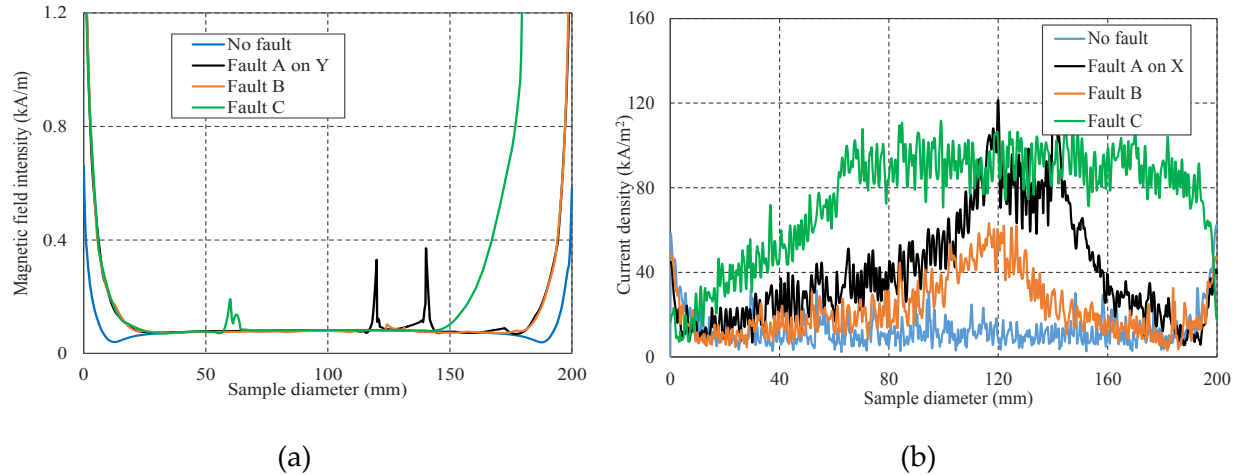


Figure 4-27: Comparison of field quantities across the sample diameter with the magnetization direction in the x axis; (a) Field intensity magnitude on the sample surface, (b) Current density magnitude in the middle of the lower sample

The numerical results above indicated that the presence of a fault causes a distortion in the field distribution, and the current density distribution in the sample. However, ascertaining this by measurement with the existing setup is still a challenge, as the field measurement coils used average the field quantities over a 50 by 50 mm measurement area. Therefore, only the large fault was implemented, whose effect can be observed over the averaged field quantities in the measurement area. Implementing the smaller faults would require a more localized approach to field quantity acquisition, currently unavailable in the laboratory.

4.4.3 Experimental measurement

Four 200 mm diameter samples cut from non-oriented M15G29 samples were prepared for measurement. Due to the power limitations of the amplifiers and the current limitations of the phase windings, only a maximum of two samples were stacked, and the flux density limited to 1 T. Two sets of samples were prepared, one with no fault and the other with a fault imposed. The fault was imposed by removing the surface insulation as shown in Figure 4-28.

Twenty turns of **B**-coils were wrapped around the two sets of two samples each, and around only one lamination. This allows comparison of loss measurements for one sample verses two samples, and the no fault verses faulted laminations. The **H**-coils consist of 240 turns

wrapped around a former to cover a 50 by 50 mm measurement area, placed above and below the samples.

Figure 4-29 shows the measurement setup, which consists of two amplifiers that provide the magnetizing current to the x and y windings. The amplifier input signals are controlled from the computer via dSPACE with reference to the measured $\mathbf{B}_{x,y}$ sensor signals. The $\mathbf{B}_{x,y}$ magnitude, and phase shift between the \mathbf{B}_x and \mathbf{B}_y waveforms is controlled in the dSPACE interface. Magnetizing currents were measured to ensure they are limited to less than the 10 A rating. Captured $\mathbf{B}_{x,y}$ and $\mathbf{H}_{x,y}$ waveforms in the clockwise(CW) and counterclockwise(CCW) direction

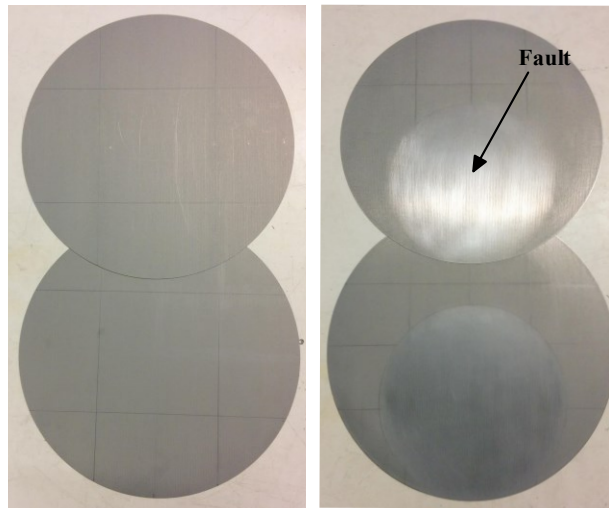


Figure 4-28: Samples before and after the fault is imposed

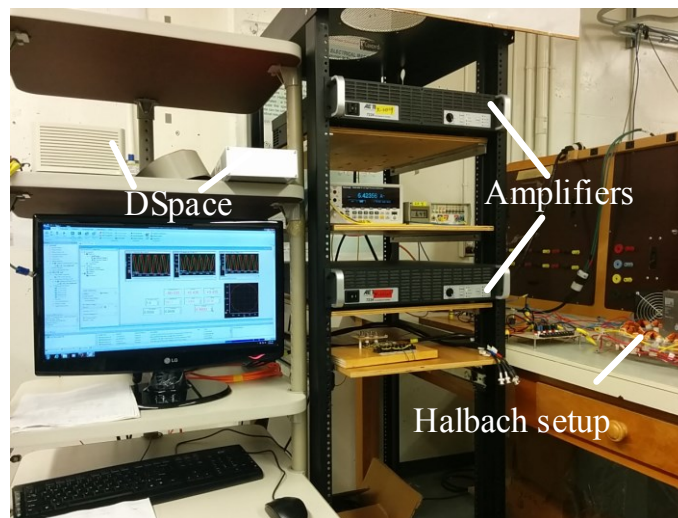


Figure 4-29: Rotational core loss measurement setup

were used in post processing to calculate the total core losses at different flux densities and frequencies.

4.4.3.1 One lamination verses two laminations

The first set of measurements was done to validate the ability of the test bench to measure losses using two samples. This was done by comparing the rotational core loss when one and two laminations of the same material are used. Figure 4-30 shows that the measured losses at 60 Hz with one and two samples is the same. However because of the limitation of the amplifiers the maximum achievable \mathbf{B} for two laminations is restricted to 1 T.

4.4.3.2 Faulted verses non faulted laminations

The measured $\mathbf{B}_{x,y}$ waveforms at 1 T in the CW and CCW direction are shown in Figure 4-31. The waveforms in both the no fault and fault cases were sinusoidal, because the $\mathbf{B}_{x,y}$ magnitude is controlled to ensure rotating flux and the same point of measurement for comparison purposes. In addition, the \mathbf{B} -coils measure the induced field as an average over the entire sample, which makes the localized fault signatures on the \mathbf{B} unnoticeable.

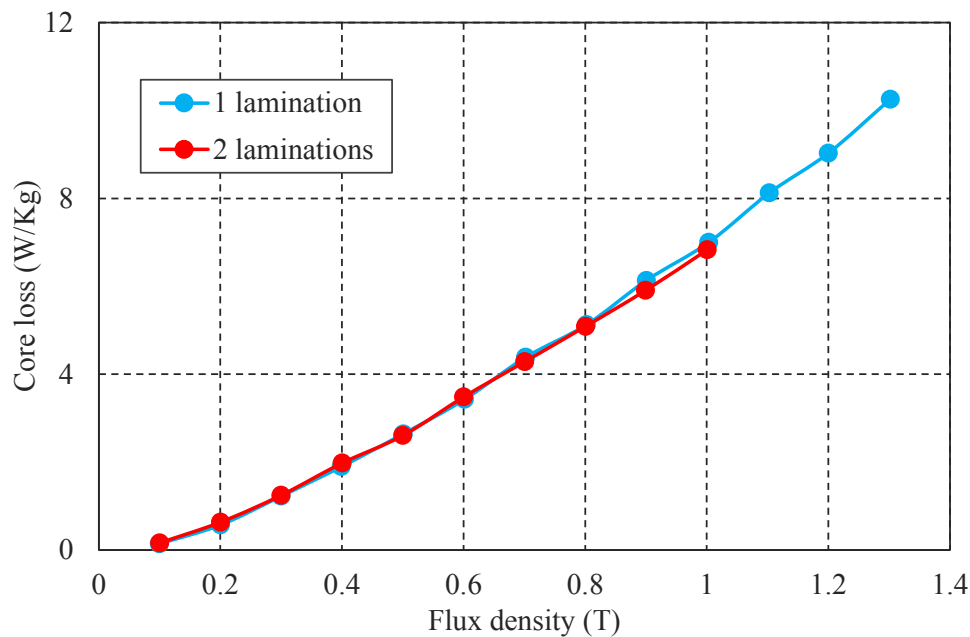
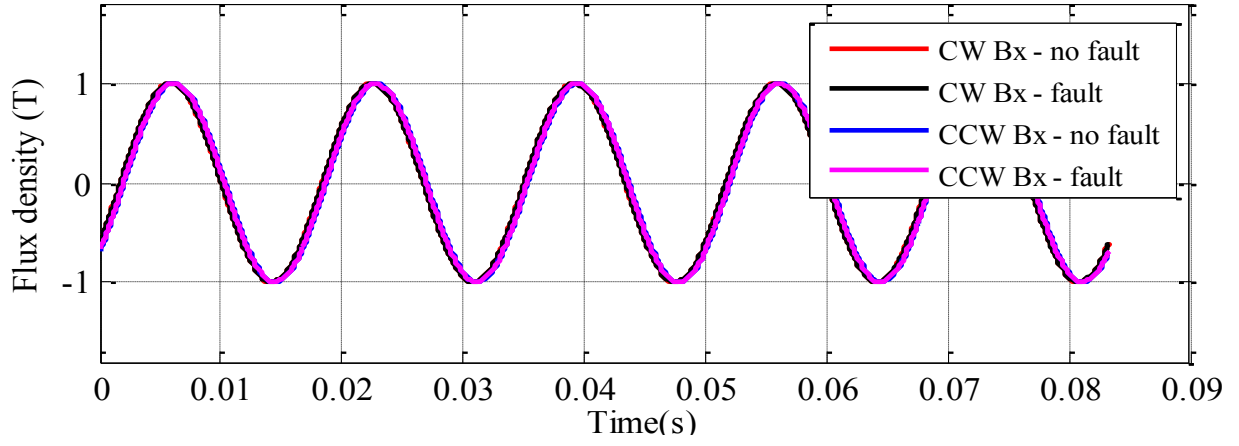
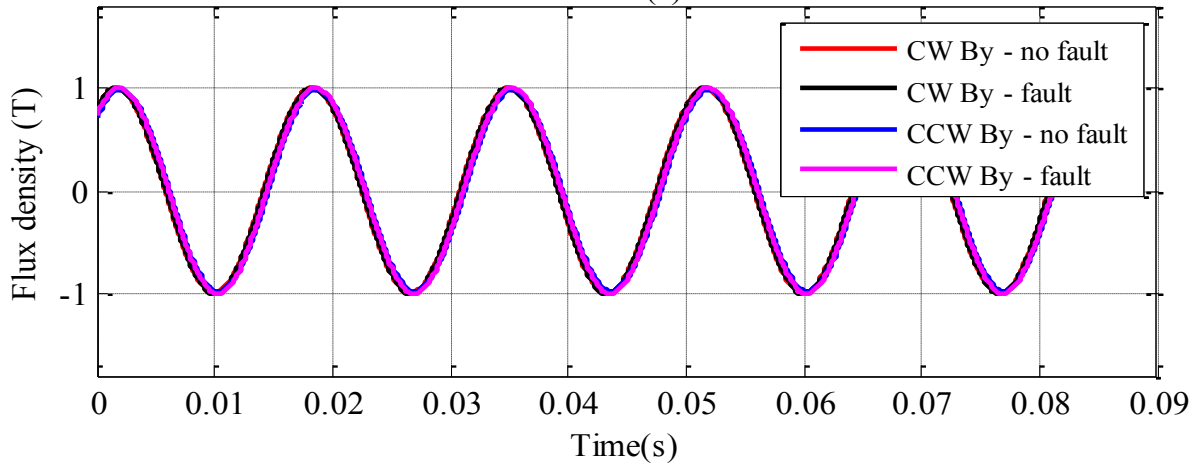


Figure 4-30: Core losses for M15G29 measured with one sample and with two samples



(a)



(b)

Figure 4-31: Flux density waveforms from the $B_{x,y}$ sensors for the fault and no fault condition in the (a) clockwise and (b) counterclockwise direction

Figure 4-32 shows the H_x and H_y in the CW and CCW directions for both the fault and no fault cases. The sample rolling direction was aligned with the x axis hence, the values of H_x were lower than the values of H_y . The fault was aligned to the y axis which explains the higher distortion in the H_y than the H_x fields. Generally, the faulted cases show a distortion in the H especially on the y axis where the fault is located.

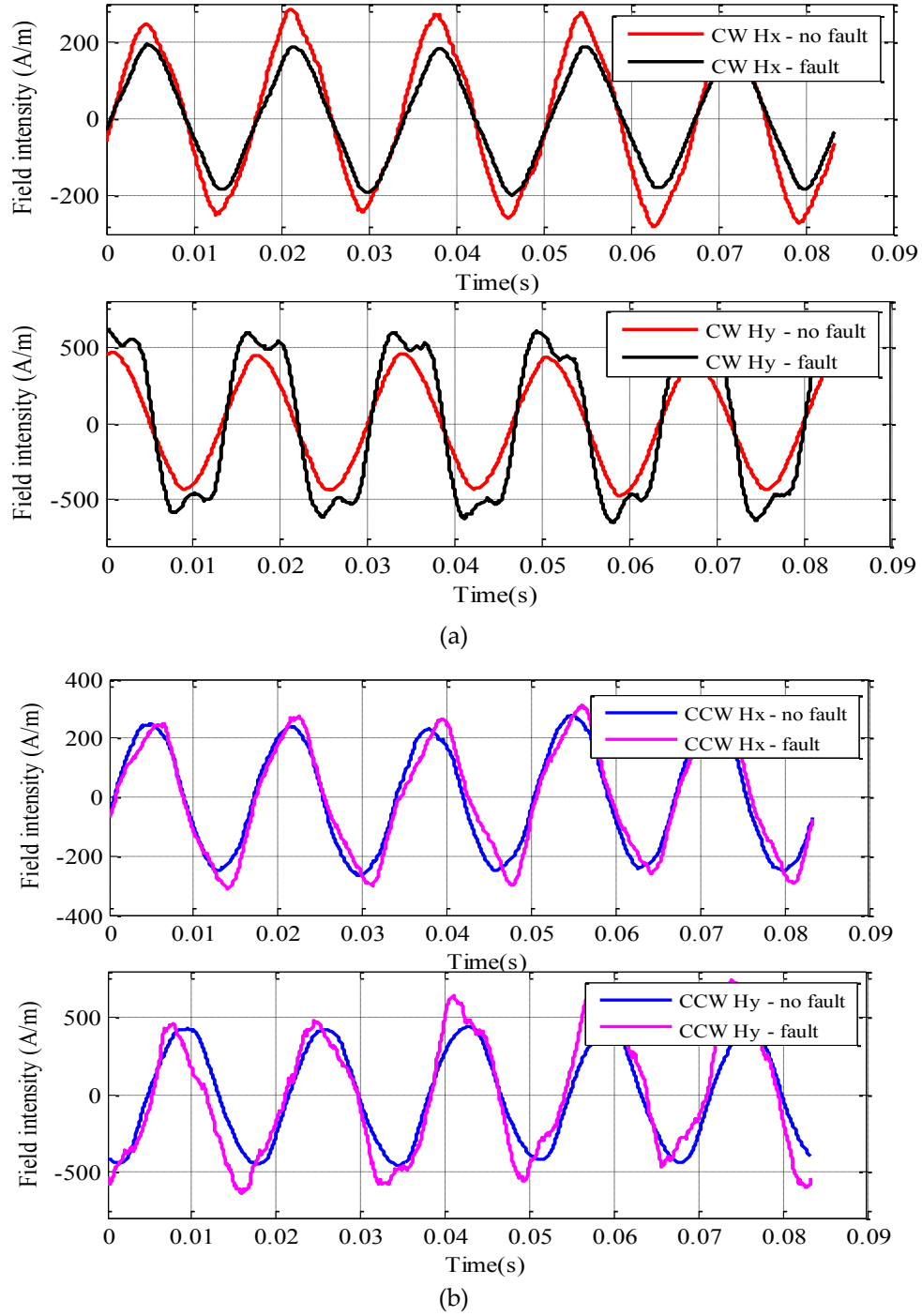


Figure 4-32: Field intensity from the $\mathbf{H}_{x,y}$ sensors for the fault and no fault condition in the (a) clockwise and (b) counterclockwise directions

The interference from the increased eddy currents in the faulted laminations cause the distortion in the measured \mathbf{H} . This distortion is dependent on the amount of eddy currents the fault induces. The experimental results also show that the distortion is dependent on the direction

of rotation (CW and CCW). Compared to simulated results, where the field distortion occurs in the localized **B** distribution across the sample, the measured results show the field distortion in the measured **H**. This difference is because the simulation results show localized flux density magnitude across the sample diameter, while experiments determine the fields from the induced voltage in the **B**-coils. This induced EMF from the coil, averages the flux density along the length of B-coils, hence **B** fault signatures are not visible. Moreover, the average flux density magnitude in the sample is controlled in experimental measurements. The local **H** measurements on the surface of the sample in simulation also shows some fault signatures. The experimentally measured **H** however shows more significant distortion since it is uncontrolled in relation to **B** therefore responds to the presence of a fault.

Figure 4-33 (a) shows the associated core losses for fault C at 60 Hz. Total rotational core losses are often considered an average of the losses in the CW and CCW losses, this reduces the errors due to the sensor alignment. The average losses of the faulted case were higher than the no fault case albeit by a 5% difference. The magnitude and effect of the fault on core losses is dependent on the increased eddy currents, which increase with the number of faulted laminations and the operating frequency. An investigation of a larger number of laminations and higher frequencies is required for further verification. Due to limitations of the power supply and phase windings, more number of laminations was not considered. However, the effect of frequency was investigated as presented in the next section.

4.4.3.3 Higher frequency

Eddy currents increase with frequency therefore measurements were done at higher frequencies. Core losses at two frequencies, 400 Hz and 1 kHz are shown in Figure 4-33 (b) as an average of the CW and CCW measurements. The maximum flux density reached in both cases was determined by the limitations of the measurement system.

Compared to the 60 Hz measurement, the difference between the no fault and faulted cases increases with frequency even when only two faulted laminations are considered. For example as shown in Figure 4-33 (a) and (b) at 0.6 T, for 60 Hz the faulted laminations have 4% more core loss, at 400 Hz they increase to 6% and 1 kHz to 9% compared to their respective no

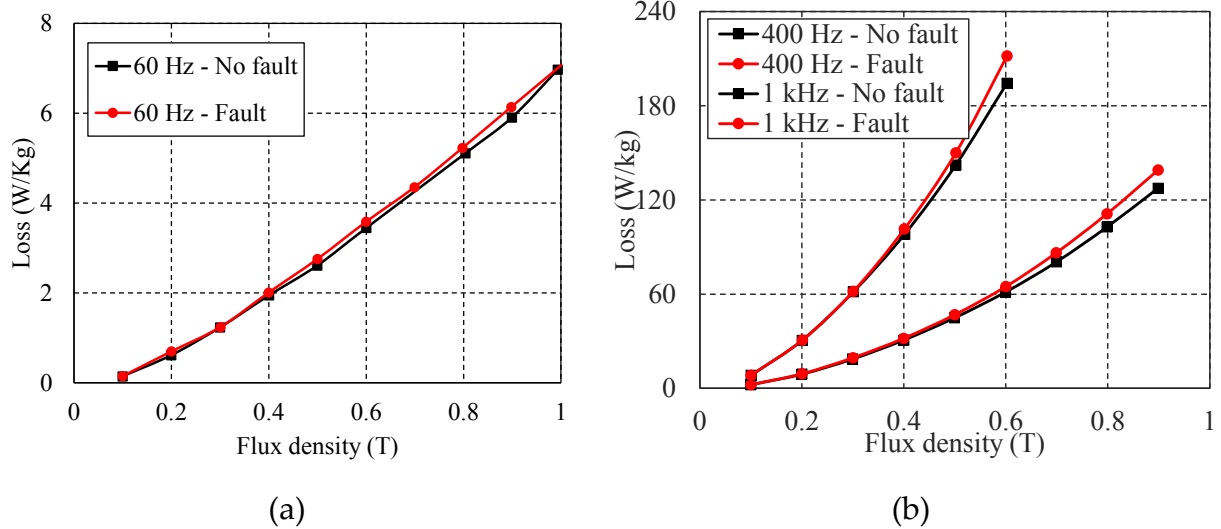


Figure 4-33: Rotational core losses (a) at 60 Hz (b) at 400 Hz and 1 kHz for both faulted and non-faulted laminations.

fault cases. In the real machine this fault can involve an entire packet of over 50 laminations stacked together, the increase in core loss would be significant even if the fault size is not as large as implemented in the sample.

4.4.4 Conclusion

Lamination faults in large machines if unattended can lead to the core melting. The location of these faults in the machine occurs in the stator yoke where there is rotational flux. This section presented an analysis of the effect of lamination faults on rotational flux and rotational core losses.

Several faults were simulated and one fault implemented in lamination samples. The measured core losses showed a 5% increase in the core losses at 60 Hz when only two laminations were shorted. Typically the losses increased with an increase in frequency. More importantly, the measured field quantities in the presence of a fault were distorted compared to the case without a fault. Further analysis and quantification of this characteristic can be explored to develop a lamination fault detection tool that can be used in a real machine.

4.5 Summary

The design process of a rotational flux magnetizer has been presented. Simulation results for the flux density distribution in the magnetizer and sample with different variation of the

magnetizer dimensions and parameters were shown. These included the winding pattern, magnetizer yoke depth and sample diameter. A final design was chosen based on the large sample measurement area.

The final design was prototyped and a set-up to measure core losses in circular samples using the fieldmetric method. Measurements were performed for several frequencies, flux densities and aspect ratios. Moreover, low frequency measurements (at 10 Hz) were used for loss separation.

The effect of size and position of faults on the rotating flux density was examined using numerical simulations. Results showed that the presence of the fault causes non uniform distribution of \mathbf{B} in the sample depending on the size and location of the fault. In addition the area around the fault was also affected by the fault size and magnetization direction.

Implementation of the fault on real laminations revealed higher losses for the faulted laminations compared to the no fault laminations, even for only two faulted laminations. Furthermore, the measured magnetic field intensity waveforms in the presence of a fault were distorted, this can further be developed as a tool to detect lamination faults.

Chapter 5 : Core Loss Estimation and Flux density Control

Core losses in machines are typically estimated using two main methods; analytical models whose coefficients are obtained from measured core losses, and curve fitting of measured data. Both techniques are applied to complex machine flux density distributions to estimate the total machine core losses, and have been used in several machine design software. However, these methods are dependent on the availability of measured soft magnetic material data.

For lack of measured rotational core loss data, rotational core losses have not been accounted for in machine core loss estimation. Therefore in this chapter, using the measured rotational core losses in chapter 4, a method is proposed to estimate the total core losses in the machine including the rotational core loss component. Moreover, the method considers both sinusoidal and non-sinusoidal flux density as in the machine.

To facilitate the calculation of core losses using non-sinusoidal rotational core loss measurements, a flux density waveform controller is designed and implemented. In addition, this waveform controller is also used to maintain sinusoidal flux density waveforms in the sample at saturation. Simulation and experimental results of the controller performance are also presented.

5.1 Core loss estimation

The core loss measurements on M19G29 soft magnetic material in chapter 4 were used for core loss estimation in this section. The 60 Hz measured data at different sinusoidal flux densities and aspect ratios was post processed to compute losses for purely sinusoidal flux densities and later extended to non-sinusoidal flux density.

5.1.1 Sinusoidal flux density core loss estimation

As previously shown, the flux density and aspect ratio distribution in the stator core is non-uniform. Additionally, measured data is only available for some discrete flux densities and aspect ratios, which are inadequate to calculate the losses everywhere in the machine. As a result,

a polynomial surface fit of the measured sinusoidal rotational data is defined to allow the loss calculation at any arbitrary flux density and aspect ratio.

Figure 5-1 (a) shows the fitted rotational core loss surface, with the black dots indicating the measured losses. The goodness of the fit is defined by $R\text{-squared} = 0.9972$, sum of squares due to error (SSE) = 0.9852 and root mean squared error (RMSE) = 0.09023. A visual representation of the goodness fit is shown in Figure 5-1 (b), which indicates the fit within an error of 15%, at mostly high flux densities. For realistic combinations of flux density and aspect ratio present in the machine, the error is within 5% thus the surface fit is sufficient for core loss estimation.

This loss surface was used to compute the losses in each stator mesh element using their respective combination of the peak flux density magnitude and aspect ratio. Pulsating losses were also calculated using the loss surface with $R = 0$. This approach was used to calculate losses in the machine stator at no and full load operating conditions. In addition, the loss surface was also used to calculate the stator core losses for the different machine designs presented in chapter 3.

5.1.1.1 No load and full load

Loss separation in large synchronous machines is based on the assumption that the core losses at no load and full load are the same [6]. This is founded on the fact that at no load rated

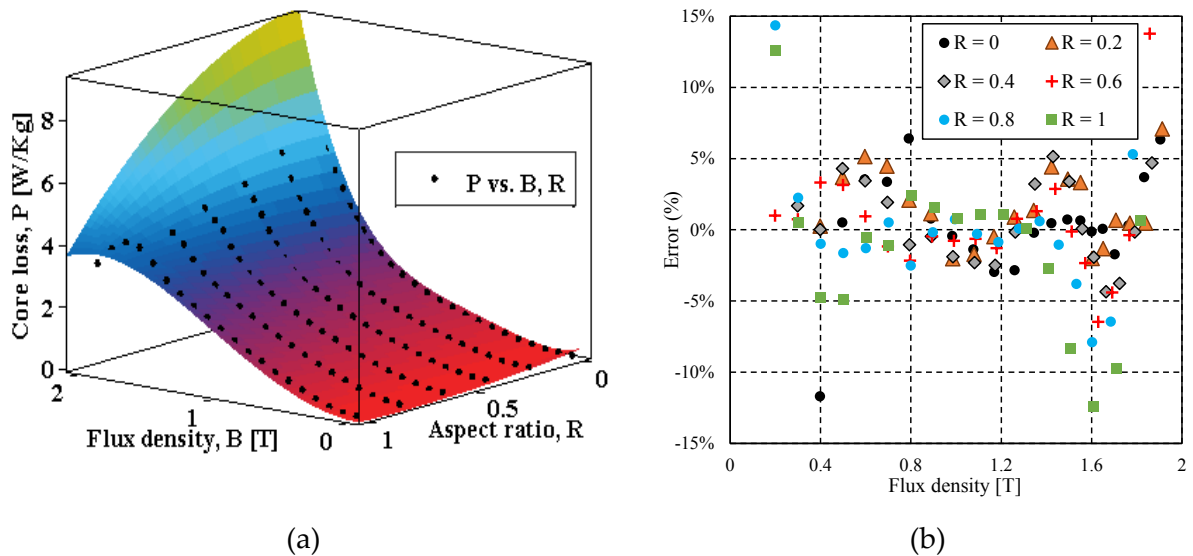


Figure 5-1: Measured rotational core loss; (a) surface of the rotational core loss data, (b) goodness of the fitted surface

voltage and at full load, the output rms voltage is the same, hence the assumption that the flux density in the machine at both operating points is the same. However this is not the case as shown by the flux density waveforms at different points of the machine in Figure 5-2, where the waveforms are different in both operating conditions. The flux density waveforms were extracted from the same points and same time steps in the stator after no load and full load simulations. A comparison of the waveforms indicates different operating points on the material **BH** curve. This is shown by the difference in the maximum flux density at both operating conditions.

Changing the operating point on the material **BH** curve affects both the shape and magnitude of the localized flux density and hence the aspect ratio. Moreover, full load operation induces some harmonics, and includes armature reaction which further affect the flux density shape and magnitude in the machine stator as shown in Table 5-1. For instance, the flux density fundamental peak at the tooth is 1.48 T for no load and 1.87 T at the same point for full load. Furthermore, for the back of the tooth, the flux density fundamental peak does not only change but so does the aspect ratio from 0.66 to 0.8. Consequently, the associated core losses in the no load and full load operating conditions will be different. A loss increase of over 50% was obtained when the calculated stator losses from no load to full load were compared, including both the pulsating and rotational components.

The rotational core loss surface fit was applied to calculate the stator losses in each mesh element, by considering only the fundamental flux density component from the extracted stator mesh flux density. This was done at both no load and full load, and the total losses obtained as a

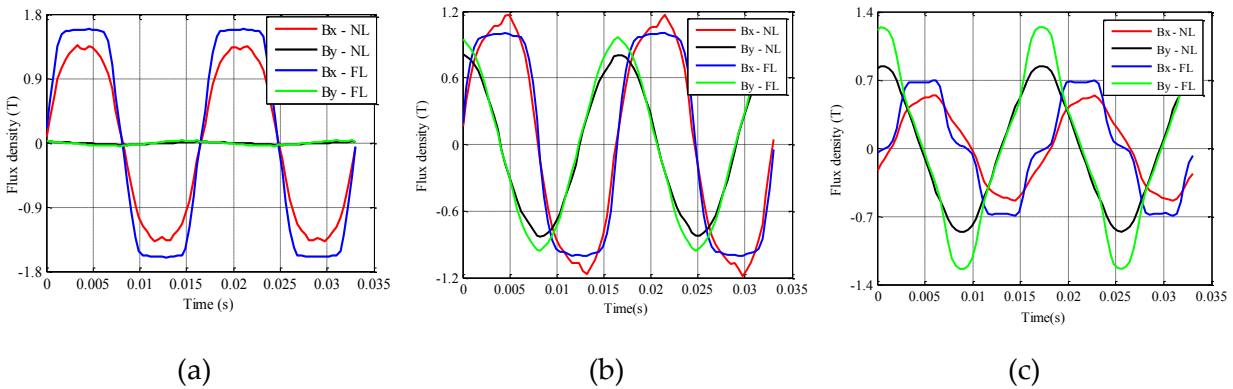


Figure 5-2: Flux density plot at no load and full load for (a) Point 1: Tooth; (b) Point 2: Back of the tooth; (c) Point 3: Back of the slot

sum of each mesh loss as shown in Table 5-1. Pulsating losses were calculated assuming all $R = 0$ in the loss surface fit. This reduces the surface to a line, which is a function of flux density magnitude with a constant $R = 0$.

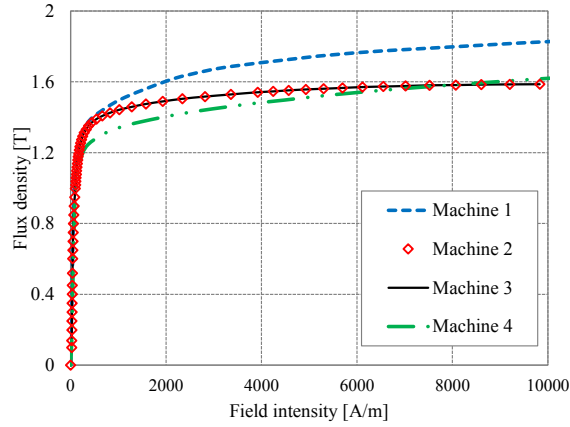
Table 5-1 also shows that including the rotational component increases the losses by 11% in both the no load and full load operating conditions of this machine. Rotational core losses at any frequency are a function of the flux density magnitude and aspect ratio, which are also dependent on the machine design and operating point as was shown in chapter 3. Therefore, in the next subsection a comparison of the core losses in the different machine designs of section 3.4 are presented.

Table 5-1 No load and full load flux density and core loss

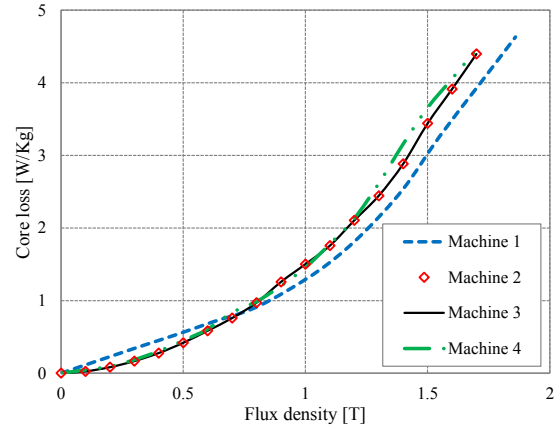
		B_x (T)	B_y (T)	R	Core Losses (kW)	
					Pulsating	Rotational
No Load	Tooth	1.48	0.02	0.01		
	Tooth	1.21	0.81	0.66	26.198	29.116
	Back					
	Slot	0.53	0.82	0.59		
Full Load	Back					
	Tooth	1.87	0.03	0.03		
	Tooth	1.18	0.94	0.80	41.228	45.710
	Back					
	Slot	0.68	1.11	0.61		
	Back					

5.1.1.2 Calculation in different machines

The core loss estimation approach presented in section 5.1.1.1 was used to calculate the core losses of the different machine designs presented in section 3.4. The machines have different stator and rotor material properties as shown in Figure 5-3 and Figure 5-4 respectively. This difference in material properties, together with the different machine ratings and geometry result in different core losses. However for comparison purposes, and for lack of stator material samples to measure the rotational core losses, the same measured rotational core loss data of M19G29 steel was used for loss calculation in all the machine stators.

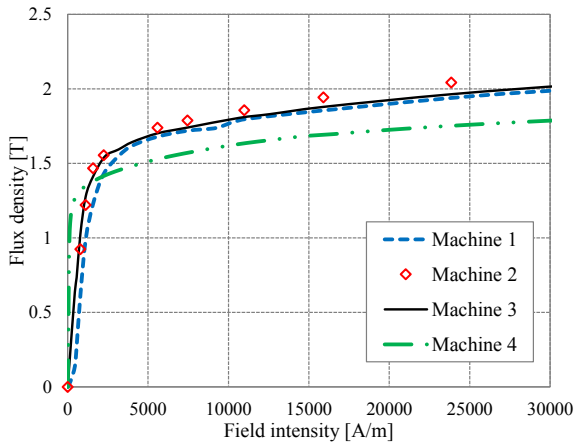


(a)

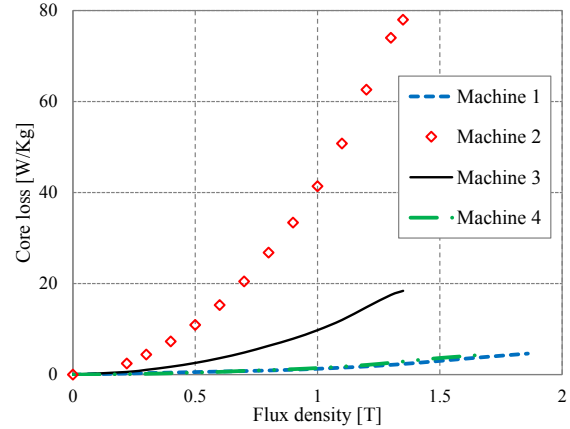


(b)

Figure 5-3: Measured stator material properties at 60 Hz; (a) **BH** curve, (b) Core losses



(a)

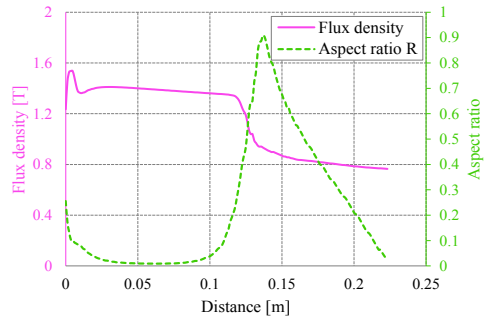


(b)

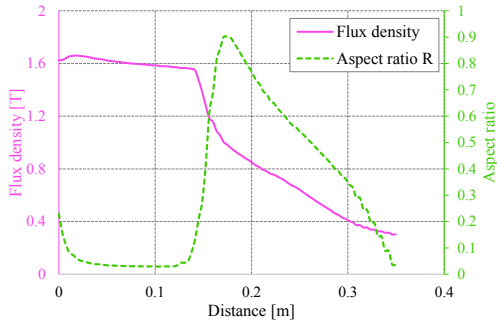
Figure 5-4: Measured rotor material properties at 60 Hz; (a) **BH** curve, (b) Core losses

Figure 5-5 shows the aspect ratio, flux density and the associated core losses plotted on a radial line along the stator core, from the stator tooth to the stator yoke. Along the tooth, the aspect ratio is low, less than 0.1 and peaks at the tooth back as shown in Figure 5-5 (a). Towards the end of the stator yoke, the aspect reduces to less than 0.1 again. Flux density distribution along the stator tooth length is high and reduces towards the end of the yoke length.

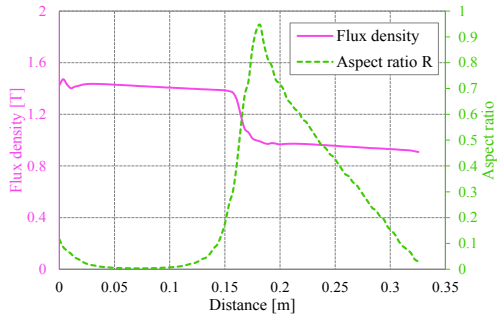
Figure 5-5 (b) shows the calculated core losses; pulsating and rotating losses using the surface fit defined in the previous section. All machines have the same core losses in the stator tooth, where the aspect ratio is less than 0.1. In the yoke where the aspect ratio is high, the rotational losses are accordingly higher than the pulsating losses.



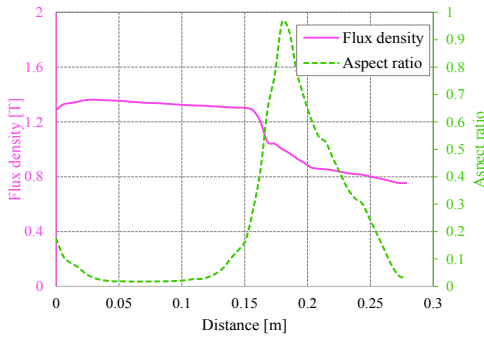
(i)



(ii)

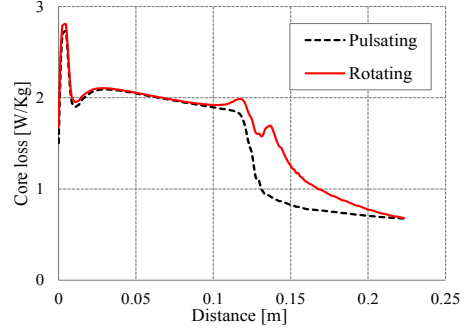


(iii)

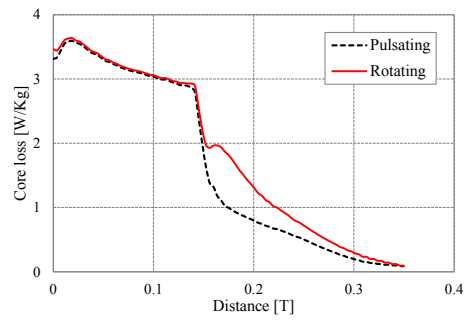


(iv)

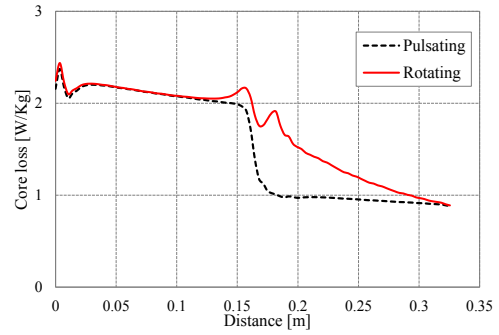
(a)



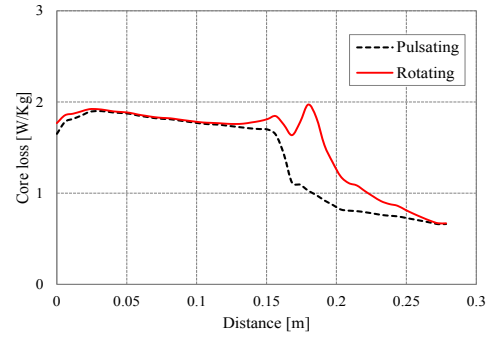
(i)



(ii)



(iii)



(iv)

(b)

Figure 5-5: Comparison of machines with data from the stator radial line through the tooth to the yoke, for (i) Machine 1, (ii) Machine 2, (iii) Machine 3, (iv) Machine 4 where (a) Flux density and Aspect ratio distribution, (b) Core losses, pulsating and rotational core losses distribution

Figure 5-5 (a) (ii) shows that the aspect ratio along the stator length in Machine 2 slowly reduces after peaking, compared to other machines. This is consistent with the aspect ratio plots previously shown in section 3.4. The flux density magnitude in this machine along the same radial line is higher in the tooth but much lower in the yoke compared to other machines. This distribution of aspect ratio and flux density in Machine 2 can be attributed to its large stator yoke. A combination of the flux density magnitude and higher aspect ratio result in the core losses in Figure 5-5 (b) (ii), where including the rotational component shows an increase in the rotational losses. This increase aggregates to 17% in the entire stator as shown in Table 5-2.

Table 5-2 shows the total core losses in the stator of each machine with and without the rotational component. The increase in core losses in each machine is a combination of the machine dimensions, aspect ratio and flux density distribution. From the dimensions in Table 3-2, Machine 2 had the largest stator yoke, which increases the aspect ratio and hence the 17% increase in core losses. Machine 3 and 4 have the longest tooth length, which indicates high flux density over the long tooth length, resulting in an increase in the losses. In addition, Machine 3 with a longer yoke which increases the aspect ratio compared to Machine 4, has a 13% increase in rotational losses. Machine 1 with almost the same tooth and yoke length has an 11% increase in the losses as a result of the flux density and aspect ratio distribution.

Results from the different machines indicate that the percentage increase in core losses is machine design dependent; specifically the stator dimensions. Different dimensions of a machine for the same excitation current result in a different flux density and aspect ratio distribution.

Table 5-2 Stator core loss calculation in different machine designs

	Machine 1	Machine 2	Machine 3	Machine 4
Pulsating (kW)	26.196	68.464	172.008	94.088
Stator Rotational (kW)	29.116	80.244	193.836	104.116
Percentage increase in loss	11%	17%	13%	11%

Although the different machines designs above use different excitation currents for rated open circuit voltage, the effect of stator dimensions on the core losses is apparent. This was shown in the relative difference in the tooth to yoke length ratio among the machines in section 3.4.

The results presented in this section are mainly comparative, therefore the same stator material, M19G29 steel, was used for each machine. However the same approach can be applied to calculate the actual total core losses in each machine, using the rotational core losses for each stator material.

5.1.2 Non-sinusoidal flux density core loss estimation

Core loss estimation presented in the previous section assumes only sinusoidal flux densities, since only the fundamental component is considered. However as alluded to, flux density in the machine stator is not only rotational but also non-sinusoidal, therefore the non-sinusoidal component needs to be accounted for. In this section, the non-sinusoidal component is measured and a method proposed to account for the non-sinusoidal component in the rotational core loss calculation.

5.1.2.1 Method of measurement

The Epstein frame based test setup in [12] was used to measure the extracted non-sinusoidal B_x and B_y waveforms. The FEA flux density waveforms are converted to an exciting voltage signal, and via dSPACE used as inputs to the linear amplifier, which produces a power signal to excite the Epstein frame. Losses were obtained by computing the area of the captured BH loop, and verified with power losses measured with the power meter. The same soft magnetic material, M19G29 steel with 16 lamination strips were used in the Epstein frame for core loss measurement.

Figure 5-6 (a) shows the flux density waveforms extracted from the stator tooth back at no load with aspect ratio of 0.66. Figure 5-6 (b) and Figure 5-6 (c) show the measured flux density waveforms, which are the same as those obtained from FEA. The setup was capable of replicating the non-sinusoidal FEA flux density waveforms, therefore was used to measure core losses with different flux density magnitudes and aspect ratios.

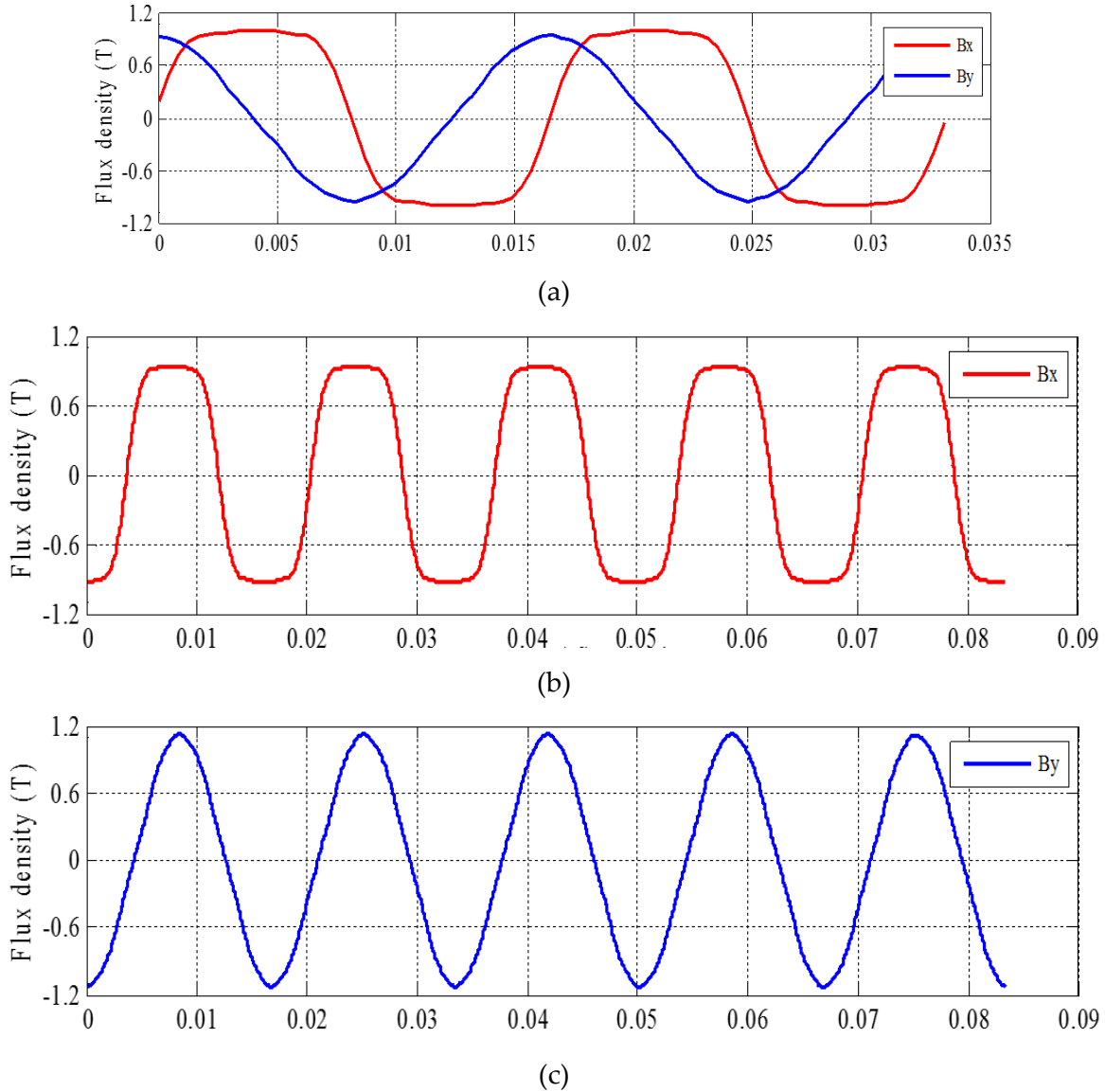


Figure 5-6: Non-sinusoidal waveforms; (a) Flux density waveforms from FEA, (b) Measured B_x waveform, (c) Measured B_y waveform

Other waveforms in the stator tooth and the back of the tooth at full load, were also measured. These measured losses were used in the next section to validate a time domain non-sinusoidal core loss prediction model, which is applied in non-sinusoidal rotational core loss calculation.

5.1.2.2 Core loss calculation

The Epstein measured non-sinusoidal data in the previous section was used to validate the time domain model in [32]. This was done by comparing its core loss prediction of the non-

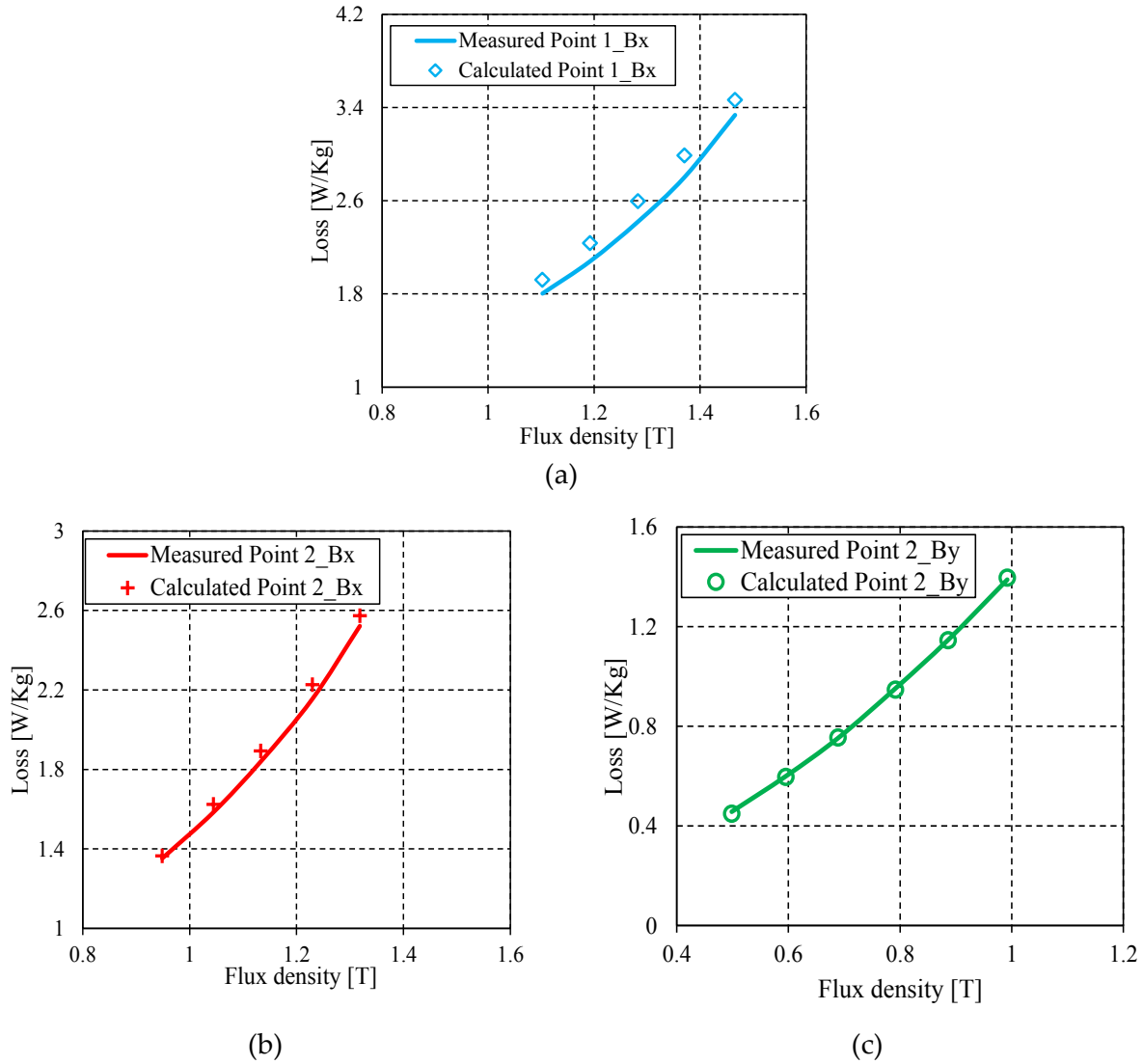


Figure 5-7: Estimation of the non-sinusoidal core loss components at (a) point 1: middle of the tooth B_x , (b) point 2: back of the tooth B_x , and (c) point 2: back of the tooth B_y

sinusoidal waveforms shown in Figure 5-7. The coefficients of this model were determined using the technique presented in [94]. The time domain model was able to precisely predict core losses of non-sinusoidal flux density waveforms within an error of less than 9% for the predicted loss in Figure 5-7 (a). The other non-sinusoidal waveform core loss predictions had an error of less than 3%

To account for both the non-sinusoidal and rotational components, the two sets of experimental results; pulsating non-sinusoidal measurements in section 5.1.2.1 and rotational core loss measurements in section 5.1.1 were used with equation (5.1)

$$P_r = r(B, R) \left[K_{hx} f B^{\alpha x} + K_{ex} \frac{1}{T} \int_0^T \left(\frac{dB_x}{dt} \right)^2 dt + K_{hy} f B^{\alpha y} + K_{ey} \frac{1}{T} \int_0^T \left(\frac{dB_y}{dt} \right)^2 dt \right] \quad 5.1$$

where r is the ratio of rotating loss to pulsating loss determined from the previously measured rotational loss data, it varies with aspect ratio and flux density. B , α , K_h , and K_e are the flux density, the Steinmetz coefficient, the hysteresis and the eddy current coefficients respectively, which are unique for x and y and vary with frequency and flux density, f is the frequency and T is the period of the waveform.

In (5.1), the non-sinusoidal loss component is obtained using the time domain part and the rotational component is included using the variable coefficient r . The coefficient r is a function of aspect ratio and flux density, which can be obtained for any material with measured rotational core losses. This coefficient can be used to calculate the rotational losses of a material only from its pulsating core losses.

Table 5-3 shows the measured sinusoidal equivalent pulsating core losses, measured core losses for the non-sinusoidal waveforms from the back of the stator tooth at no load, and the total core losses, which include both the non-sinusoidal and rotational loss components using equation (5.1) for different flux densities. Only flux density waveforms at the back of the tooth are considered because as shown in Table 5-1, the aspect ratio only changes at that point in the no load and full load operation.

The flux density in Table 5-3 is obtained as a magnitude of the \mathbf{B}_x and \mathbf{B}_y waveforms. Varying the flux density peaks of the \mathbf{B}_x and \mathbf{B}_y waveforms gives different aspect ratios and flux density magnitudes. This enables the calculation of the associated total core losses using (5.1), for different combinations of flux density and aspect ratio. The sinusoidal pulsating loss in Table 5-3 is a sum of the measured fundamental components of the \mathbf{B}_x and \mathbf{B}_y waveforms.

The non-sinusoidal loss in Table 5-3 was found as a sum of the measured losses for the respective \mathbf{B}_x and \mathbf{B}_y non-sinusoidal waveforms. For some of the measured waveforms at 1.46 T and 1.59 T, the pulsating sinusoidal core losses were higher than the non-sinusoidal losses. This is mainly because the fundamental component of the measured non-sinusoidal waveform was

Table 5-3 Core loss estimation considering the non-sinusoidal component

Aspect ratio, R	Flux density [T]	Sinusoidal pulsating loss W/Kg	Non-sinusoidal loss W/Kg	Total loss W/Kg
0.53	1.07	1.75	1.81	2.46
0.53	1.28	2.47	2.49	3.22
0.57	1.20	2.18	2.22	2.99
0.61	1.33	2.66	2.65	3.49
0.64	1.46	3.31	3.17	4.03
0.67	1.59	4.02	3.72	4.49

higher than the peak of the non-sinusoidal waveforms, which results into higher losses. The total core losses in Table 5-3 include both the non-sinusoidal and rotational core loss components. These total losses were significantly higher (12-40% higher) than just considering the pulsating component, for the flux density waveforms and aspect ratios assessed.

The conclusions from this section indicate that in calculation of core losses in machines, it is required to account for both the non-sinusoidal and rotational core loss components simultaneously. The challenge to this, is the ability to experimentally quantify both the rotational and non-sinusoidal components simultaneously, by only using non-sinusoidal rotational measured data. This requires the implementation of flux density waveform control in the rotational core loss test bench, typically with feedback control. The following section therefore presents the implementation of feedback control in the rotational core loss measurement test bench

5.2 Flux density waveform control

Rotational core losses are often measured using sinusoidal excitation waveforms at different aspect ratios. Most measurement systems operate in the open loop therefore, at high flux densities the measured waveforms are distorted and non-sinusoidal due to material saturation. This is caused by the non-linearity of both the sample and test rig material at high flux density, which is also a function of the type of test rig used. Additionally, non-sinusoidal waveforms cannot be implemented in the open loop operation. Therefore, different closed loop

techniques have been used to maintain sinusoidal flux density waveforms at high flux densities, and in some cases used to measure specific non-sinusoidal waveforms.

The challenge to controlling the waveform lies in the fact that the system is non-linear and its transfer function changes with the point being measured, level of flux density and frequency. This is further complicated by the flux path, which is completed through the test rig, thus contributing to the non-linearities, especially at high flux densities. Therefore an adaptive controller is required to control the flux density waveform particularly at high flux densities when the material starts to saturate.

In [95] an adaptive proportional controller is proposed to maintain a sinusoidal field (**H** or **B**). This was done by compensating for the harmonics using Fourier analysis on the error signal, modifying the phase harmonics and performing an inverse Fourier transform, all of which require a lot of processing time, and therefore has a large convergence time. A combination of analog and digital control is applied in [96], where the digital control is done for the flux density phase, frequency and amplitude control, and the analog control is done for the waveform shape. In [97] and [98], a comparison of analog and digital flux density waveform controllers were presented for pulsating measurements. Digital controllers were preferred for their versatility.

Other methods are reported in [99], [100] and [101] all using digital control with digital low pass filters and isolating transformers to remove any dc components from the controller output. The methods also use Fourier analysis to compensate for the waveform harmonics. Low pass filters create flux density level and frequency dependent phase shifts, which make the phase shift compensation difficult. In addition, real time Fourier analysis and processing of the waveforms is processor intensive and the success of the method depends on accurate compensation of not only the harmonic magnitudes but also their phases.

In this section, waveform control is implemented using a proportional and integral (PI) controller in the DQ frame. This concept has been successfully used in the vector control of electrical machines, therefore was adapted for the waveform control in rotational flux density measurements. The DQ frame control eliminates the need for low pass filters and isolators as the output can never contain a dc component. Moreover, the need for Fourier analysis and harmonic

compensation in real time is eliminated. This makes the control simple but robust enough to achieve sinusoidal waveforms at high flux densities, and measure desired non-sinusoidal waveforms. Owing to the highly non-linear system, whose transfer function changes with the level of flux density and frequency measured, the PI gains are appropriately tuned before results are captured.

The details on the DQ modelling for the test set-up, the control block diagram, simulation and experimental results are presented below. Experimental results for both controlled sinusoidal waveforms at high frequencies and non-sinusoidal waveforms are also shown.

5.2.1 DQ equivalent for the measurement set up

The dq transformation is a space vector transformation of three phase quantities (currents or voltages) from a stationary coordinate system to a rotating coordinate system. Figure 5-8 shows the schematic of the transform steps from the stationary 3phase reference frame (ABC) to the two-axis orthogonal stationary frame ($\alpha\beta$), and finally to the rotating frame (dq). This transformation is commonly used in the vector control of permanent magnet synchronous machines and induction machines.

This transform was adopted and adapted for the design and implementation of a controller for the rotational core loss measurement set up. Waveform control in the dq frame is not only easier as the components are dc voltages therefore a simple PI controller can be used, but also for this setup the dq frame ensures that dc components are not provided as inputs to the

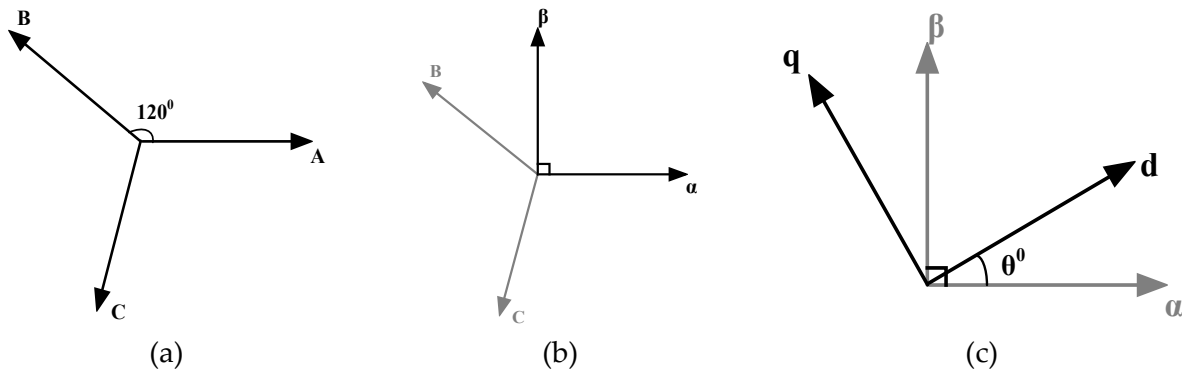


Figure 5-8: DQ transformation stages (a) 3 phase symmetrical system (ABC), (b) Clarke transform from ABC to $\alpha\beta$, (c) Park transform from $\alpha\beta$ to dq

amplifier. Therefore no need for digital low pass filters and transformer isolators. Moreover, the fieldmetric method used in this setup relies on the rate of change of flux to measure the field quantities therefore, only AC fields can be measured. Any DC field components in the system would consequently not be measured, which can cause instability in the feedback loop, saturation in the material and over loading of the amplifiers even at low flux densities.

Figure 5-9 shows the schematic of how the dq transform is adapted for the rotational core loss test set up. The setup is already a two phase orthogonal system, therefore $v_\alpha = v_x$, $v_\beta = v_y$, which neglects the use of the Clarke transform. The v_x and v_y phase voltages are thus directly converted to dq voltages in Figure 5-9 using equation (5.2) and its inverse in equation (5.3)

$$\begin{aligned} u_d &= v_x \cos(\theta) + v_y \sin(\theta) \\ u_q &= -v_x \sin(\theta) + v_y \cos(\theta) \end{aligned} \quad 5.2$$

$$\begin{aligned} v_x &= u_d \cos(\theta) - u_q \sin(\theta) \\ v_y &= u_d \sin(\theta) + u_q \cos(\theta) \end{aligned} \quad 5.3$$

where u_d and u_q are the dq voltages, v_x and v_y are the winding voltages in the ABC frame, and θ is the rotation angle. These dq voltages are used in the feedback control loop using a PI controller for waveform control. In the next section the closed loop block diagram is presented together with some simulation and experimental results.

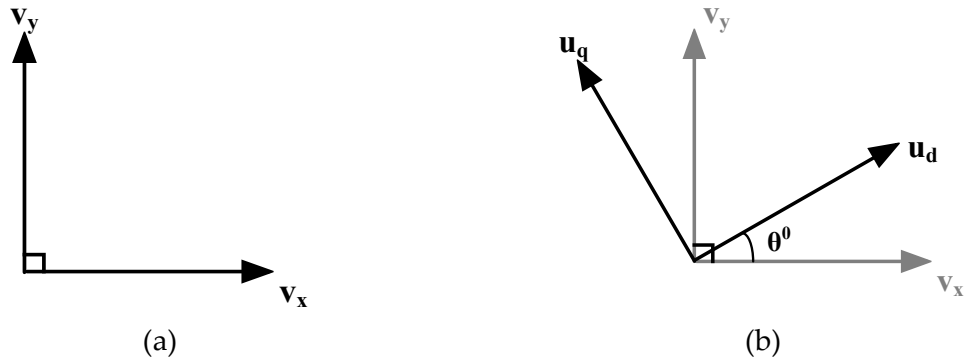


Figure 5-9: DQ transformation for the rotational test setup (a) 2 phase rotational flux system, (b) DQ transformation of the 2 phase system.

5.2.2 Feedback loop

Figure 5-10 shows the block diagram of the feedback control implemented with a PI controller in the dq frame. The proportional and integral gains were tuned to follow the reference with in an error of 2% at maximum flux density. Reference signals for phase x and phase y are generated and converted into dq signals, which are inverted back to v_x and v_y after the PI controllers. The real time controller, dSPACE in this case, converts this digital signal into an analog signal that is amplified to a power signal to magnetize the test rig. The feedback signal is obtained from the B-coils, converted into the dq frame and compared to the reference signal.

The phases are independently controlled as each phase has its own PI controller, one for u_d , which is linked to phase x and the other for u_q , which is linked to phase y. This is important as the material characteristics in the sample are anisotropic along the rolling and transverse direction even for a non-oriented material. Therefore the design of the controller is different for the two phases.

5.2.2.1 Simulation results

The test rig and sample is a difficult problem to model as a transfer function because of the flux leakage between the rig and sample, the sample anisotropy based on the rolling direction, coupling between the x and y phases, and material saturation. Therefore in simulation, a simple approximation of the system is modeled with a first order transfer function and a look up table of M19G29 magnetizing curve data in the x and y axes respectively.

Figure 5-11 shows the simulation diagram for the feedback loop, where the transfer function and look up tables which indicate the plant are shown in blue, the dq transformations in

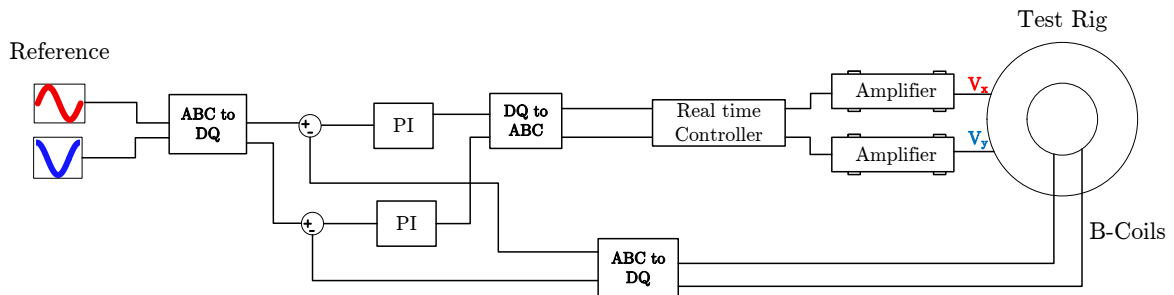


Figure 5-10: Block diagram of the feedback loop for waveform control

green, the flux density peak for both phases in red and the scope to compare the output and reference in pink. Also included are the saturation blocks to limit the output, dSPACE gains for the conversion and the **B**-coils constant.

A fixed step continuous solver of eighth order accuracy is used for simulation with a time step of 16 μs . The time step was later adjusted to enable program execution in real-time without overruns. The angle of rotation, $\theta = \omega t$ is generated together with the reference waveforms, and also used in the dq transformations as shown in equations (5.2) and (5.3). The flux density peak can be varied as desired, and different flux density harmonics can also be added to the phases independently. This enables core loss measurement of arbitrary waveforms.

The simulation results are shown in Figure 5-12 when the flux density peak is increased from 0 to 1 T, then to 1.5 T and finally to 2 T. This examines the controller's ability to respond to a change in the reference. Moreover, it also enables the testing of the proportional and integral gains. The corresponding error between the reference and the feedback \mathbf{B}_x and \mathbf{B}_y waveforms was determined as also shown in Figure 5-12. The largest error was 2% in both the \mathbf{B}_x and \mathbf{B}_y waveforms at 2 T, at lower flux densities the error was less than 1%.

In the next section, this closed loop is implemented in the rotational core loss test measurement. The proportional and integral gains on both phases were appropriately tuned to suit the magnetic circuit, and also function during material saturation at high flux densities.

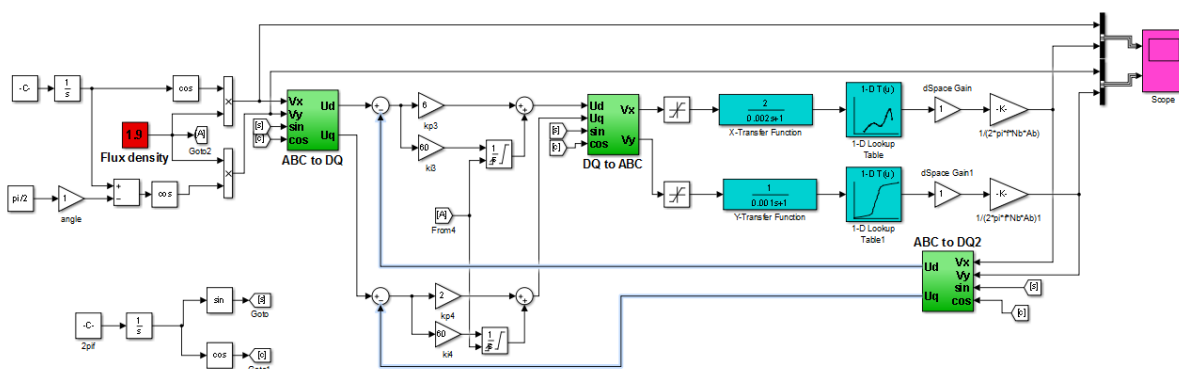
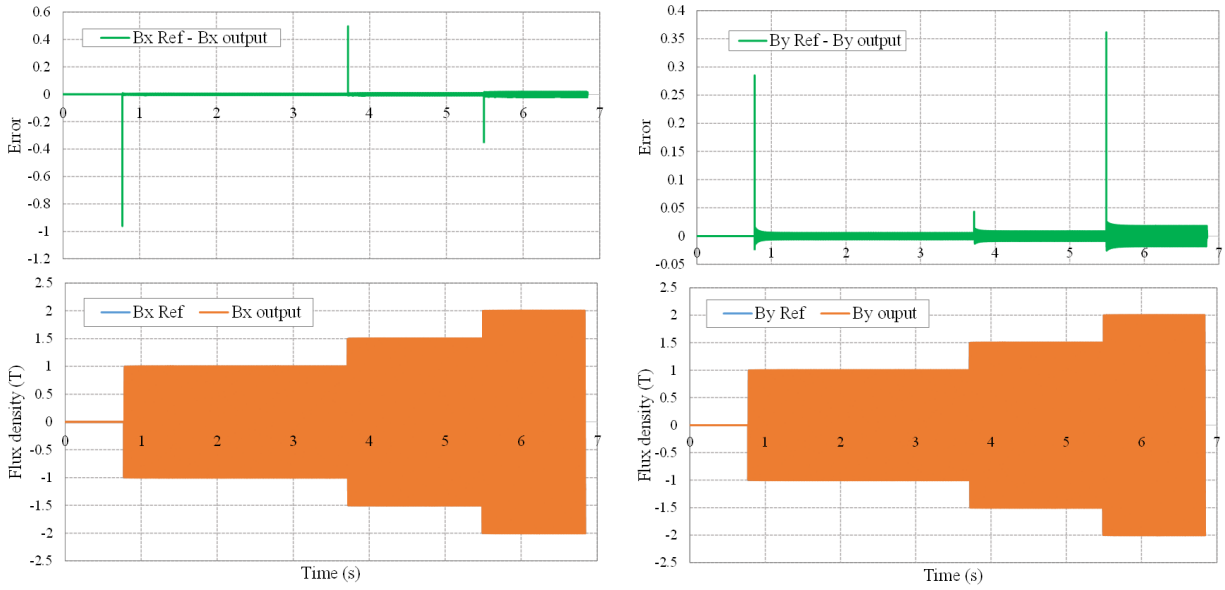


Figure 5-11: Simulation diagram of the feedback loop for waveform control

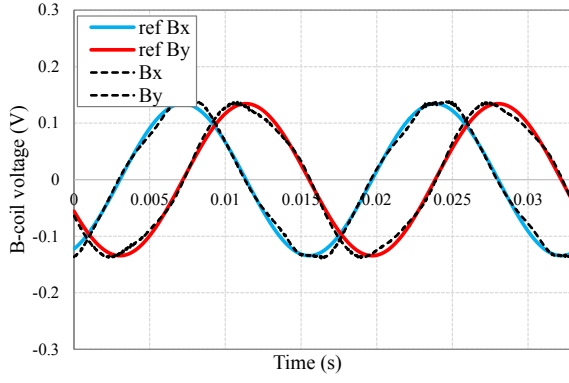


(a) B_x waveforms and error, (b) B_y waveforms and error

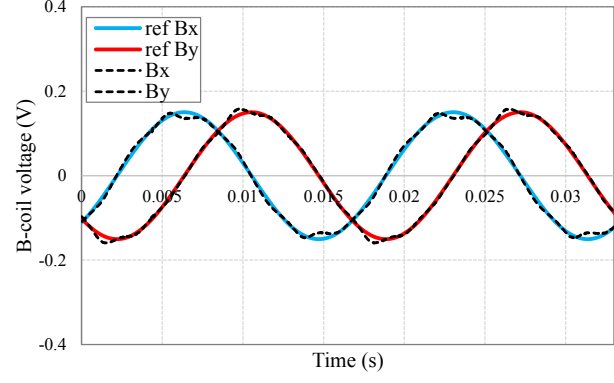
5.2.2.2 Experimental results

Figure 5-13 shows a comparison of the reference and sample B -coil sinusoidal voltages at high flux densities of 1.7 T and 1.9 T. The controller is able to follow the reference within the flux density voltage standard form factor of 1.11, even at high flux densities when the material is saturating. For lower flux densities, the controller reproduces the reference therefore only high flux density results are presented. When this voltage is integrated and multiplied by the coil constant, the resulting flux density waveform is a pure sinusoid.

Non-sinusoidal waveforms were also tested, 3rd and 5th harmonics of 20% in both phases. Figure 5-14 shows the experimental results for peak flux densities of 1.2 T for the 3rd harmonic, and 1 T for the 5th harmonic. The results show that the output waveform can be controlled within an error of less than 2%. It is possible to achieve better accuracy by appropriately tuning the proportional and integral gains. Future work in this aspect of control would focus on adaptive tuning of the control PI gains or changing the type of controller.

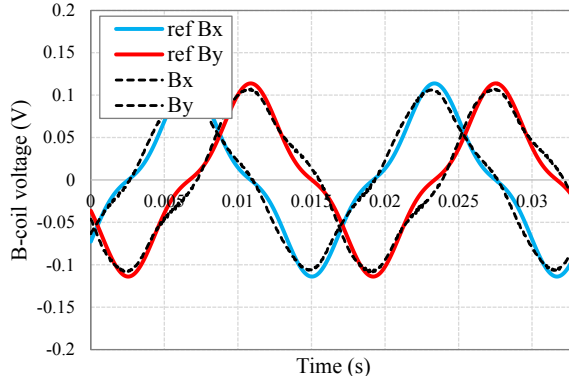


(a)

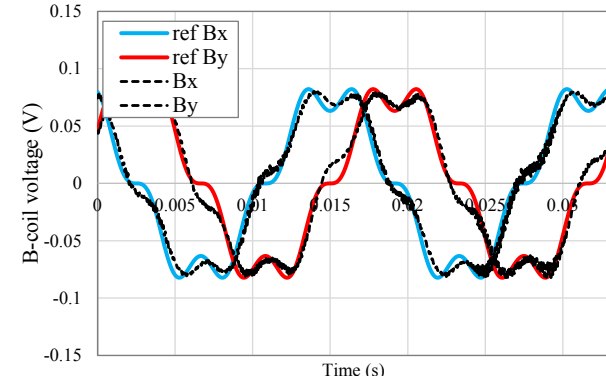


(b)

Figure 5-13: Comparison of the sinusoidal reference and measured B-coil voltages for different flux densities ; (a) at 1.7 T, (b) at 1.9 T



(a)



(b)

Figure 5-14: Comparison of the non-sinusoidal reference and measured B-coil voltages for different flux densities ; (a) at 1.2 T, (b) at 1 T

5.3 Summary

In this chapter, a method to estimate core losses in the stator of a hydro generator was presented, which was done assuming sinusoidal flux density waveforms. This was applied to calculate and compare the core losses in the stator of the machine at no load and full load. A 50% increase in the core loss was obtained from the no load to the full load operation. Including the rotational component increased the losses by 11% from only considering the pulsating loss. This method was also applied to other machine designs which validated the results in section 3.4, emphasizing that the distribution of rotational flux and losses is geometry dependent.

The loss estimation method was also extended to include non-sinusoidal flux that exists in machine. The non-sinusoidal waveforms used were FEA flux density waveforms from the back of the stator tooth. This was done using the measured rotational and pulsating core loss data, where the pulsating data was used to account for the non-sinusoidal component. Pulsating data was used for lack of measured non-sinusoidal flux density rotational data. As a result, a feedback controller was designed and implemented to measure rotational losses with non-sinusoidal flux density.

The controller sufficiently reproduced the sinusoidal waveforms at high flux density, and non-sinusoidal waveforms. More work can be done to tune the PI to increase the accuracy of the measurements.

Chapter 6 : Generator Winding Pattern Design

FEA modeling accords the ability to analyze different machine phenomena, predict machine behavior and understand machine response in certain operating conditions. This chapter discusses the analysis of a generator winding pattern for refurbishment purposes.

6.1 Generator winding refurbishment

Generators which have been online for over 20 years often require upgrades in the form of uprating or refurbishment. Both types of upgrades require changing one or more aspects of the machine such as, changing the stator core to a higher permeability lower loss material, reinsulating the rotor windings, rewinding of the stator, changing the stator frame and/or rotor rim, increasing the turbine rating, increasing the operating temperature, replacement of the exciter system, increasing the exciter current among others. The main objectives of the upgrades are to increase the life time, reduce maintenance or increase the rating of the machine.

Uprating is defined as when machine components are replaced or improved specifically to increase the generator power output without compromising the machine life time. In [102] a comprehensive methodology for hydro generator uprating was presented starting from the assessment of the unit's condition. Refurbishment is defined as the modernization of the generator by replacing parts or sections of the machine with better materials or designs, resulting to higher efficiency, increased life expectancy, reduced labor intensive maintenance and sometimes an increase in the machine output [103].

In [104], changing the rotor winding increased the power output by 10%, and in [105] stray losses were controlled by stator coil transposition to reduce circulating currents and the use of non-magnetic wedges. Some changes in the machine are also to reduce noise, vibration and overheating which can have diverse effects on the machine operation and performance. However before any changes are made, multi physics and economic analyses are required to determine the feasibility of the proposed solution.

Evaluation of design changes initially start with analytical models, which are followed by more detailed numerical simulations to the extent at which a phenomenon can be modeled. Analytical approaches have been used in large synchronous machines to predict air gap flux density [106] and open circuit voltage [107], armature and damper bar MMF harmonics in [108] and [109], all with acceptable accuracy. Analytical methods however are still deficient in prediction because they use several assumptions for simplicity, some characteristics like the effect of material saturation, eddy currents and some machine dimensions are ignored, all of which significantly affect the outcome.

Common updates and refurbishments are done on stator windings, which are replaced with better insulated coils and stranded conductors to reduce eddy currents, or with windings designed to reduce copper losses and harmonics [110]. In the refurbishment of a 32.5 MVA hydro generator, the stator core design was maintained and a new winding pattern was proposed. For any fractional slot windings with $a\frac{b}{c}$ slots per pole per phase, several balanced winding patterns exist provided both b and $(c-b)$ are greater than one [111]. The final choice for a winding pattern is then based on the winding pattern with the least noise and vibration.

This section therefore numerically analyses, the influence of changing the stator winding pattern by comparing the air gap flux density space harmonics, and the air gap electromagnetic forces in both the new and old winding patterns. Emphasis is on the low frequency harmonics around the natural frequencies of the machine. The generator modeling and validation procedure used is the same as discussed in Chapter 2, therefore the modeling and validation details are not repeated in this chapter. A recommendation of the winding pattern is given based on the results from the numerical analysis.

6.2 Generator modelling and validation

Machine 2 with specifications repeated in Table 6-1 was modelled in 2D FEA. The slots per pole per phase for this machine is $2\frac{2}{17}$, therefore a minimum of 17 poles is required to model this machine according to its magnetic and winding symmetry, which reduces the model to

quarter of the machine. This was done by applying the appropriate master and slave boundary conditions on the edges of the model.

Nonlinear transient, time stepped simulations with a time step of 36 μ s was selected for the simulations using a fine model mesh totaling to 275945 elements. External circuits were used to impose a load on the machine, include per phase end winding impedances and per pole equivalent damper bar impedances. Comparison of the effect of changing winding patterns is only effective in the loaded condition, therefore all simulations are executed in the loaded condition based on the available measured data. Due to the turbine limitations, the only available measured data is at no load and 86% of the rated load. Thus, all the simulations were limited to these two operating conditions.

Figure 6-1 shows the simulated 2D model, flux density distribution and flux lines at 86% of the rated load, which indicates a large percentage of the stator yoke has flux density less than 0.4 T. This FEA machine model was validated using measured air gap flux data at both no load and 86% of the rated load as shown Figure 6-2. Comparison of the simulated and measured air gap flux density showed good agreement at both operating points, therefore validating the FEA model.

Table 6-1 Machine specifications

Power	32.5 MVA
Voltage	13.2 kV
Power factor	0.8
Rated current	1.422 kA
Speed	105.9 rpm
Number of poles	68
Number of slots	432

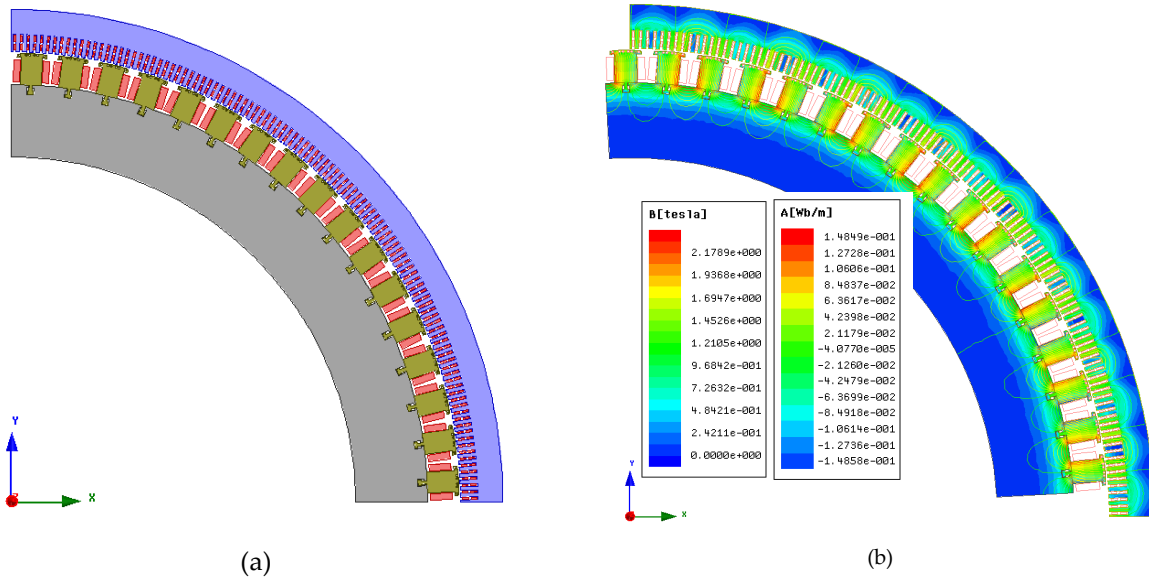


Figure 6-1: Simulated machine at 86% rated load; (a) 2D FEA model, (b) Flux density distribution and flux lines.

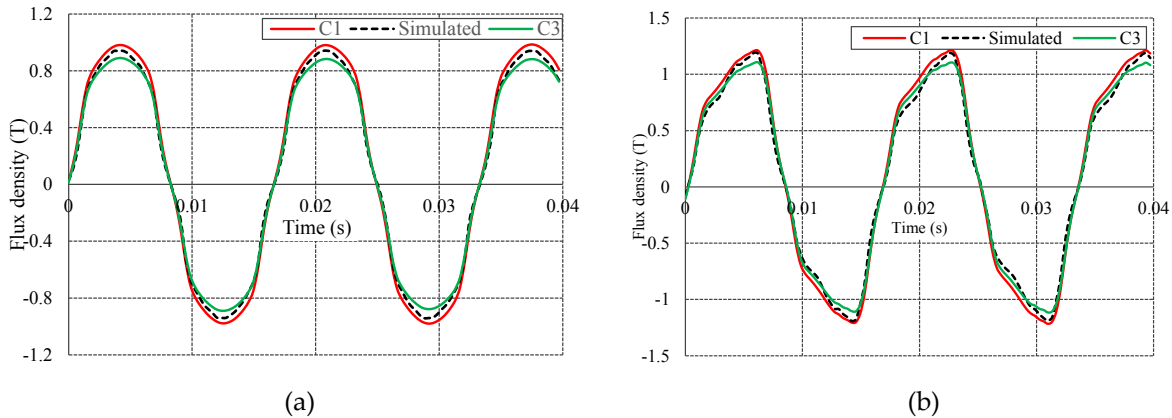


Figure 6-2: Comparison of the measured and simulated air gap flux density at (a) no load and (b) 86% of rated load

6.3 Change in pattern winding

The old winding pattern of this 32.5 MVA generator is as shown in Figure 6-3 (a). For refurbishment, the refurbishing company recommended the new winding pattern shown in Figure 6-3 (b), based on their in house winding standard. Changing the winding pattern offers many advantages but also has the potential to increase the noise and vibration in the machine. As a result, it was of interest to the utility to know the machine performance with the new winding pattern.

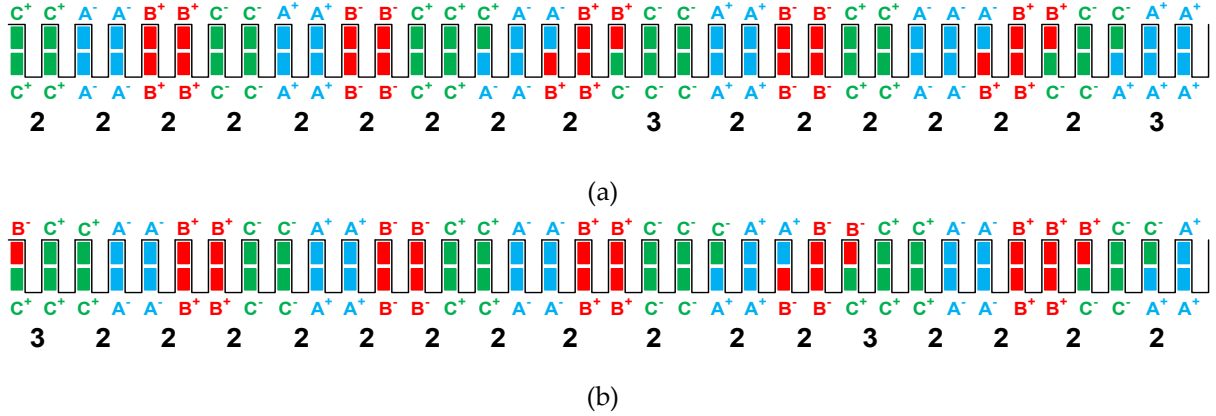


Figure 6-3: Machine stator winding patterns; (a) Old winding pattern (b) New winding pattern

This section therefore compares the machine performance with the two winding patterns, specifically the air gap flux and electromagnetic forces in the air gap. Emphasis is on the low frequency harmonics around the natural frequencies of the machine core, which are the source of noise and vibration in the machine.

6.3.1 Natural frequency of the core

In normal machine operation, exciting the natural frequencies causes acoustic noise and vibrations. The natural frequency of the machine can be calculated either analytically or numerically. In the analytical approach presented in [112], only the stator core is considered in the natural frequency calculation, the stator frame and end windings of the machine are not included. Conversely, determining natural frequencies numerically can include the stator, and the effect of both the stator frame and stator core. Including more components in the natural frequency calculations yields higher natural frequencies.

In [113] analytically and numerically computed natural frequencies and mode shapes of a 120 MVA hydro generator were concurrent. Using the same numerical approach, Figure 6-4 shows the numerically calculated natural frequencies of the 32 MVA machine core with their corresponding mode shapes. The frequencies increase if the natural frequency is recalculated considering the generator frame.

For this machine, the slots per pole per phase is $2\frac{2}{17}$ which means the magnetic symmetry repeats after 17 poles, therefore the mode for this machine is $\frac{68}{17} = 4$. From Figure 6-4, mode 4

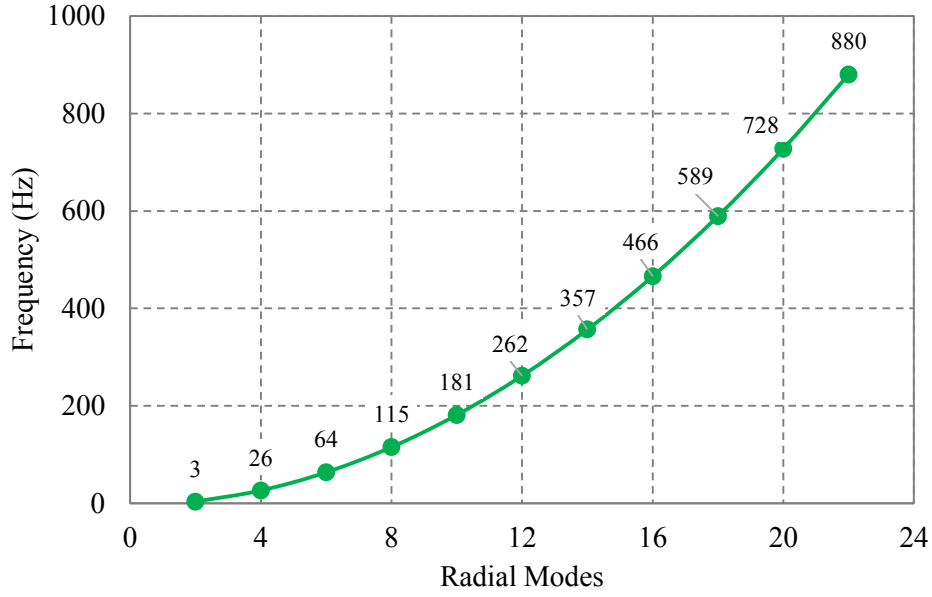


Figure 6-4: Natural frequency of the machine core

corresponds to a natural frequency of 26 Hz and the other probable modes are 4-10 with natural frequencies in the range less than 200 Hz. Thus, in the change in winding pattern analysis, focus is on harmonics in the frequency range less than 200 Hz, with magnitudes greater than 1%.

6.3.2 Armature MMF

The armature MMF of the hydro generator can be determined analytically or graphically [114]. Analytically involves calculating the MMF as a sum of all three phases using equation (6.1) from [115]

$$\theta = i_a \sum_{n=1,3,5,\dots}^{\infty} \hat{M}_n \sin(np\alpha) + i_b \sum_{n=1,3,5,\dots}^{\infty} \hat{M}_n \sin\left(np\alpha - \frac{2\pi n}{3}\right) + i_c \sum_{n=1,3,5,\dots}^{\infty} \hat{M}_n \sin\left(np\alpha - \frac{4\pi n}{3}\right) \quad 6.1$$

$$i_a = I \cos(\omega t), \quad i_b = I \cos\left(\omega t - \frac{2\pi}{3}\right), \quad i_c = I \cos\left(\omega t - \frac{4\pi}{3}\right),$$

$$\hat{M}_n = \frac{4}{\pi} \frac{N_s}{2pn} \frac{1}{n} k_{dn}(n) k_{pn}(n) k_{sn}(n),$$

where θ is the armature MMF, p is the number of pole pairs, n the harmonic order, α is angle in mechanical degrees, N_s is the number of turns per slot, k_d is the distribution factor, k_p is the pitch

factor and k_s is the slot skewing factor. Figure 6-5 shows the analytically calculated MMFs using both winding patterns normalized to the old pattern winding fundamental of 9642 AT.

The magnitude of the fundamental component and the slot passing frequency in both windings was similar as expected. This is because the number of slots per pole per phase is unchanged. The slot passing frequency of 762.35 Hz was calculated using equation (6.2)

$$f_{spf_n} = f \left(\frac{n\Lambda}{p} \pm 1 \right) \quad 6.2$$

where f_{spf_n} is slot passing frequency for any n^{th} harmonic, f is the fundamental frequency, n is the harmonic order, N_{slot} is the number of stator slots, p is the number of pole pairs. However, the harmonics of the new pattern winding were higher than the old pattern winding especially at 21.18 Hz in both the clockwise and counter clockwise direction, each are twice that of the old pattern winding. This difference is significant especially at this frequency, which is close to the mode 4 natural frequency of the machine.

At 44.21 Hz, the old pattern winding harmonic rotating in the counterclockwise direction is 9.6% and the new pattern winding is 2.8% of the fundamental. This 44.21 Hz frequency is close

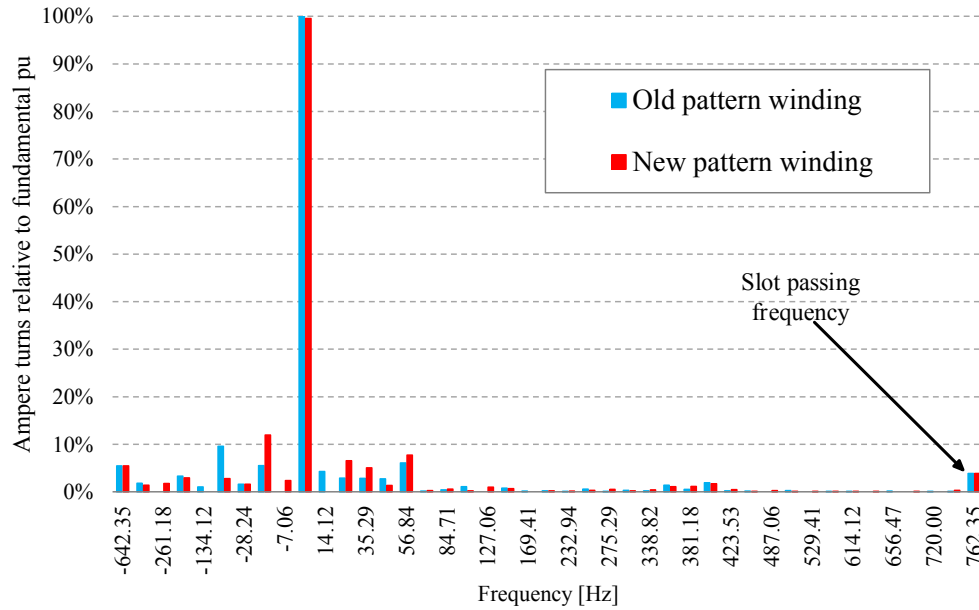


Figure 6-5: Comparison of the analytically calculated stator winding MMFs of the old and new pattern winding

to the mode 6 natural frequency of the machine. However, because this is a mode 4 machine, reducing the 21.18 Hz component is priority, an advantage the old pattern winding seems to offer.

Although the analytically generated MMF gives some of the dominant harmonics, the influence of the slot width, the direction and magnitude of current flow in each slot per phase, on the winding pattern is not considered. In this case, the graphical method which accounts for them presents an advantage over the analytical method [114]. The graphical method however can be laborious for large diameter machines with many slots per phase.

Furthermore, it is difficult to isolate the armature MMF in numerical simulations when the machine is operated as a generator. Nonetheless, the numerically obtained air gap flux density at a point and in space carries information on all the available harmonics. Therefore numerical analysis will be done on the air gap flux at 86% rated load.

6.3.3 Air gap flux density

The air gap flux density of both pattern windings at 86% rated load is shown in Figure 6-6, where Figure 6-6 (a) is the air gap flux at a point, with its FFT in Figure 6-6 (b) and the radial air gap flux is shown in Figure 6-6 (c). All FFT values are normalized to the old pattern winding fundamental peak of 1.134 T. The new pattern winding has a fundamental magnitude of 102%, and at the 3rd harmonic of 180 Hz, its magnitude is 12% while that of the old pattern winding is 14% of the fundamental. Other harmonics are negligible and are also of the same magnitude in the two winding patterns.

For the same time step, the air gap flux density along an arc in the air gap for both winding patterns was obtained at 86% of rated load as shown in Figure 6-6 (c) for a section of the air gap arc. The radial flux distribution is not significantly different between the two winding patterns, except in some teeth where either the old pattern winding or the new pattern winding has higher flux.

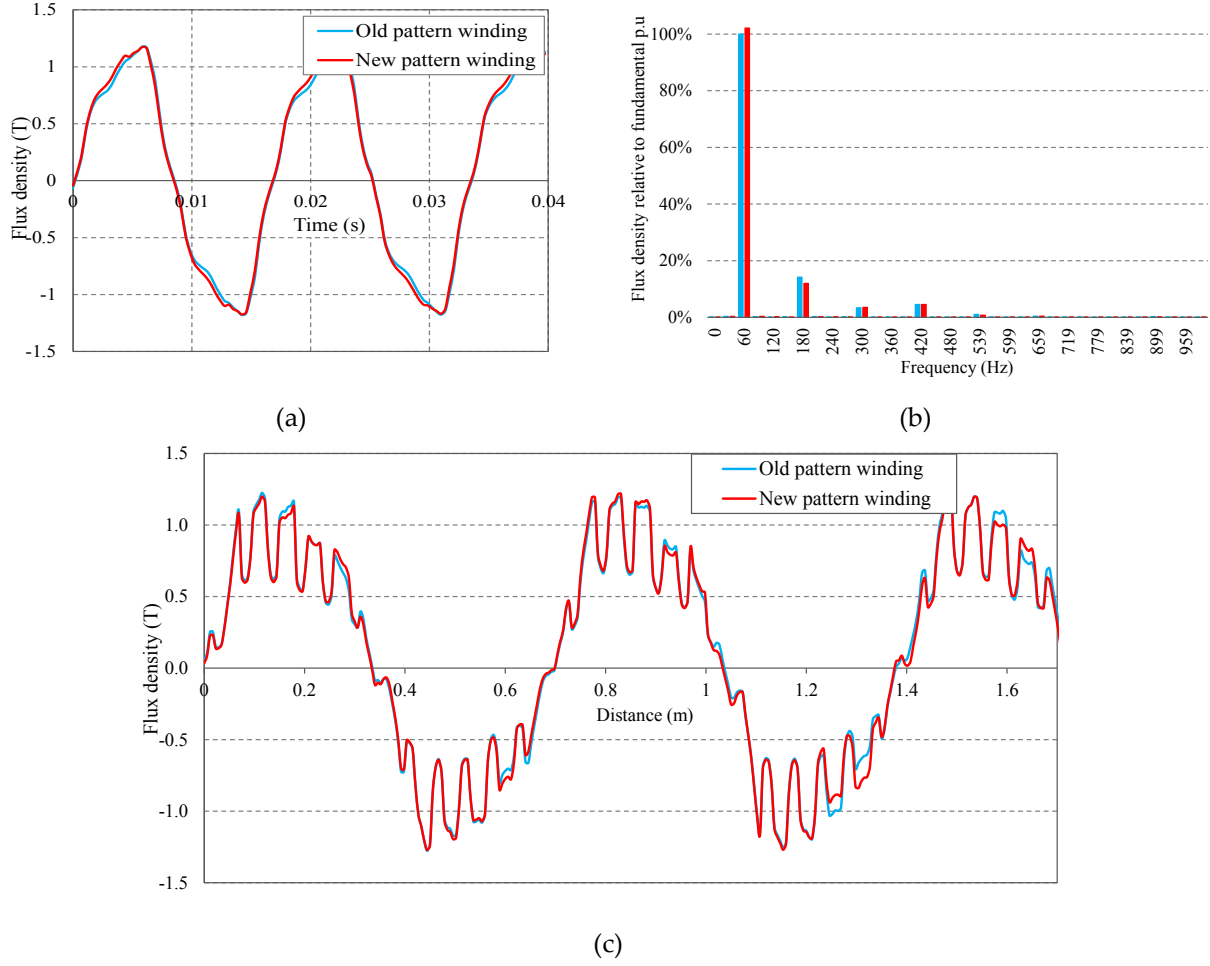


Figure 6-6: Comparison of the air gap flux density in both pattern windings; (a) At a point, (b) FFT of the air gap flux density at a point, (c) Radial air gap flux density

6.3.4 Electromagnetic forces

The force density was obtained from the radial and tangential air gap flux profile along the same arc in the airgap, which gives the force density profile as a function of distance. Maxwell stress tensor equations (6.3) were used to calculate the radial and tangential forces respectively

$$f_r = \frac{1}{2\mu_0} (B_r^2 - B_t^2)$$

$$f_t = \frac{1}{\mu_0} B_r B_t$$
6.3

where f_r and f_t are the radial and tangential force density components, B_r and B_t are the radial and tangential flux density, and μ_0 is the permeability of free space.

Figure 6-7 shows the radial force density along the air gap arc, and its FFT for select frequencies. The p.u force density for both windings was obtained by considering the fundamental at $2f = 120$ Hz and using the old pattern winding value of 186 kN/m^2 as the base value. Generally, for frequencies less than $2f$, the new pattern winding had higher harmonic magnitudes. At some frequencies such as 21.18, 42.35, 49.42, 70.6, 98.84 and 141 Hz, the new pattern winding harmonic magnitudes were over twice that of the old pattern. In comparison with the analytically obtained harmonic spectrum, at 21.18, 35.29 and 56.84 Hz the new winding

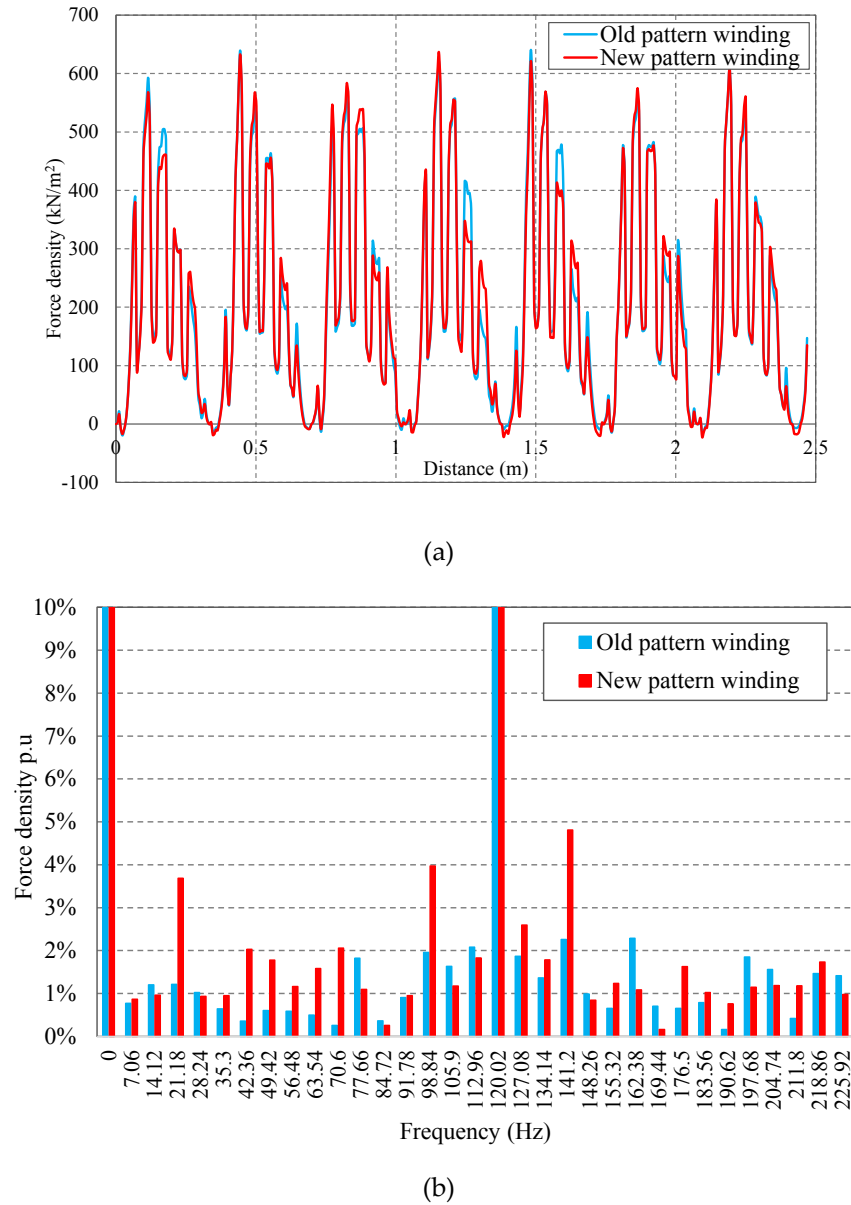


Figure 6-7: Comparison of the air gap electromagnetic force densities in new and old pattern winding; (a) Force densities along an air gap arc, (b) Force density FFT in pu

pattern magnitudes were also higher than the old pattern winding, while at 14.12 and 44.21 Hz, the old pattern winding dominates. This shows consistency between the simulated and analytical results.

At 42.35 Hz the simulated force density results show a higher harmonic magnitude for the new winding, while the analytical results (armature MMF) for the same frequency have the old pattern winding harmonic magnitudes higher. The presence of the same frequency spectrum in both the simulated and analytically calculated quantities indicate the correlation of the results, while their differences in harmonic content can be attributed to the air gap flux density having more effects like armature reaction, material effects and geometry that are not generally considered in the analytical armature MMF calculations.

6.3.5 Losses

The total harmonic distortion (THD) of the armature MMF in Figure 6-5 resulted into 16.6% for the old pattern winding and 10.0% for the new pattern winding. A THD of the radial force density of Figure 6-7 up to 4 kHz yielded 94% for the old pattern winding and 97% for the new pattern winding. Both THDs indicate the harmonic spectrum to be higher in the new pattern winding by 3%. These armature MMF harmonics are induced damper bar currents and also contribute to non-sinusoidal flux in the stator and pole face, which results in an increase in the associated core losses and the total damper bar ohmic losses.

The solid losses P_{ohm} in the damper bars, which is representative of the resistive loss in the damper bars, were calculated from the field solutions using equation (6.4)

$$F_{ohm} = \frac{1}{\sigma} \int_{Vol} J^2 dVol \quad 6.4$$

where J is the current density, σ is the conductivity in siemens/meter. The total core losses P_v were calculated using equation (6.5) as a sum of the rotor pole face losses and stator core losses, calculated as an average over 6 electrical cycles.

$$F_v = K_h f B_m^2 + K_c (f B_m)^2 + K_e f B_m^{1.5} \quad 6.5$$

where B_m is the peak flux density, f is the frequency, K_h is the hysteresis coefficient, K_c is the eddy current coefficient and K_e is the excess loss coefficient.

Table 6-2 shows a comparison of the losses in both winding patterns. Results show the new winding pattern has higher losses compared to the old winding, this agrees with the higher harmonic content found in the new pattern winding. The numerical core losses increase by 6.7% and the total damper bar losses increase by 5.3% in the new winding pattern.

Table 6-2 Loss comparison

Loss	Old pattern winding	New pattern winding
Core losses (kW)	239.6	255.7
Damper bar losses (kW)	26.1	27.5

6.3.6 Conclusion

A suitable choice of winding pattern is based on the pattern with the least level of noise and vibration. From numerical analysis, this is visible in the presence of subharmonics and low frequency harmonics with values greater than 1% of the fundamental. Moreover, the existence of harmonics around the natural frequency of the machine core should be avoided.

The simulated airgap flux density for both winding patterns are very similar, however the new winding pattern has higher harmonic components in the calculated radial electromagnetic forces, which could significantly increase noise and vibration.

Changing the winding pattern is therefore a tradeoff between the benefits of the refurbishment and other different factors for instance; vibration and noise, associated core and damper bar losses, downtime and cost associated with changing the winding pattern. In this case the old pattern seems to present better properties than the proposed new pattern. However this conclusion is only from numeric electromagnetic simulations, results could be different if all

mechanical aspects are put into consideration. When the refurbishment is complete, experimental results will be analyzed to ascertain the machine performance.

6.4 Summary

Numerical evaluation of changing the winding pattern for a 32.5MVA generator was presented. Comparison of the two winding patterns was done using the analytically calculated armature MMF, numerically obtained air gap flux density both at a point and in space, and the associated radial force densities in the air gap. Analytical results showed some significant low frequency harmonics (21.18 and 44.2 Hz), which were also present in the numerical air gap results but with less significant values.

Comparison of the armature MMF and the radial force THD for both winding patterns showed an increase of 3% in the new pattern winding. This indicates more harmonic content in the new pattern winding compared to the previous one. As a result, there will be higher associated losses in the core and rotor damper bars.

Chapter 7: Conclusions and Future work

7.1 Conclusions

This work presented several aspects in rotational core losses of hydro generators from which the following conclusions can be drawn;

1. A review of core loss measurement and estimation methods in chapter 1 showed that methods to estimate core losses in real machines require the rotational core loss component to be accounted for. Accurate estimation of core losses in hydro generators finds applications in machine uprate studies, loss distribution and hot spot determination in the machine. This work therefore proposes a method to estimate core losses in hydro generators including the rotational core loss component.
2. FEA modeling and simulation of hydro generators requires several test data to validate the model before it is used for any analysis. Measured data provides a reference for numerical models even in the case of different machines with the same machine design. As shown in chapter 2, variation in machine performance of several units with the same design due to physical characteristics and tolerances such as effective air gap and material permeability, can be pinpointed using FEA simulations and open circuit curve data.
3. The distribution of rotational flux in the stator of hydro generators is dependent on the design dimensions and the machine's operating point on the BH curve. Simulation results in chapter 3 showed that machines with a larger yoke, smaller air gap, and machines operated close to saturation are prone to higher percentages of rotational flux.
4. The shape of a rotational core loss measurement yoke affects the uniform distribution of flux in the sample. Proper choice of the type of magnetizer, magnetizer yoke depth, sample diameter, winding pattern and number of slots for uniform flux density and field

intensity distribution across the sample is crucial. Moreover, these also limit the available measurement area. An optimum design should provide uniformity in all field quantities at all field levels and magnetization directions.

5. Core loss estimation including both the rotational and non-sinusoidal components is possible with the available measured rotational data. The post processing technique based on curve fitted measured data, provides an easier, less computation intensive and straightforward technique to compute core losses in each mesh element of the machine. The method in chapter 5 can be scripted and run in the background of a simulation software to calculate core losses.
6. Flux density waveform control in core loss measurements can be achieved using the control architecture in electrical machines and drives. A feedback loop in the DQ frame using a PI controller was used to control the flux density waveform at high flux densities. Moreover, the controller could also be used for non-sinusoidal waveforms with 20% 3rd and 5th harmonics.
7. Change in a generator pattern winding for the same stator core design can lead to an increase in the air gap electromagnetic forces. The presence of low frequency harmonics around the machine radial mode can lead to noise and vibration. Therefore, for the available pattern windings of any core stator design, preliminary analysis is required to ensure the winding pattern of choice is unsusceptible to noise and vibration.
8. Interlaminar faults distort the measured magnetic field. The increased eddy currents in the presence of the fault distort the fields in the location of the fault. This resulted in the distortion of the measured magnetic field intensity waveforms in both the clockwise and counter clockwise flux rotation directions. This finding can further be developed into a lamination fault detection tool.

7.2 Future work

The future work can be summarized as follows;

1. Develop a metric that can be used to determine the percentage of rotational flux in any machine design based on certain relative dimensions such as the ratio between the tooth length and yoke depth, the tooth width and air gap length among others.
2. Develop a database of measured rotational core loss data for several magnetic materials used in hydro generators, from which rotational core losses in the entire machine can be calculated. This database can be included in machine design software for more accurate core loss prediction.
3. Quantification and inclusion of the miscellaneous losses existing in the no load measured core loss, which are not accounted for in the calculated losses. These losses include rotor surface losses, eddy current losses in damper bars and slot leakage flux. Accounting for these losses allows the fair comparison of measured and calculated machine core losses.
4. Script the proposed core loss calculation method in a programming language such as python or vbs to be run in the simulation software (ANSYS – Maxwell) during simulation. This would reduce on the manual post processing required to estimate core losses including the rotational component.
5. Upgrade the controller to an adaptive controller capable of self-tuning especially when the material starts to saturate. Manually tuning the PI is tedious and subject to human error.
6. Developing a tool to detect interlamination faults from the measured field intensity on the lamination surface. Simulated and measured field results showed a visible difference between the no fault and faulted laminations.

REFERENCES

- [1] Canadian Electricity Association, "FACT SHEETS - Key Canadian Electricity Statistics," June 2014. [Online]. Available: www.electricity.ca/resources/industry-data.php. [Accessed 17 March 2015].
- [2] "Hydro-Quebec at a Glance," Hydro-Quebec, [Online]. Available: <http://www.hydroquebec.com/about/who-are-we/hydro-quebec-glance.html>. [Accessed 11 June 2016].
- [3] M. G. Johnson, "Recent generator uprate case studies," in *International Conference of Electric Machines and Drives (IEMDC)*, Seattle, 1999.
- [4] R. Zawoysky and K. Tornroos, "GE Generator rotor design, operational issues, and refurbishment options," GE Power Systems, Schenectady, NY, 2001.
- [5] IEC, 60064-2A, *Rotating electrical machines - Part 2-1: Standard methods for determining losses and efficiency from tests (excluding machines for traction vehicles)*, 2014.
- [6] Std. 115 - 2009, *IEEE Guide for Test Procedures for Synchronous Machines Part I Acceptance and Performance Testing Part II Test Procedures and Parameter Determination for Dynamic Analysis*, IEEE, 2009.
- [7] A. Moses, "Importance of rotational losses in rotating machines and transformers," *Journal of Materials Engineering and Performance*, vol. 1, no. 2, pp. 235-244, 1992.
- [8] D. Ahmad, "Evaluation of localised loss transformer core lamination," *Journal of applied sciences*, vol. 10, no. 22, pp. 2917-2922, 2010.
- [9] M. Znidarich, "Hydro generator stator cores part 1- constructional features and core losses," in *Australasian Universities Power Engineering Conference AUPEC*, Sydney, 2008.

- [10] ASTM Standard A348/A348M-00, "Standard Test method for Alternating Current magnetic properties of materials Using the Wattmeter-Ammeter-Voltmeter Method, 100 to 10 000Hz and 25-cm Epstein Frame," West Conshohocken, PA, 2000.
- [11] "MODEL 3110-MS2 COMPUTER," Donart Electronics Inc, 1999-2010. [Online]. Available: <http://www.donartelectronics.com/ms2.html>. [Accessed 21 5 2012].
- [12] M. Ibrahim and P. Pillay, "Novel equipment for the measurement of core losses in laminations for advanced machines," in *IEEE international electric machines and drives conference (IEMDC)*, Niagara falls, 2011.
- [13] P. Marketos, S. Zurek and A. Moses, "A method for defining the mean path length of the Epstein frame," *IEEE Transactions on magnetics*, vol. 43, no. 6, 2007.
- [14] A. S. A927/A927M-99, "Standard test method for alternating current magnetic properties of Toroidal core specimens using the voltmeter-ammeter-wattmeter method," ASTM Standard A927/A927M-99, West Conshohocken, PA, 1999.
- [15] T. Yamamoto and Y. Ohya, "Single Sheet Tester for Measuring Core Losses and Permeabilities in a Silicon Steel Sheet," *IEEE Transactions on Magnetism*, vol. 10, no. 2, pp. 157-159, 1974.
- [16] Y. Guo, J. Zhu, J. Zhong, H. Lu and J. Jin, "Measurement and modeling of rotational core losses of soft magnetic materials used in electrical machines: A review," *IEEE Transactions on Magnetism*, vol. 44, no. 2, 2008.
- [17] J. Sievert, "Two-dimensional magnetic measurements - History and achievements of the workshop," *Journal of Electrical Review*, vol. 87, pp. 1-10, 2011.

- [18] C. Ragusa, S. Zurek, C. Appino and A. Moses, "An Intercomparison of Rotational Loss Measurements in Non-Oriented Fe-Si Alloys," *J. Magn. Magn. Mater.*, vol. 320, no. 20, pp. e623-e626, October 2004.
- [19] A. Hasenzagl, B. Weiser and H. Pfutzner, "Novel 3-phase excited single sheet tester for rotational magnetization," *Elsevier Journal of Magnetism and Magnetic Materials*, vol. 160, pp. 180-182, 1996.
- [20] F. Brailsford, "Rotational Hysteresis Loss in Electrical Sheet Steels," *J. of the Inst. of Elect. Eng.*, vol. 83, no. 502, pp. 566-575, October 1938.
- [21] F. Fiorillo and A. Rietto, "Extended induction range analysis of rotational losses in soft magnetic materials," *IEEE transactions on magnetics*, vol. 24, no. 2, 1988.
- [22] C. Boon and J. Thompson, "Alternating and rotational power loss at 50c/s in 3% silicon - iron sheets," *The institution of electrical engineers proceedings: science and general*, vol. 112, no. 11, 1965.
- [23] A. Bousbaine, "A thermometric approach to the determination of iron losses in single phase induction motors," *IEEE Transactions on energy conversion*, vol. 14, no. 3, 1999.
- [24] A. J. Gilbert, "A method of measuring loss distribution in electrical machines," *Proceedings of the IEE-Part A: Power Engineering*, vol. 108, no. 39, pp. 239-244, 1961.
- [25] M. Ross, "Time-temperature tests to determine machine losses," *Electrical Engineering*, vol. 54, no. 5, pp. 512-515.
- [26] H. Hamzehbahmani, A. Moses and F. Anayi, "Opportunities and precautions in measurement of power loss in electrical steel laminations using the initial rate of rise of temperature method," *IEEE Transactions on magnetics*, vol. 49, no. 3, 2013.

- [27] J. Sievert, H. Ahlers, M. Birkfeld, B. Cornut, F. Fiorillo, K. Hempel, T. Kochman, A. Kedous-Lebouc, T. Meydan, A. Moses and A. Rietto, "European intercomparison of measurements of rotational power loss in electrical sheet steel," *Journal of Magnetism and Magnetic Materials*, vol. 160, pp. 115-118, 1996.
- [28] J. Wanjiku and P. Pillay, "Design Considerations of 2-D Magnetizers for High Flux Density Measurements," *IEEE Transactions on Industry Applications*, pp. 3629-3638, 2015.
- [29] N. Alatawneh and P. Pillay, "Design of a novel test fixture to measure rotational core losses in machine laminations," *IEEE Industry Applications*, vol. 48, no. 5, pp. 1467-1477, 2012.
- [30] C. Steinmetz, "On the law of hysteresis (originally published in 1892)," *Proc. IEEE*, vol. 72, no. 2, pp. 196-221, 1984.
- [31] G. Bertotti, "General properties of power losses in soft ferromagnetic materials," *IEEE Trans. Magnetics*, vol. 24, no. 1, pp. 621-630, 1988.
- [32] L. Mthombeni and P. Pillay, "Core losses in motor laminations exposed to high frequency or non-sinusoidal excitation.," *IEEE Trans. Ind.App*, vol. 40, no. 5, pp. 1325-1332, 2004.
- [33] Y. Chen and P. Pillay, "An Improved Formula for Lamination Core loss Calculations in Machines Operating with High Frequency and High Flux Density Excitation," in *IEEE 37th IAS Annunal Meeting Conference*, Pittsburgh, 2002.
- [34] A. Boglietti and A. Cavagnino, "Iron loss prediction with PWM supply: An overview of proposed methods from an engineering application point of view," in *Industry Applications Conference*, New Orleans, 2007.
- [35] Z. Gmyrek, A. Boglietti and A. Cavagnino, "Estimation and analysis if iron losses in induction motors under sinusoidal and PWM excitation," in *IEEE International conference on electrical machines*, Vilamoura, 2008.

- [36] D. Lonel, M. Popescu, S. Dellinger, T. E. Miller, R. Heidman and M. McGilp, "Computation of Core losses in electrical machines using improved models for laminated steel.," *IEEE Trans. Ind. Appl.*, vol. 43, no. 6, Nov/Dec 2007.
- [37] J. Lavers, P. Biringer and H. Hollitscher, "A simple method of estimating the minor loop hysteresis loss in thin laminations.," *IEEE Trans. on magnetics*, vol. 14, no. 5, 1978.
- [38] E. Dlala, J. Saitz and A. Arkkio, "Hysteresis modeling based on symmetric minor loops," *IEEE Transactions on magnetics*, vol. 41, no. 8, 2005.
- [39] D. Eggers, S. Steentjes and K. Hameyer, "Advanced iron-loss estimation for nonlinear material behaviour," *IEEE Transactions on magnetics*, vol. 48, no. 11, November 2012.
- [40] D. Lin, P. Zhou, W. Fu, Z. Badics and Z. Cendes, "A dynamic core loss model for soft ferromagnetic and power ferrite materials in transient finite element analysis," *IEEE Transactions on Magnetism*, vol. 40, no. 2, March 2004.
- [41] L. Ma, M. Sanada, S. Morimoto and Y. Takeda, "Prediction of iron loss in rotating machines with rotational loss included," *IEEE Transactions on magnetics*, vol. 39, no. 4, 2003.
- [42] K. Komeza and M. Deme, "Field and circuit calculation of the core losses in the energy-saving small-size induction motor," in *International Conference on Electrical Machines*, Rome, 2010.
- [43] A. Belahcen, P. Rasilo and A. Arkkio, "Segregation of iron losses from rotational field measurements and application to electrical machine," *IEEE Transactions on magnetics*, vol. 50, no. 2, 2014.
- [44] M. Ranlof, A. Wolfbrandt, J. Lidenholm and U. Lundin, "Core loss prediction in large hydro generators: influence of rotational fields," *IEEE Transactions on magnetics*, vol. 45, August 2009.

- [45] I. Junaid, J. Qudsia and B.-i. Kwon, "Improved model of the iron loss for the permanent magnet synchronous motors," in *International Conference on Electrical Machines and Systems*, Rome, 2010.
- [46] T. Fukami, H. Aoki and K. Shima, "Assessment of core losses in a flux-modulating synchronous machine," *IEEE Transactions on industry applications*, vol. 48, no. 2, March/April 2012.
- [47] X. Jannot, J. Vannier, A. Kedous-Lebouc, C. Marchand, M. Gabsi and J. Saint-Michel, "Analytical computation of stator iron losses in interior permanent-magnet synchronous machine," in *XIX International Conference on Electrical Machines*, Rome, 2010.
- [48] J. Tangudu, T. Jahns and A. EL-Refaie, "Core loss prediction using magnetic circuit model for fractional slot concentrated winding interior permanent magnet machines".
- [49] J. Zhu and V. Ramsden, "Improved formulations for rotational core losses in rotating electrical machines," *IEEE Transactions on magnetics*, vol. 34, no. 4, July 1998.
- [50] J. Walker, *Large Synchronous Machines, Design, Manufacture and Operation*, New York: Oxford University Press, 1981.
- [51] P. A. Hargreaves, B. C. Mecrow and R. Hall, "Calculation of Iron Loss in Electrical Generators using Finite Element Analysis," in *International Electric Machines and Drives Conference (IEMDC)*, Niagara Falls, 2011.
- [52] J. Lorenz, "Electrical machine iron loss predictions- A unique engineering approach utilizing transient finite element methods- Part 1: Theory and calculation method," in *Electric Ship Technologies Symposium*, Arlington, 2013.

- [53] J. Lorenz, "Electrical machine iron loss predictions- a unique engineering approach utilizing transient finite element methods-part II application and validation," *IEEE Transactions on industrial applications*, vol. 50, no. 4, 2014.
- [54] G. Stone, I. Culbert, E. Boulter and H. Dhirani, "Core lamination insulation failure and repair," in *Electrical Insulation for Rotating Machines: Design, Evaluation, Aging, Testing and Repair*, Wiley-IEEE Press, 2014, p. 672.
- [55] B. Moore, "Include generators and exciters in your outage inspections," Power-Business and Technology for the Global Generation Industry Since 1882, 15 March 2006. [Online]. Available: <http://www.powermag.com/include-generators-and-exciters-in-your-outage-inspections/?pagenum=7>. [Accessed 11 July 2016].
- [56] J. Edmonds, A. Daneshpooy, S. Murray and R. A. Sire, "Turbo generator Stator Core Study," in *Symposium on Diagnostics for Electric Machines, Power Electronics and Drives*, Cracow, 2007.
- [57] P. Tavner and A. Anderson, "Core faults in large generators," *IEE Proceedings - Electric Power Applications*, vol. 152, no. 6, pp. 1427-1439, 2005.
- [58] G. Stone, I. Culbert, E. Boulter and H. Dhirani, *Electrical insulation for rotating machines: Design, Evaluation, Aging, Testing and Repair*, Wiley & Sons Inc., 2014.
- [59] M. Znidarich, "Hydro generator stator cores Part 2 - Core losses, degradation mechanisms, testing and specification," in *Australasian universities power engineering conference (AUPEC)*, 2008.
- [60] C.-G. Richter and J. R. Weidner, "Testing stator cores of turbo generators using the ring flux method," Siemens AG, Vienna, Austria, 2013.

- [61] H. Tomlinson, "Interlaminar insulation test for synchronous machine stators," *Power apparatus and systems*, vol. 71, no. 1, 1952.
- [62] J. Sutton, "Method and apparatus for testing laminated cores of electrical machines". Patent US 20030117144 A1, 26 June 2003.
- [63] J. Sutton, "EL CID: An Easier way to test stator cores," *Electrical Review*, vol. 207, pp. 33-37, 1980.
- [64] A. Smith, D. Bertenshaw, C. Ho and T. Chan, "Detection of stator core faults in large turbo-generators," in *Electric machines and drives conference (IEMDC)*, 2009.
- [65] S. Lee, G. Kilman, M. Shan, W. Mall, N. K. Nair and R. Mark, "An advanced technique for detecting inter-laminar stator core faults in large electric machines," *IEEE Transactions on industry applications*, vol. 41, no. 5, 2005.
- [66] R. Romary, S. Jelassi and J. Brudny, "Stator interlaminar fault detection using an external flux density sensor," *IEEE Transactions on industrial electronics*, vol. 57, no. 1, 2010.
- [67] S. Nazrulla, E. Strangas, J. Agapiou and T. A. Perry, "A device for the study of electrical steel losses in stator lamination stacks," *IEEE Transactions on industrial electronics*, vol. 61, no. 5, 2014.
- [68] G. B. Kliman, S. B. Lee, M. R. Shah, M. Lusted and N. K. Nair, "A new method for synchronous generator core quality evaluation," *IEEE Transactions on Energy Conversion*, vol. 19, no. 3, 2004.
- [69] R. Romary, C. Demian, P. Schlupp and J. Roger, "Offline and Online methods for stator core fault detection in large generators," *IEEE Transactions on Industrial Electronics*, vol. 60, no. 9, 2013.

- [70] B. Singh, E. Kyriakides and A. Michaelides, "Efficient identification of synchronous machine parameters through the finite element method," in *Mediterranean conference and exhibition on power generation, transmission, distribution and energy conversion*, Agia Napa, 2010.
- [71] M. Amaya, A. Costa, J. Palacios and H. Cadavid, "Identification of the synchronous machine parameters by the simulation of time domain tests using finite element method," in *IEEE International conference on electric machines and drives*, 2003.
- [72] P. Hargreaves, B. Mecrow and R. Hall, "Open circuit voltage distortion in salient pole synchronous generators with damper windings," in *International Conference on Power Electronics Machines and Drives (PEMD)*, Brighton, 2010.
- [73] K. Ship, K. Goddard and J. Sykulski, "Two dimensional finite-element simulation of high temperature superconducting synchronous generator during three-phase short circuit fault condition using full transient non-linear rotating machine model," in *International Symposium on Electromagnetic Fields in Electrical Engineering*, Maribor, 2003.
- [74] G. Komurgoz and T. Gundogdu, "Comparison of salient pole and permanent magnet synchronous machines designed for wind turbines," in *Power Electronics and Machines in Wind Applications (PEMWA)*, Denver, 2012.
- [75] R. Wamkeue, I. Kamwa and M. Chacha, "Line to line short circuit based finite element performance and parameter predictions of large generators," *IEEE Transactions on Energy Conversion*, vol. 18, no. 3, pp. 370-378, 2003.
- [76] L. Han, G. Zhou, Z. Fan, X. Hou and Y. Lian, "Optimization of no load voltage waveform in hydro-generator by asymmetric poles," in *World Automation Congress*, Hawaii, 2008.

- [77] Hind.C.Dirani, A. Merkhoul, A.-M. Giroux and K. A.-. Haddad, "Study of the impact of eccentricity in large synchronous generator with finite elements," in *Interenational Conference on Electrical Machines*, Berlin, 2014.
- [78] B. Lamamura, Y. L. Menach, A. Tounzi, N. Sadowski and E. Guillot, "Study of static and dynamic eccentricities of a synchronous generator using 3D FEM," *IEEE Transactions on Magnetics*, vol. 46, no. 8, pp. 3516-3519, 2010.
- [79] K. Weeber, "Determination of dynamic parameters of large hydro-generators by fininte-element simulation of three-phase sudden short-circuit tests," in *IEEE Internation Electric Machines and Drives Conference*, Milwaukee, 1997.
- [80] C. Hudon, A. Merkhoul and M. Chaaban, "Consideration of loss distribution to evaluate the hot spot temeperature when up-rating generators," in *IEEE International Symposium on Electrical Insulation Conference*, San Diego, 2010.
- [81] *ANSYS Maxwell Release 16*, ANSYS, Inc.
- [82] ANSYS, "Equivalent BH curves for 2D Finite Element Analysis".
- [83] Y. B. Li, S. L. Ho, W. N. Fu and W. Y. Liu, "An interpolative finite element modeling and its starting process simulation of a large solid pole synchronous machine," in *ANSYS China user conference best paper*, 2011.
- [84] A. Ana, A. Merkhoul and K. Al-Haddad, "Influence of the air gap length on the magnetic core loss in large hydro generator," in *International Conference on Electrical Machines*, Marseille, 2012.
- [85] O.Stupakov, J. Pal'a, I. Tomas, J. Bydzovsky and V. Novak, "Investigation of magnetic response to plastic deformation of low-carbon steels," *Elsevier Journal of Materials Science and Engineering A*, vol. 462, pp. 351-354, 2007.

- [86] F. Landgraf and M. Emura, "Losses and permeability improvement by stress relieving fully processed electrical steels with previous small deformations," *Elsevier Journal of Magnetism and Magnetic Materials*, vol. 242, pp. 152-156, 2002.
- [87] K. Jeong, Z. Ren, H. Yoon and C.-S. Koh, "Measurement of stator core loss of an induction motor at each manufacturing process," *Journal of Electrical Engineering and Technology*, vol. 9, pp. 742-747, 2014.
- [88] K. Bourchas, "Manufacturing Effects on Iron Losses in Electrical Machines," KTH Royal Institute of Technology, Stockholm, 2015.
- [89] J. G. Wanjiku, N. Alatawneh and P. Pillay, "The effect of tooth-width on the distribution of rotational core losses," in *International Electric Machines and Drives Conference (IEMDC)*, Chicago, 2013.
- [90] M. Enokizono, H. Shimoji and T. Horibe, "Effect of stator construction of three-phase induction motors on core loss," *IEEE Transactions on Magnetics*, vol. 39, no. 3, 2003.
- [91] G. Diaz, C. Gonzalez-Moran, P. Arboleya and J. Gomez-Aleixandre, "Characterization of flux rotation and of the ensuing core losses in the stator of induction motors," *IEEE Transactions on Energy Conversion*, vol. 23, no. 1, 2008.
- [92] M. Lancarotte and A. d. A. P. Jr., "Improving the magnetizing device design of the single sheet tester of two-dimensional properties," *Elsevier Journal of Magnetism and Magnetic Materials*, vol. 269, no. 3, pp. 346-351, 2004.
- [93] P. P. J. C. Akiror, "On the coefficients of core loss formulas for electrical machines," in *IECON*, Montreal, 2012.
- [94] J. C. Akiror, T. Rahman and P. Pillay, "Progress on formulas for core loss calculations," in *XXth International conference on Electrical Machines (ICEM)*, Marseille, 2012.

- [95] S. Zurek, P. Marketos, T. Meydan and A. Moses, "Use of Novel Adaptive Digital Feedback for Magnetic Measurements under Controlled Magnetizing Conditions," *IEEE Transactions on Magnetics*, vol. 41, no. 11, 2005.
- [96] W. Salz, "A two dimensional measuring equipment for electrical steels," *IEEE Transactions on Magnetics*, vol. 30, no. 3, 1994.
- [97] S. Baranowski, E. Misiuk and S. Tumanski, "Comparison of various methods of the control of flux density waveform," *Elsevier Journal of Magnetism and Magnetic Materials*, no. 1-0, 2005.
- [98] S. Baranowski, S. Tumanski and S. Zurek, "Comparison of digital methods of the control of flux density shape," *PRZEGLĄD ELEKTROTECHNICZNY*, vol. 85, pp. 93-95, 2009.
- [99] S. Zurek and T. Meydan, "Digital feedback controlled RSST system," in *Soft Magnetic Materials Conference (SMM)*, Dusseldorf, 2003.
- [100] P. Anderson, "Measurement techniques for the assessment of materials under complex magnetising conditions," *Przegląd Elektrotechniczny*, vol. 87, no. 9b, pp. 61-64, 2011.
- [101] N. Chatziiliasa, T. Meydana and C. Porter, "Real time digital waveform control for magnetic testers," *Journal of Magnetism and Magnetic Materials*, Vols. 254-255, p. 104-107, 2003.
- [102] M. M. Znidarich, "Upgrading and Uprating of Hydro Generators: An Australian Perspective," *Australian Journal of Electrical and Electronics Engineering*, vol. 10, no. 1, pp. 75-84, 2013.
- [103] W. D. Blecken, "Applying new technology in the upgrading or uprating of generators," *Hydropower & Dams*, no. 5, pp. 26-32, 1997.

- [104] V. Thakur, "Upgrading and refurbishment of hydro generators," in *Advances in Electronics and Electrical Technology*, 2014.
- [105] J. Allen, "Hydro-generator refurbishment," *Sulzer Technical Review*, pp. 31-33, March 2011.
- [106] C. Grabner, "Comparative study on the analytical and numerical calculation of no-load harmonics in large salient-pole synchronous machines," in *International symposium on electric drives, automation and motion power electronics (SPEEDAM)*, Taormina, 2006.
- [107] A. Knight, S. Troitskaia, N. Stranges and A. Merkhof, "Analysis of large synchronous machines with axial skew, part 1: flux density and open-circuit voltage harmonics," *Electric Power Applications, IET*, vol. 3, no. 5, pp. 389-397, 2009.
- [108] M. Liwschitz-Garik, "Harmonics of salient-pole synchronous machine and their effects. Part 1 mmf harmonics produced by the armature and damper winding," *Transactions of the American Institute of Electrical Engineers, Power Apparatus and Systems, Part III*, vol. 75, no. 3, pp. 35-39, 1957.
- [109] J. Calvert, "Amplitudes of Magnetomotive Force Harmonics for Fractional Slot Windings-1," *Transactions of the American Institute of Electrical Engineers*, vol. 57, no. 12, pp. 777-785, 1938.
- [110] M. Znidarich, "Hydro Generator High Voltage Stator Windings: Part 2- Design for Reduced Copper Losses and Elimination of Harmonics," *Australian Journal of Electrical and Electronics Engineering*, vol. 5, no. 2, pp. 119-135, 2009.
- [111] C. G. Veinott, "Spatial harmonic magnetomotive forces in irregular windings and special connections of polyphase windings," *IEEE Transactions on Power Apparatus and Systems*, vol. 83, no. 12, 1964.
- [112] S. Timoshenko, *Vibration Problems in Engineering*, D. Van Nostrand Company, 1995.

- [113] H. C. Dirani, S. Cupillard, A. Merkhoul, A. T. S. Bélanger, A.-M. Giroux and K. Al-Haddad, "Free Vibration Analysis of a Large Hydro Electric Generator and Computation of Radial Electromagnetic Exciting Forces," in *International Electric Machines and Drives Conference (IEMDC)*, Coeur d'Alene, 2015.
- [114] B. Hague, "The mathematical treatment of the magnetomotive force of armature windings," *Journal of the Institution of Electrical Engineers*, vol. 55, no. 268, pp. 489-514, 1917.
- [115] J. Pyrhonen, T. Jokinen and V. Hrabovcov, *Design of Rotating Electrical Machines*, John Wiley & Sons Ltd, 2008.
- [116] Exponent, [Online]. Available: <http://www.exponent.com/capabilities/>. [Accessed 27 May 2015].
- [117] ASTM Committee on Magnetic Properties, *Standard Practice for Sampling and Procurement Testing of Magnetic Materials*, ASTM International, 2001.

Appendix A: Coil Sizing

Considering an uncooled open stator, the following assumptions can be made from (T. Chau, 2015)

Current density $J = 3 \text{ A/m}^2$

Slot fill factor $K_{sf} = 0.4$

Maximum number of conductors per slot $N = 10$

Maximum peak current per conductor $I_{pk} = 10 \text{ A}$, $I_{rms} = 7.07 \text{ A}$

Coil diameter

$$d = \sqrt{\frac{4I_{pk}}{\pi J}}$$
$$d = 2 \text{ mm}$$

Slot dimensions

Area of the slot from coil diameter

$$A_d = \frac{N \frac{\pi d^2}{4}}{K_{sf}}$$
$$A_d = 79 \text{ mm}^2$$

Area of the slot from slot dimensions

$$A_s = \frac{\pi * r^2}{2} + (l * w)$$
$$A_s = 89 \text{ mm}^2$$

$r = Bs2/3$, $w = \text{average}(Bs1, Bs2)$, $l = Hs2$ from slot dimensions in Figure 1.

$$A_d \cong A_s$$

Since the calculated area of the conductor is about 2 mm, $Bs0$ needs to be increased to 3 or 4 mm. In the prototype two 1 mm diameter cables were used.

AWG 2mm diameter cable is Gauge 12 with maximum current of 9.3A rms.

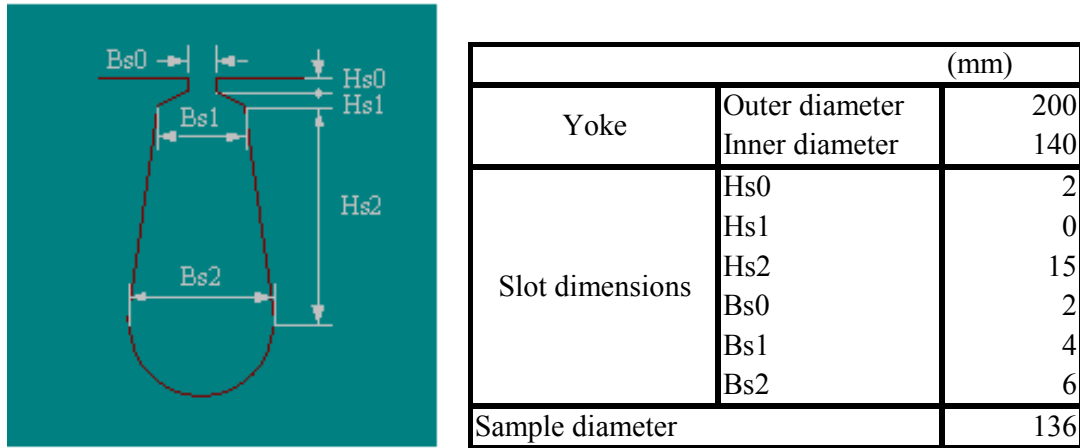


Figure 1: Slot dimensions

1. Electric vehicle machines and drives design, analysis and application by K.T. Chau, John Wiley & Sons Singapore Pte. Ltd, ISBN 978-1-118-75252-4

Appendix B: Magnetizer Set-up at IREQ

The magnetizer prototype, sensor coil placement, and set up are shown in Figure 2 and Figure 3. Table 1 shows a summary of the set up components and their specifications. The measurement procedure is presented in the next sub-section with reference to the installed software and operational LabVIEW VIs.

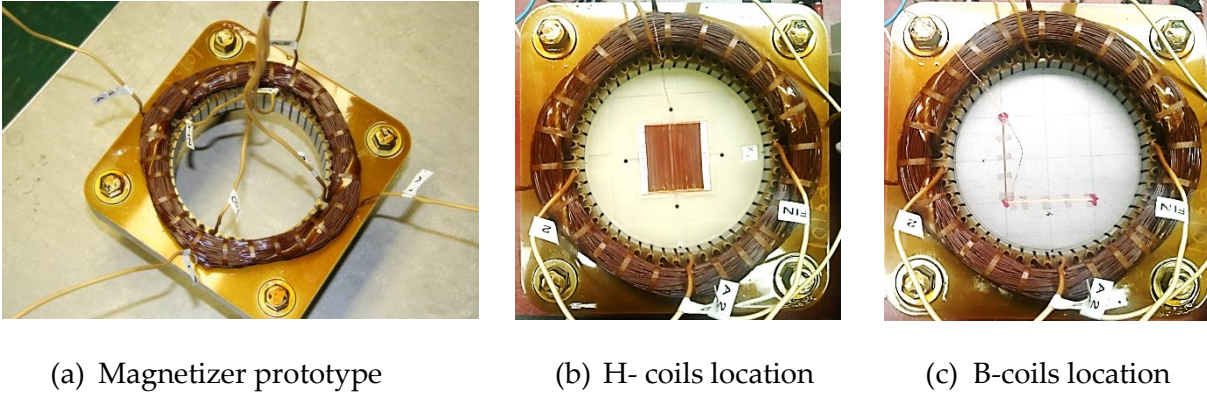


Figure 2: Prototype and sensor coil placement

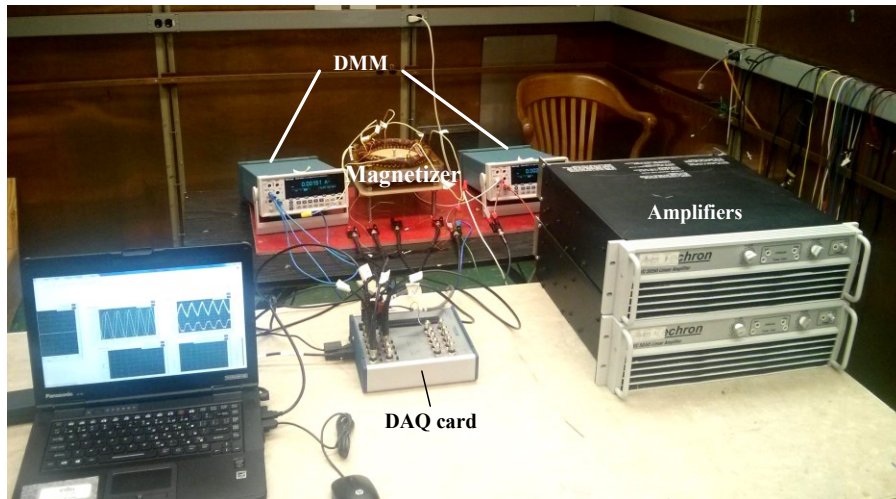





Figure 3: Magnetizer prototype set up

Table 1

Component	Specifications
<p>DAQ card</p> 	<ul style="list-style-type: none"> ➤ NI USB 6356-BNC ➤ 8 simultaneously sampled analog input channels ➤ 2 output channels ➤ 1.25MS/s/ch with 16 bit resolution <p>http://sine.ni.com/nips/cds/view/p/lang/en/nid/209075</p>
<p>Amplifier</p> 	<ul style="list-style-type: none"> ➤ LVC 5050 AE Techron Amplifier ➤ AC Mains: 60 Hz, 120 VAC with 30A ➤ Maximum load: 250 Volts RMS ➤ Parallel mono mode: for 1 kHz, 2Ω resistive load is 800 W, 40 V, 20 A <p>http://www.aetechron.com/pdf/service/LVC5050manual.pdf</p>
<p>Digital Multimeter</p> 	<ul style="list-style-type: none"> ➤ Tektronix DMM4040 digital multimeter ➤ 100 mV to 1 kV with up to 100 nV resolution ➤ 100 μA to 10 A current range with up to 100 pA resolution <p>http://www.testequity.com/products/1730/</p>
<p>PC</p>	<ul style="list-style-type: none"> ➤ LabVIEW installed

Pre-measurement Procedure

1. Connect the set up as shown in the schematic below

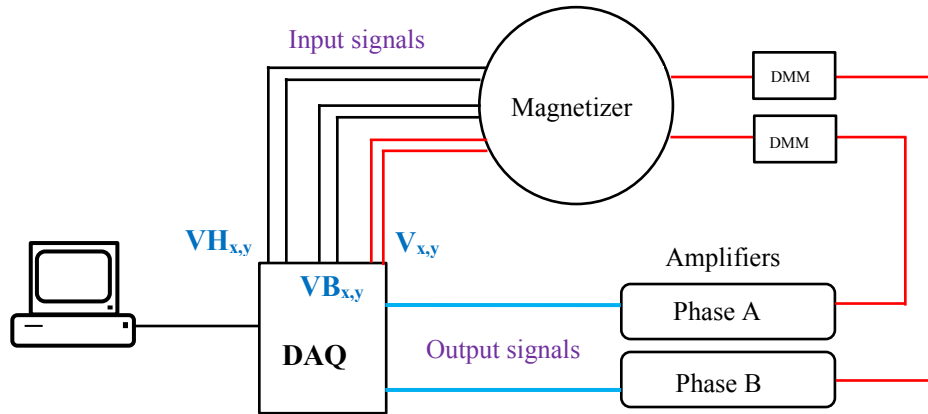


Figure. 5: Schematic of the connection diagram

2. Connect the DMMS to measure current in each phase winding. Ensure the DMMs are set to measure AC current maximum 10 A.
3. Connect output signals from the AO0 and AO1 BNCs to Phase A and Phase B amplifiers respectively
4. Measure the Phase A and Phase B voltages via attenuators to BNC input channels AI0 and AI1 respectively
5. Place one **H**-coil (**H_x** coil) in the lower sample holder slot to measure the magnetic field intensity in the X. Pass the leads out through a hole in the sample holder and connect them to the BNC AI4. This coil will measure the VH_x .
6. Place the second **H**-coil (**H_y** coil) in top sample holder slot to measure the magnetic field intensity in the Y. Pass the leads out through a hole in the sample holder and connect them to the BNC AI5. This coil will measure the VH_y .
7. Place the sample on top of the **H_x** coil and pass the X coils from the sample through a hole in the lower sample holder. Connect this coil to BNC AI2. This coil will measure the VB_x .
8. Pass the second coils from the sample through the holes on the top sample holder. Connect this coil to BNC AI3. This coil will measure the VB_y .

Measurement Procedure

1. Start the core loss project in LabVIEW and open measurements.vi
2. Fill in the necessary constants to initialize the VI
 - Material density
 - Constant for the H-coils; $N_H \cdot A \cdot \mu_0$
 - Constant for the B-coils; $N_B \cdot A$

- Sampling rate and number of samples for both generation and acquisition
 - Appropriate phase between X and Y – CW or CCW
3. Turn on the NI USB card
 4. Turn on the amplifiers
 5. Run the simulation
 6. Increase the Gain button to the required flux density shown in the B_x and B_y indicator

B_y is usually less than B_x because B_x is in the rolling direction of the sample. Turn off the main Gain and increase the Phase B gain alone until both B_x and B_y are the same.

7. Check the aspect ratio is as desired, the phase difference between X and Y is 90°
8. Click the calculate core loss button to allow the system to calculate the core loss as an average of the last measured 100 iterations
9. Repeat steps 6-8 until all the required flux densities are measured
10. Reduce the gain to almost 0 or until the current in the DMMs is 0. Click the Stop button vi
11. When the vi stops. It will prompt for a folder and file name to store the core loss and flux density data. Save the data and the vi stops.

Recommendations

1. 1. Number of samples and sampling rate
2. Each DAQ card has its functionality limits, before taking any measurements check to ensure that the number of samples and sampling rate is appropriate. This can be done by seeing the integrated H-signals. They should be periodic sinusoids.
3. 2. Limit the maximum current to 10 A
4. For high flux densities, the required current will be high but since the winding, amplifiers, DMMs and set-up is designed for 10 A, limit the current to 10 A. For currents above 10 A ensure that the measurement is taken quickly and the current reduced to less than 10 A.

Core loss calculation

The field metric method is used to obtain core losses from the measured field quantities in the x and y using the following equation

$$P = \frac{1}{T\rho} \int_0^T \left(H_x \frac{dB_x}{dt} + H_y \frac{dB_y}{dt} \right) dt$$

Where the field intensity (H) and flux density (B) are obtained from the measured coil sensor voltages e_B and e_H respectively, **B** and **H** can be calculated using

$$H = \frac{K_{cal}}{\mu_0 N_H A_H} \int e_H(t) dt$$

$$B = \frac{1}{N_B A_B} \int e_B(t) dt$$

$N_H = 220$ – number of turns of the H-coils

$A_H = 53e-3 * 1.5e-3$ – area of the H-coils

$\mu_0 = 1.256637e-6$ – permeability of air

$N_B = 5$ – number of turns of the B-coils

$A_B = 65e-3 * 0.48e-3$ – area of the B-coils

Appendix C: Safe Operating Procedures for the Rotational Core Loss Test Bench at Concordia University Power Lab

DO NOT use if the system setup is not aptly connected as shown in the figure below.



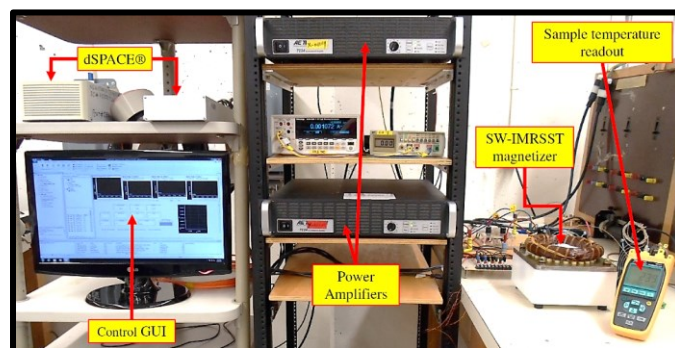
Wear appropriate safety footwear



Wear safety glasses

Procedure

1. Ensure there are no loose connections and the setup is well connected.
2. Plug the transformer into the power outlet.
3. Switch on the dSPACE.
4. Switch on the computer.
5. Open MATLAB and build the Simulink model.
6. Open dSPACE Control desk, load the project and experiment.
7. Switch on the 3phase breaker to power the amplifiers.
8. Switch on the two amplifiers.
9. Slowly increase the amplifier gains to the desired value, one at a time. Ensure no current is flowing as you increase the gains.
10. Run the dSPACE experiment.
11. Take the required measurements.
12. Reduce the output current to zero. Stop the dSPACE measurement and go offline.
13. Reduce the amplifier gains to zero slowly, one at a time.
14. Switch the amplifiers off.
15. Disconnect the amplifier breaker.
16. Close the dSPACE control desk, MATLAB, switch off the dSPACE and shut down the computer.
17. Disconnect the transformer from the power outlet.



Appendix D: Z-component field intensity distribution 1 mm above the sample for the proposed magnetizer

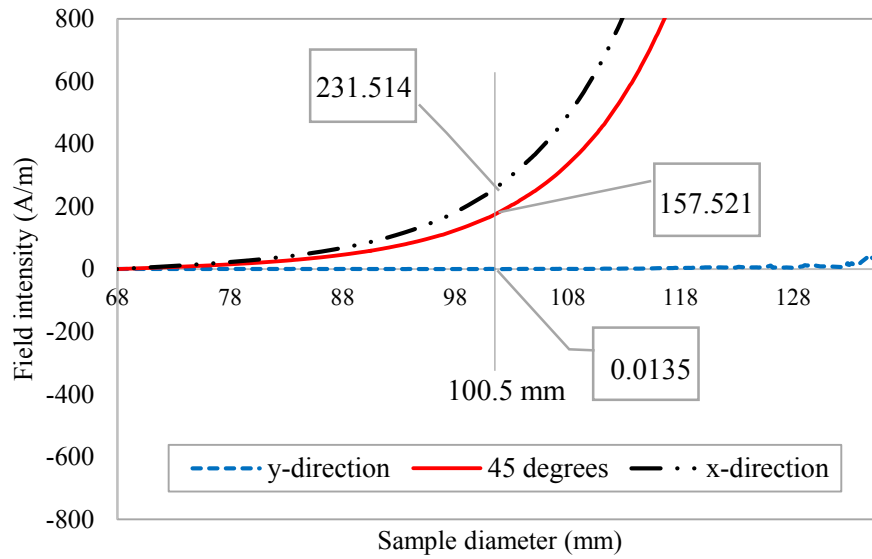


Figure. 6: Z-component of field intensity at low flux density of 0.56 T

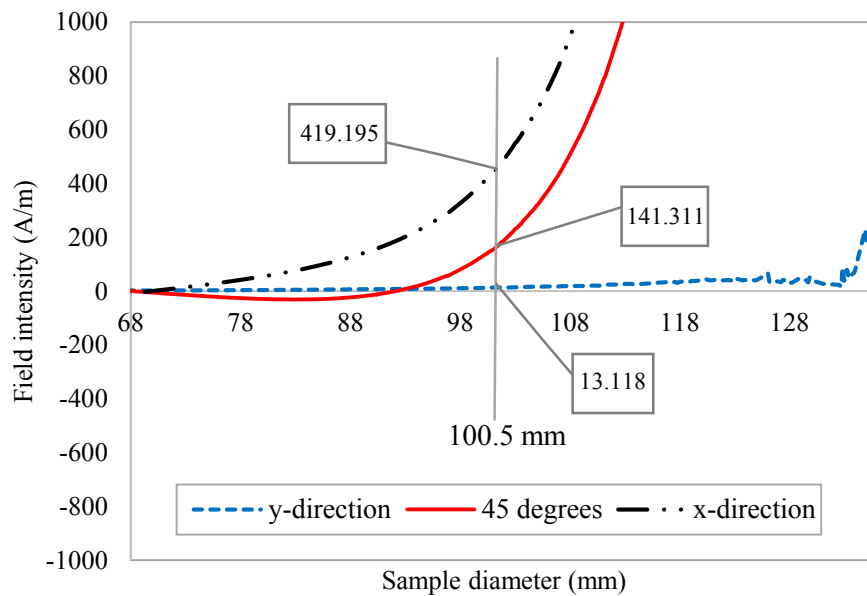


Figure. 6: Z-component of field intensity at high flux density of 1.6 T